TECHNISCHE UNIVERSITÄT WIEN

VIENNA UNIVERSITY OF TECHNOLOGY

DISSERTATION

Calibrating the CERN ATLAS Experiment with E/p

ausgeführt zum Zwecke der Erlangung des akademischen Grades eines Doktors der technischen Wissenschaften unter der Leitung von

Univ. Prof. Dipl.-Ing. Dr. Christian Fabjan
E141
Atominstitut der österreichischen Universitäten

eingereicht an der Technischen Universität Wien
Fakultät für Physik

von

Dipl.-Ing. Mag. Robert Fröschl
Matrikelnummer: 9426271
Bobiesgasse 3/4/5
1230 Wien

Wien, im September 2009

Kurzfassung

Innerhalb des ATLAS Experiments werden zwei Protonstrahlen mit einer Schwerpunktenergie von $\sqrt{s} = 14$ TeV zur Kollision gebracht und die dabei entstehenden Teilchen detektiert. Diese Protonstrahlen werden durch den Large Hadron Collider (LHC) des European Center of Particle Physics, CERN, in Genf erzeugt.

Für essentielle Punkte des Physikprogramms von ATLAS, wie z.B. die Suche nach dem Higgs–Boson, ist die Qualität der Energiemessung von Elektronen und Photonen durch das elektromagnetische Kalorimeter von entscheidender Bedeutung.

Das zentrale Thema der Dissertation ist die relative Kalibrierung der Energieskala des elektromagnetischen Kalorimeters und der Impulsskala des inneren Spurendetektors. Diese Kalibrierung basiert auf der Verteilung des Verhältnisses E/p für Elektronen, wobei E die Energie gemessen durch das elektromagnetische Kalorimeter und p der Impuls gemessen durch den inneren Spurendetektor bezeichnen.

Ausgangspunkt ist der Combined Test Beam 2004, ein Teststrahlversuch im Jahre 2004, bei dem ein vollständiges Segment des ATLAS Detektors mit verschiedenen Teilchen mit Energien von 1 GeV bis 350 GeV beschossen wurde. Zuerst habe ich die Kalibrierung der Energiemessung des elektromagnetischen Kalorimeters für Elektronen mittels Monte Carlo Simulationen untersucht. Die mit dieser Methode erzielte Qualität der Kalibrierung wird anhand von Daten des Combined Test Beam 2004 demonstriert. Im Anschluss daran habe ich ein Model für die E/p Verteilung entwickelt, welches es ermöglicht, die relativen Skalen des elektromagnetischen Kalorimeters und des inneren Spurendetektors zu extrahieren. Die Leistungsfähigkeit dieses Modells wird zuerst für den Combined Test Beam 2004 demonstriert und dann auf Monte Carlo Simulationen für den vollständigen ATLAS Detektor angewandt.

Die Energieskala des elektromagnetischen Kalorimeters wird letzten Endes mit Elektron/Positron–Paaren von Z Bosonzerfällen bestimmt werden. Allerdings ist dafür eine sehr große Anzahl von Ereignissen notwendig. Daher wird die Leistungsfähigkeit der von mir entwickelten Kalibrierung mit begrenzter Statistik präsentiert. Weiters kann

mit dieser Methode die Energieskala für verschiedene Energiebereiche bestimmt werden. Dies erlaubt eine in–situ Messung der Linearität des elektromagnetischen Kalorimeters. Diese Vorgehensweise ist nur durch die verfügbare Anzahl von Elektronen mit hoher Energie und schlussendlich durch die Fähigkeit des inneren Spurendetektors, den Impuls sehr hochenergetischer Teilchen zu messen, begrenzt.

Abstract

Inside the ATLAS experiment two proton beams will collide with a center of mass energy of $\sqrt{s} = 14$ TeV. These proton beams will be delivered with unprecedented high collision rates by the Large Hadron Collider (LHC) at the European Center of Particle Physics, CERN.

For important parts of the physics program of ATLAS, e.g. the search for the Higgs boson, the performance of the electromagnetic calorimeter, whose primary task is to measure the energy of electrons and photons, is crucial.

The main topic of this thesis is the intercalibration of the energy scale of the electromagnetic calorimeter and the momentum scale of the inner detector. This is an important consistency test for these two detectors. The intercalibration is performed by investigating the ratio E/p for electrons, i.e. the ratio of the energy E measured by the electromagnetic calorimeter and the momentum p measured by the inner detector.

The starting point is the Combined Test Beam (CTB) 2004, where a segment of the ATLAS detector was exposed to different particle beams with different energies, ranging from 1 GeV to 350 GeV. First, I have investigated a calibration procedure using Monte Carlo simulation for the energy measured by the electromagnetic calorimeter for electrons. The performance of this procedure is presented for data taken in the CTB 2004. Second, I have developed a model for E/p which allows the disentanglement of the ratio of the two scales from tail effects from the different detector response functions of the inner detector and the electromagnetic calorimeter. The performance of this model for intercalibration is shown for the Monte Carlo simulation for the CTB 2004 and compared to data taken in the CTB 2004. Finally I have evaluated the performance of this method for the full ATLAS detector using Monte Carlo simulation.

Although the energy scale of the electromagnetic calorimeter will ultimately be determined with electron/positron pairs from Z boson decays, the potential of the intercalibration method with initial data, and therefore limited statistics, is presented. With the presented intercalibration method the energy scale can also be determined for various

electron energies, thereby measuring the linearity of the electromagnetic calorimeter in situ. This will only be limited by statistics, i.e. the number of electrons produced at high energies, and ultimately the capability of the inner detector to measure the momentum of charged particles at very high energies.

Acknowledgements

I want to thank Chris Fabjan for the supervision of this PhD thesis. His valuable remarks have always enabled me to make a step forward in my work. I thank Martin Aleksa who provided crucial guidance for my work. I learned a lot from our discussions and they broadened my horizon. For all the informal discussion I especially wish to thank Guillaume Unal, Tancredi Carli, Marco Delmastro, Walter Lampl and Daniel Froidevaux.

In general, I enjoyed the working atmosphere at CERN that promotes critical, but fruitful discussion without hierarchy boundaries.

Most of all I thank my wife Lena and my daughter Nika for making the last years so wonderful.

Contents

1 The Large Hadron Collider

This chapter is devoted to the Large Hadron Collider accelerator complex (section 1.1) and the major experiments that are going to make use of the collisions provided by the Large Hadron Collider (section 1.2).

1.1 The Large Hadron Collider accelerator complex

The Large Hadron Collider (LHC) is a hadron accelerator and storage ring collider at CERN near Geneva [1]. It is located in the tunnel where previously the Large Electron Positron (LEP) collider had been installed. This tunnel has a circumference of 26659 meters and an internal diameter of 3.7m in the arcs. This constraint essentially did not allow the construction of two completely separate proton rings. Instead, the so called twin-bore magnet design was chosen meaning that the windings for the two beam channels are situated in a common cold mass and cryostat. Because the LHC is a particle–particle collider (and not a particle–antiparticle collider as the Tevatron for example), the magnetic flux has to be directed in the opposite sense for the two beam channels.

The schematic layout of the LHC is shown in figure 1.1. The LHC consists of 8 sectors. In the middle of all sectors are the so called long straight sections where the beams can be collided. This will only be done at Interaction Point (IP) 1 for the ATLAS experiment, at IP 2 for the LHCb experiment, at IP 5 for the CMS experiment and at IP 8 for the ALICE experiment. The other long straight sections will be used for beam cleaning, for the beam dump and to house the radio frequency (RF) system.

In order to keep the particles on orbit 1232 superconducting dipole magnets are used. These dipole magnets have a nominal field of 8.33 T corresponding to a nominal energy of 7 TeV per beam. The dipole magnets are made up of NbTi Rutherford cables that are cooled down to 1.9 K with superfluid helium. The quality requirements for the dipole magnets are very high. The upper bound on the relative variations of the integrated field, the field shape imperfection and their reproducibility is 10^{-4}. In addition to the

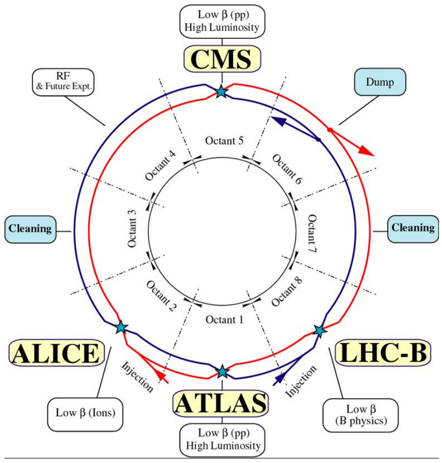

Figure 1.1: The schematic layout of the Large Hadron Collider (LHC).

dipole magnets the LHC magnet system contains a variety of different magnets such as focusing and defocusing quadrupole magnets or chromaticity correcting sextupoles. A full inventory of the LHC magnet system is given in [1].

The primary operation mode for the LHC will be to collide 2 proton beams. From the proton source the protons are first accelerated by the Linac2, then by the Proton Synchrotron Booster (PSB), then by the Proton Synchrotron (PS) and then by the Super Proton Synchrotron (SPS) to an energy of 450 GeV, which is the injection energy into the LHC. Through dedicated transfer lines the protons are injected into the LHC which then accelerates the protons to the design energy of 7 TeV per beam, resulting in a center of mass energy of $\sqrt{s} = 14$ TeV for proton–proton collisions. The protons are divided into 2808 bunches where each bunch contains $1.15 \cdot 10^{11}$ protons. This results in a beam current of 0.58 A. The interval between bunch crossings for collisions is 25 ns.

In the first year of LHC operation neither the design energy nor the design luminosity will be reached. It is planned to operate at 3.5 TeV per beam at the beginning and then to increase the energy to 5 TeV per beam in the first year of operation.

The peak luminosity that will be delivered to the ATLAS and CMS experiments is $10^{34}\,\mathrm{cm}^{-2}\,\mathrm{s}^{-1}$, which corresponds to approximately 10^9 collisions per second. This peak luminosity is unprecedented for a hadron collider and cannot be achieved with a proton–antiproton machine (like the Tevatron) with present day technology. Mainly due to beam loss from collisions the luminosity degrades over time. The estimated luminosity lifetime (the time after the luminosity has fallen to $1/e$ of the initial luminosity) is estimated to be

14.9 h. The expected average turnaround time (time between two runs needed to ramp down the machine and to ramp it up again) is around 7 hours implying an optimum run duration of 12 hours. Together with the assumption of 200 days of machine operation per year and accounting for the uncertainty of the average turnaround time, this yields a maximum total integrated luminosity[1] of 80-120 fb^{-1} per year.

Apart from colliding protons the LHC is also able to accelerate and collide fully stripped lead ($^{208}\mathrm{Pb}^{82+}$) ions at a center of mass energy of $\sqrt{s} = 1148$ TeV, meaning 2.8 TeV per nucleon per beam. The maximum luminosity for ion–ion collisions that will be delivered at IP8 for the ALICE experiment which is a dedicated heavy ion experiment is $1.0 \cdot 10^{27}\mathrm{cm}^{-2}\mathrm{s}^{-1}$.

1.2 Experiments at the Large Hadron Collider

This section describes the main experiments that will be operated at the LHC. The ATLAS experiment will be presented in chapter 2 in more detail.

1.2.1 ALICE

ALICE (**A** **L**arge **I**on **C**ollider **E**xperiment) is a general–purpose detector dedicated to heavy ion physics [2]. It primary will probe quantumchromodynamics (QCD) at extreme energy densities and temperatures which lead to the production of quark–gluon plasma. The schematic layout of ALICE is shown in figure 1.2. ALICE uses the solenoid magnet from the previous L3 experiment at LEP to provide the magnetic field for the central barrel part of the detector. A dipole magnet creates the magnetic field for the forward muon spectrometer.

At the interaction point inside ALICE, lead ions will be collided with a center of mass energy of $\sqrt{s} = 1148\,\mathrm{TeV}$ at a luminosity of $10^{27}\,\mathrm{cm}^{-2}\,\mathrm{s}^{-1}$. This will lead to extreme charged particle multiplicities at mid–rapidity, i.e. close to the plain which containts the inertaction point and is orthogonal to the beam axis. The ALICE detector is designed to operate at charged particle multiplicities up to $dN/d\eta = 8000$. The most recent estimate including extrapolations of measurements done by the RHIC detector at the Brookhaven National Laboratory is $dN/d\eta = 1500 - 4000$.

[1] The integrated luminosity $\mathcal{L}$ is defined as the integral of the luminosity over time. The average number of events N for a process for a certain time interval is the product of the integrated luminosity for the time interval and the cross section for the process σ, i.e. $N = \mathcal{L}\,\sigma$.

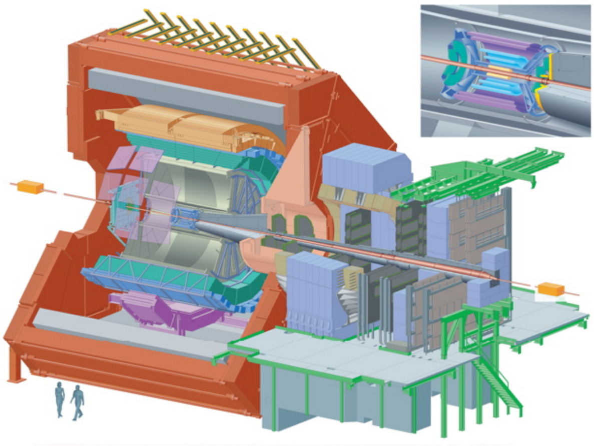

Figure 1.2: The schematic layout of the ALICE detector.

These high charged particle multiplicities constrained the choice of tracking detectors severely. Three tracking systems are employed in the barrel part of ALICE. The Inner Tracking System (ITS) made up of 6 silicon layers, the Time Projection Chamber (TPC) with a very low material budget and the Transition Radiation Detector (TRD) which also contributes to electron identification. Further systems for particle identification are the Time of Flight (TOF) array using Multigap Resistive Plate Chambers and the High Momentum Particle Identification Detector (HMPID) consisting of proximity–focusing Ring Imaging Cherenkov (RICH) counters.

The PHOton Spectrometer (PHOS) is a single–arm high–resolution high–granularity electromagnetic spectrometer consisting of 2 parts. The first is the electromagnetic calorimeter made up of 17.920 $PbWO_4$ crystals. $PbWO_4$ was chosen because of its very small moliere radius and radiation length. The calorimeter is highly segmented and has a depth of 20 radiation lengths. The second is a Charged–Particle Veto (CPV) detector. This is a Multi–Wire Proportional Chamber (MWPC) with a charged particle rejection better than 99%. The primary focus of PHOS is meson identification at low p_T and photon identification and energy measurement.
The Electro Magnetic CALorimeter (EMCal) is a large Pb–scintillator sampling calorimeter with cylindrical geometry that is read out via wavelength–shifting fibres. Its main goal is to study jets, and in particular the interaction of energetic partons with dense partonic matter.

The design criterion for the forward muon spectrometer was a mass resolution of $100\,\mathrm{MeV}/c^2$ to allow the separation of all states of heavy quark resonances like

$J/\Psi, \psi', \Upsilon, \Upsilon', \Upsilon''$. The forward muon spectrometer covers a pseudo–rapidity range of $-4 < \eta < -2.4$. Ten planes of modules are used for the inner muon tracking, four planes of Resistive Plate Chambers for the outer muon tracking.

1.2.2 CMS

The Compact Muon Solenoid (CMS) is a general-purpose detector, high luminosity detector [3]. The schematic layout of CMS is shown in figure 1.3.

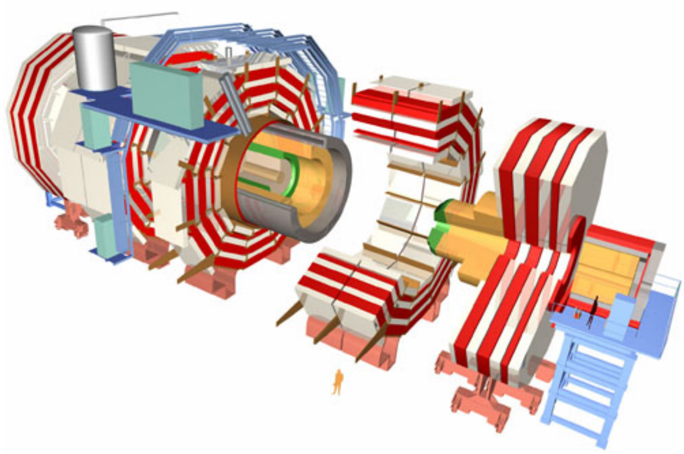

Figure 1.3: The schematic layout of the CMS detector.

Although the physics program of CMS is very similar to that of ATLAS, very different design decisions have been made. Most striking, CMS will use only one superconducting magnet to produce a 4 T solenoidal field in the central cylindrical region (diameter 6 m, length 12.5 m). The magnet is made of NbTi and the energy stored in it is 2.6 GJ.

The Inner Tracking System consists exclusively of silicium detectors. This choice was driven by the granularity, speed and radiation hardness requirements. At design luminosity of $10^{34}\,\mathrm{cm}^{-2}\,\mathrm{s}^{-1}$ on average 1000 particles will be created from 20 simultaneous proton-proton collisions per bunch crossing. The measurement of the track parameters of all the charged particles and the reconstruction of displaced secondary vertices for τ and b–jet tagging are the main purpose of the Inner Tracking System. Its coverage in pseudo–rapidity is $|\eta| \leq 2.5$. This is achieved by 3 barrel pixel layers and 10 silicon strip larrel layers and their corresponding endcap detectors. In total the Inner Tracking System has an area of active silicon of 200 m^2, making it the largest silicon tracker ever built.

The Electromagnetic Calorimeter (ECAL) is a homogeneous scintillation calorimeter. It consists of 61200 $PbWO_4$ crystalls. $PbWO_4$ has a very small radiation length (0.89 cm) and Molire radius (2.2 cm) making it possible to implement a compact design for the ECAL. Furthermore its scintillation decay time is comparable to the LHC bunch crossing time of 25 ns. The scintillation photons are detected by Avalanche Photodiodes (APDs) in the barrel and by Vacuum Phototriodes (VPTs) in the endcaps. A laser monitor system is used to monitor the evolution of the crystal transparency which degrades under irradiation. The information of this system is used for calibration purposes.

The Hadronic Calorimeter (HCAL) is a sampling calorimeter using brass as absorber and plastic scintillator as active medium. It is read out via wavelength–shifting fibres. The HCAL and the ECAL are both placed inside the solenoid magnet coil. Due to this restriction an outer hadron calorimeter had to be placed outside of the solenoid magnet to provide a sufficient interaction depth for the barrel region.

Two forward detectors are employed. The Centauro And Strange Object Research (CASTOR) detector is a quartz-tungsten sampling calorimeter with a pseudo–rapidity coverage of $5.2 < |\eta| < 6.6$ for diffractive and low–x studies.. The Zero Degree Calorimeter (ZDC) is a quartz-tungsten sampling calorimeter which covers the pseudo–rapidity range $|\eta| \geq 8.3$ for neutral particles contributing to heavy ion and proton-proton diffractive physics.

The muon system covers the pseudo–rapidity range $|\eta| < 2.4$. In the barrel part $|\eta| < 1.2$ Drift Tube (DT) chambers are used. The endcaps are equipped with Cathode Strip Chambers (CSC) because of higher particle rates. Both systems can trigger on the transverse momentum[2] p_T of muons. In addition, Resistive Plate Chambers (RPC) are also used for triggering purposes. Together with the inner tracking system a good momentum resolution is achieved, about 5% for muons at 1 TeV/c. The charge of the muon can be unambiguously determined up to 1 TeV/c.

1.2.3 LHCb

The LHCb experiment will study heavy flavour physics at the LHC [4]. The main point of its physics program is the search for new physics via CP violation and rare decays of beauty and charm hadrons, mainly B_d, B_s and D mesons. The B mesons will be generated via $b\bar{b}$ production which has a cross section of approx. 500 μb at 14

[2]The transverse momentum p_T is defined as the component of the momentum vector that is orthogonal to the beam axis.

TeV center of mass energy for proton-proton collisions. The optimal luminosity for p-p collisions for LHCb is $2{\cdot}10^{32}\,\mathrm{cm}^{-2}\,\mathrm{s}^{-1}$. At this level of luminosity the detector occupancy and radiation damage are kept at a reasonable level and on average there is less then a single proton-proton interaction per bunch crossing. In order to stay at this luminosity level at nominal LHC running conditions the beam focus at the LHCb interaction point can be adjusted independently from the other interaction points.

The schematic layout of LHCb is shown in figure 1.4. LHCb is an asymmetric experiment (wrt. η) with an acceptance range of $1.6 < \eta < 4.9$. The magnet that provides the magnetic field for the outer tracking system is a warm magnet. The direction of the magnetic field will be changed periodically in order to control the systematic effects for CP asymmetry measurements.

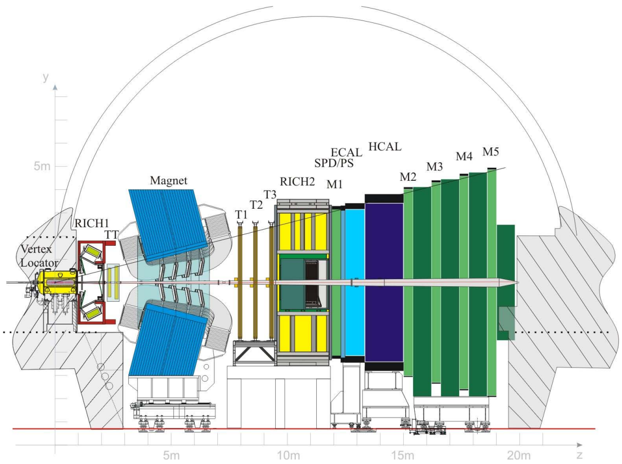

Figure 1.4: The schematic layout of the LHCb detector.

The tracking system of LHCb consists of 3 parts. The Vertex Locator (VELO) is positioned next to the interaction region and its main purpose is the measurement of tracks in the proximity of the interaction region. These measurements are crucial for the identification of displaced secondary vertices that are characteristic for b and c–hadron decays. The Silicon Tracker consists of two detectors, namely the Tracker Turicensis (TT) and the Inner Tracker (IT). Both of them use silicon microstrip sensors. The TT is positioned upstream of the magnet while the IT is located downstream. Both have small overall material keeping the degradation of the resolution due to multiple scattering at an acceptable level. The Outer Tracker (OT) is designed as a drift time detector using drift tubes filled with a mixture of Argon (70%) and CO_2 (30%).

Particle identification is provided by two Ring Imaging Cherenkov (RICH) detectors. RICH1 is located upstream of the magnet while the RICH2 is situated downstream. RICH1 uses aerogel and C_4F_{10} radiators to separate pions from kaons at the low momentum charged particle range from 1 to 60 GeV/c while RICH2 employs CF_4 a radiator in the high momentum range from 15 to well above 100 GeV/c. Both use a spherical mirror to reflect the cherenkov photons out of the spectrometer acceptance and than a flat mirror to propagate them to the Hybrid Photon Detectors (HPDs). The HPDs can measure photons at wavelengths of 200–600 nm.

The calorimeter system consists of an electromagnetic calorimeter (ECAL) which is a Pb–scintillator sampling calorimeter and a hadronic calorimeter (HCAL) which is an Iron–scintillator sampling calorimeter. Both are read out via wavelength–shifting fibres. The systems contribute to the particle identification of electrons, photons and hadrons and also measure their energy. Prompt photons and π^0 also have to be reconstructed well for flavour tagging.

The first muon station is situated right upstream of the electromagnetic calorimeter. A triple Gas Electron Multiplier (GEM) detector is used in its inner region to deal with the expected particle rate. The outer region of the first muon station and the other four muon stations that are downstream of the calorimeters consist of Multi-Wire Proportional Chambers (MWPC). The first three muon stations perform tracking while the two outer most stations are used to identify penetrating particles.

2 The ATLAS Experminent

The ATLAS (A Toroidal LHC ApparatuS) detector is a general–purpose detector that will take data from proton–proton collisions at the LHC with a center of mass energy of 14 TeV at a design luminosity of $10^{34}\,\mathrm{cm}^{-2}\,\mathrm{s}^{-1}$ [5]. The requirements imposed by the physics program of ATLAS are discussed in section 2.1. After describing the magnet system of ATLAS in section 2.2, the three main detector subsystems are presented in the following sections, the Inner Detector in section 2.3, the calorimetry subsystems in section 2.4 and the muon spectrometer in section 2.5. The overall layout of the ATLAS detector is shown in figure 2.1.

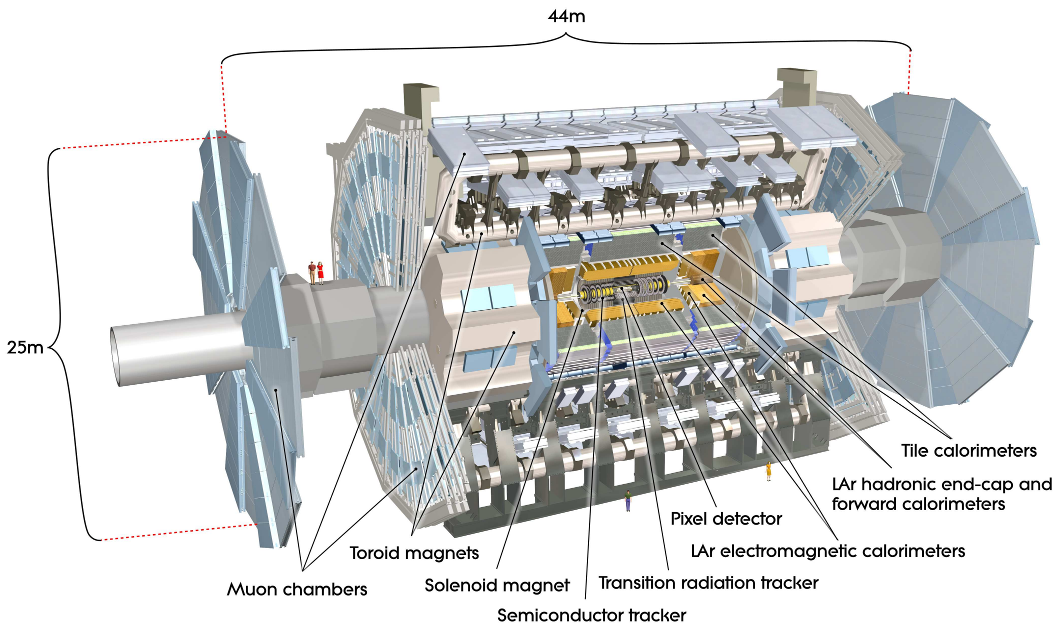

Figure 2.1: Cut-away view of the ATLAS detector. The dimensions of the detector are 25 m in height and 44 m in length. The overall weight of the detector is approximately 7000 tonnes. Taken from [5].

2.1 Physics requirements

A primary task of the ATLAS detector is the search for the standard model Higgs boson H which is a benchmark process for many of the subdetectors of ATLAS since the production and decay mechanisms vary considerably as a function of the Higgs boson mass. Important decay channels are $H \to \gamma\gamma$, $H \to b\bar{b}$ and $H \to ZZ^{(*)}$. The sensitivity of ATLAS for the discovery of a Standard Model Higgs boson in terms of the significance of the signal for Higgs boson decays as a function of the Higgs boson mass and the integrated luminosity is shown in figure 2.2.

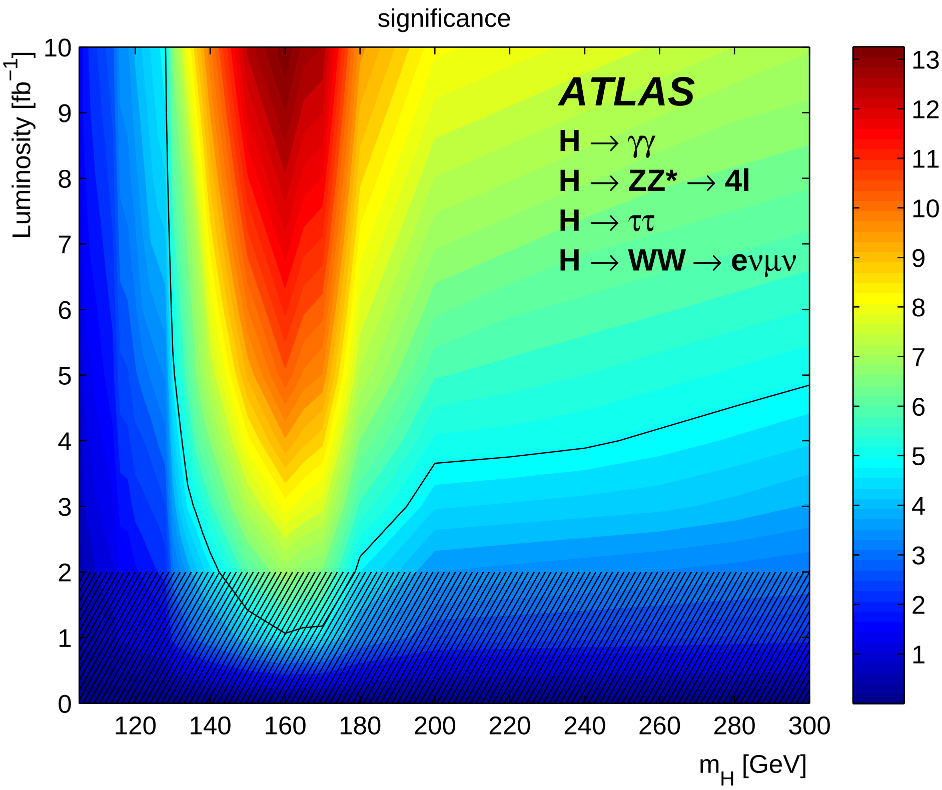

Figure 2.2: Significance contours for different Standard Model Higgs masses and integrated luminosities. The solid curve represents the 5σ discovery contour. The median significance is shown with a colour according to the legend. The hatched area below $2\,\mathrm{fb}^{-1}$ indicates the region where the approximations used in the combination of the four decay channels are not accurate, although they are expected to be conservative.

Searches for physics beyond the standard model will include processes with a transverse momentum p_T up to a few TeV. For the search for new heavy gauge bosons W' and Z'

through their lepontic decays this means that the resolution and charge identification must still be accurate in this high momentum range. The search for quark compositeness involves very high p_T jets and requires a good linearity for jet energies up to several TeV.

Another variable sensitive to physics beyond the standard model is the missing transverse energy[1] E_T^{miss}. For supersymmetric models[2] where the R-parity is conserved, the decay of supersymmetric particles would proceed in cascades where the lightest stable supersymmetric particle (LSP) would not be able to decay any further and would escape the detector nearly without interacting with the detector therefore creating a significant E_T^{miss}. Other models that have experimental signatures including a significant E_T^{miss} are extra dimensions models and quantum gravity.

The ATLAS detector will also perform high precision tests of the standard model of particle physics. Among the properties to be measured are the top quark mass, the top quark spin and the W boson mass with a desired precision of 10 MeV.

At the design luminosity of $10^{34}\,\mathrm{cm}^{-2}\,\mathrm{s}^{-1}$ approximately 23 inelastic proton–proton collisions will occur at each bunch crossing. Together with a bunch crossing spacing of 25 ns this will result in a enormous particle production rate that requires a highly efficient trigger system to detect events of interest over the large background as well as fast and radiation hard sensors and electronics.

All the benchmark processes mentioned above lead to the following requirements for the ATLAS detector, see table 2.1:

1. Large acceptance in φ and in pseudorapidity for a good E_T^{miss} resolution.
2. Good charged-particle momentum resolution, charge identification and reconstruction efficency in the inner tracker. Good resolution for secondary vertices for τ

[1]Since the detector inertial system is the center of mass system of the colliding protons, the vector sum of the momenta of all particles is zero for each proton-proton collision. Since the detector does not cover a small stereo angle around the beam axis, the sum of the momenta of the particles in the detector acceptance region can be deviate from 0. However, the transverse component of the momenta in the uncovered regions is very small. As a consequence the sum of the transverse momenta of the particles in the detector acceptance region is always very close to 0. If a particle has significant momentum and escapes the detector unmeasured, i.e. a neutrino, the sum of the measured transverse momenta is not zero and this is denoted *missing transverse energy*, E_T^{miss}.

[2]Supersymmetry is the concept for an invariance that links fermions and bosons. Every fermion has a bosonic supersymmetric partner and every boson has a fermionic supersymmetric partner. The main advantage of Supersymmetry is that the loop corrections in the Higgs mass renormalization cancel exactly due to the opposite sign for fermions and bosons, therefore solving the *hierarchy problem* in an elegant way.

and b-jet tagging.

3. Excellent electromagnetic calorimetry for electron and photon identification and measurements.

4. Hadronic calorimetry with large coverage for jet and E_T^{miss} measurement.

5. Good muon momentum resolution, charge identification and reconstruction efficency in the muon spectrometer up to the TeV range.

6. The electronics and sensor elements must be fast and radiation–hard due to the experimental conditions at the LHC.

7. Efficient trigger also for low p_T objects with sufficient background rejection.

Turning these requirements into numbers yields the required performance listed in table 2.1.

Detector component	Resolution	η measurement	η trigger
Tracking	$\sigma_{p_T}/p_T = 0.05\% p_T \oplus 1\%$	$\lvert\eta\rvert < 2.5$	
Electromagnetic calorimetry	$\sigma_E/E = 10\%/\sqrt{E} \oplus 0.7\%$	$\lvert\eta\rvert < 3.2$	$\lvert\eta\rvert < 2.5$
Hadronic calorimetry			
barrel and endcap	$\sigma_E/E = 50\%/\sqrt{E} \oplus 3\%$	$\lvert\eta\rvert < 3.2$	$\lvert\eta\rvert < 3.2$
forward	$\sigma_E/E = 100\%/\sqrt{E} \oplus 10\%$	$3.1 < \lvert\eta\rvert < 4.9$	$3.1 < \lvert\eta\rvert < 4.9$
Muon spectrometer	$\sigma_{p_T}/p_T = 10\%$ at $p_T = 1\,\text{TeV}$	$\lvert\eta\rvert < 2.7$	$\lvert\eta\rvert < 2.4$

Table 2.1: Required performance of the ATLAS detector. The unit for E is GeV, the unit for p_T is GeV/c.

2.2 Magnet System

In contrast to the CMS detector, where only one solenoidal field is used, the ATLAS detector employs a unique hybrid system of four superconducting magnets to provide the magnetic field for the inner tracking detector called Inner Detector and the muon spectrometer. The total size of the magnetic system in 22 m in diameter and 26 m in length. The stored energy in the system im 1.6 GJ.

Central solenoid

The central solenoid provides the solenoidal field for the momentum measurement in the Inner Detector. The solenoidal field is aligned with the beam axis and has a nominal strength of 2 T. The superconducting cables are made out of Al–stabilized NbTi. The central solenoid is located inside the electromagnetic barrel calorimeter. In order to achieve the required performance of the electromagnetic barrel calorimeter, the material budget of the central solenoid is crucial. A thickness of only 0.66 radiation lengths at normal incidence has been achieved.

Barrel toroid

The barrel toroid provides the toroidal field for the momentum measurement in the barrel part ($|\eta| < 1.4$) of the muon spectrometer. The bending power provided by the barrel toroid is 1.5 to 5.5 Tm. The eight coils of the barrel toroid are housed in eight separate cryostats. These are linked together by a support structure to deal with the Lorentz force which amounts to the equivalent of 1400 tonnes.

Endcap toroids

The two endcap toroids provide the toroidal field for the momentum measurement in the endcap part ($1.6 < |\eta| < 2.7$) of the muon spectrometer. The bending power provided by the endcap toroids is 1 to 7.5 Tm.

In the transition region ($1.4 < |\eta| < 1.6$) the magnetic fields of the barrel and the endcap toroids overlap and the provided bending power is lower than in the other regions.

2.3 Inner Detector

At the design luminosity of the LHC approximately 1000 particles will emerge from the collision point every 25 ns. The primary task of the Inner Detector is to measure the tracks of the charged particles. Based on these tracks, the Inner Detector will measure the transverse momentum of charged particles down to a transverse momentum p_T of 0.5 GeV/c. It will reconstruct the primary vertex as well as secondary vertices, e.g. from τ leptons, b–quarks or c–quarks, if present. Furthermore the Inner Detector will contribute to electron identification by measuring transistion radiation. The bending power required for the momentum measurement is provided by the central solenoid. The layout of the Inner Detector is shown in figure 2.3.

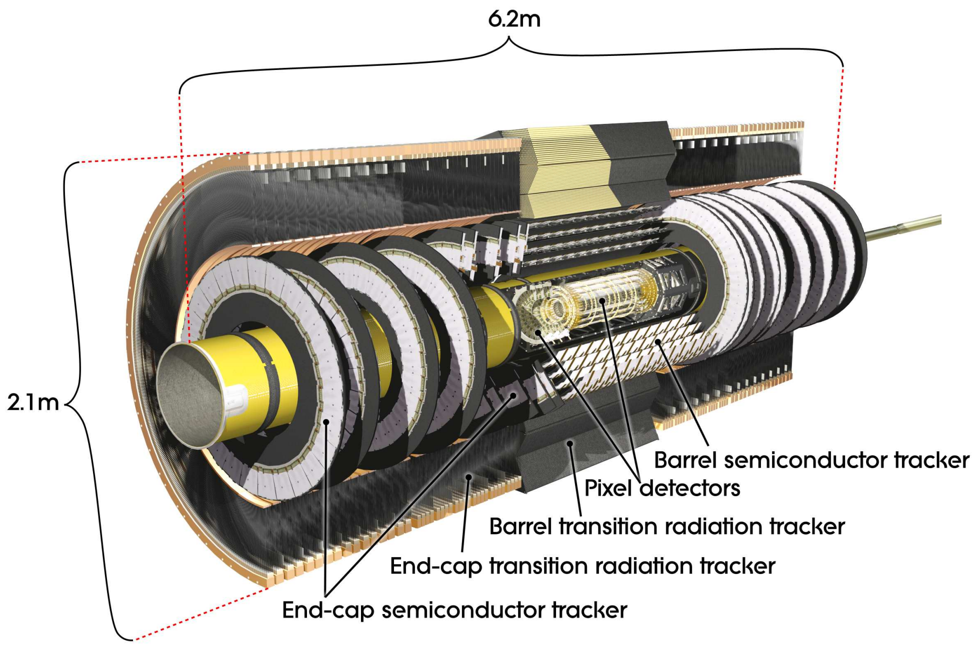

Figure 2.3: Cut-away view of the ATLAS Inner Detector. Taken from [5].

Pixel Detector

The Pixel detector is a sillicon detector consisting of 1744 pixels sensors with 46080 readout channels per sensor. The barrel part features three cylindrical layers, the two endcaps three discs each. The thickness is 250 μ with a nominal pixel size 50x400 μm^2. The Pixel detector will provide discrete space–points that will be used for high resolution tracking.

The standard bias voltage is 150 V, although after 10 years of operation up to 600 V will be needed for good charge collection to compensate the degradation of the performance due to radiation damage.

Silicon Microstrip Tracker

The Silicon Microstrip Tracker (SCT) is also a sillicon detector consisting of 15192 sensors with 768 strips per sensor. The barrel part features four cylindrical layers, the two endcaps 9 discs each. The thickness is 285 μm. The SCT will provide stereo pairs to the tracking algorithms.

The standard bias voltage is 150 V, although after 10 years of operation up to 350 V will be needed for good charge collection to compensate the degradation of the performance due to radiation damage.

Transition Radiation Tracker

The Transition Radiation Tracker (TRT) consists of polyimide drift tubes of 4 mm diameter. They are operated at 1530 V resulting in a gain factor of $2.5\text{x}10^4$ and provide $R - \varphi$ information only. The chosen gas mixture is 70% Xe, 27% CO_2 and 3% O_2 at 5-10 mbar over–pressure. The TRT covers the pseudorapidity range of $|\eta| < 2.0$ and has 351000 readout channels.

In addition to providing typically 36 hits per track to the tracking algorithms, the TRT also contributes to the electron identification. The low energy transition radiation photons emitted by traversing electrons are absorbed in the gas mixture and yield much larger signal amplitudes for electrons than for minimum ionizing charged particles. The electron identification capabilities are implemented by using a high threshold to detect the enhanced signal for electrons in addition to a low threshold for identifying standard hits for tracking.

2.4 Calorimetry

All calorimeters employed by ATLAS are sampling calorimeters. The electromagnetic (subsection 2.4.1) and hadronic (subsection 2.4.2) calorimeters cover the pseudorapidity range of $|\eta| < 4.9$. The layout of the calorimetry system is shown in figure 2.4.

2.4.1 Liquid Argon Electromagnetic Calorimeter

The Liquid Argon Electromagnetic Calorimeter is a sampling calorimeter using lead as the absorber and liquid argon as the active material. It consists of a barrel part ($|\eta| < 1.475$) and two endcaps ($1.375 < |\eta| < 3.2$). A special geometry (accordion) has been developed to provide complete φ symmetry without azimuthal cracks has been chosen for the barrel and the endcaps.

The Liquid Argon Electromagnetic Barrel Calorimeter (LAr EMB) is described in chapter 4 in more detail since the calibration of the electron energy measurement with the LAr EMB in the Combined Test Beam 2004 is the subject of chapter 5.

Each endcap consists of two co–axial wheel–like structures. The outer wheel (1.375 <

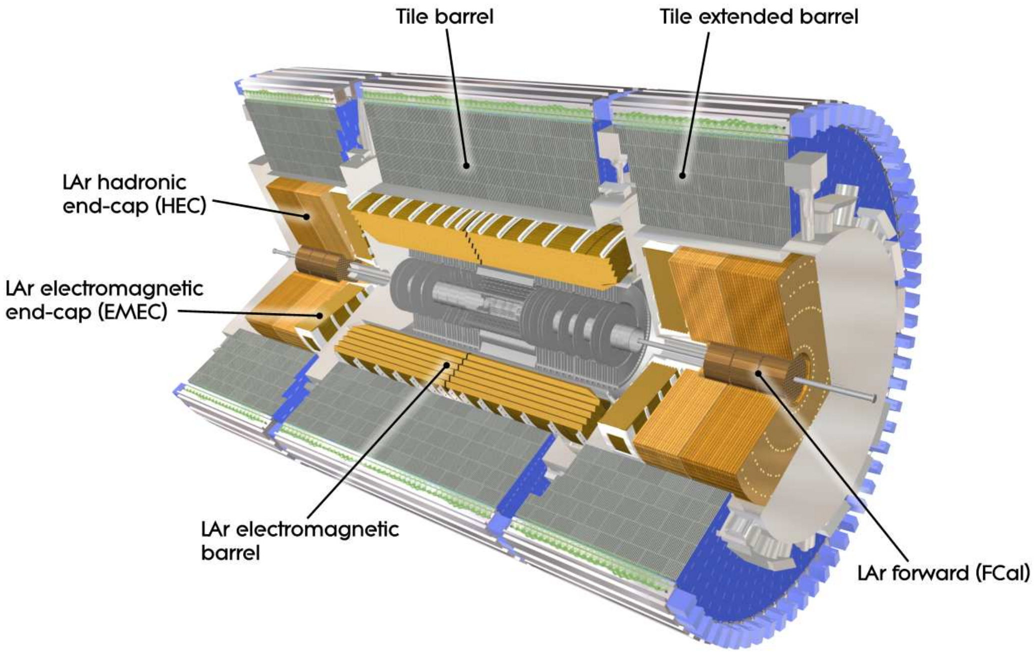

Figure 2.4: Cut-away view of the ATLAS calorimeter system. Taken from [5].

$|\eta| < 2.5$) and the inner wheel ($2.5 < |\eta| < 3.2$) are separated by a 3 mm gap whose position corresponds to the end of the acceptance of the Inner Detector. The precision region of the outer wheel ($1.5 < |\eta| < 2.5$) is segmented into three layers in depth, the other regions into two layers. For the region of $1.5 < |\eta| < 1.8$ a liquid argon presampler is used to estimate the energy loss in front of the calorimeter in order to improve the energy measurement. The thickness of the endcaps is at least 24 radiation lengths.

2.4.2 Hadronic Calorimeters

Tile calorimeter

The Tile Calorimeter consists of a barrel part ($|\eta| < 1.0$) and two extended barrels ($0.8 < |\eta| < 1.7$). It is a sampling calorimeter using iron as the absorber and scintillating tiles as the active medium. The tiles are readout at two sides by wavelength shifting fibres into two independent photomultiplier tubes. The tiles are oriented radially and normal to the beam axis providing an almost seamless azimuthal coverage. The Tile Calorimeter is radially segmented into three layers and its radial depth is 7.4 interaction lengths (λ). Together with the electromagnetic calorimeter this yields a depth of 9.7 λ of active material in the barrel region. This is sufficient to achieve the desired resolution for high energy jets (see table 2.1).

Liquid Argon Hadronic Endcap calorimeter

The Liquid Argon Hadronic Endcap calorimeter is a sampling calorimeter with liquid argon as active and copper as absorber material and covers the pseudorapidity range of $1.5 < |\eta| < 3.2$. It consists of two independent wheels per endcap and shares a common cryostat together with the electromagnetic endcap calorimeter and the Forward Calorimeter. Each wheel is divided into two segments in depth.

Liquid Argon Forward Calorimeter

The Liquid Argon Forward Calorimeter (FCal) is a sampling calorimeter and uses liquid argon as the active medium. For each endcap the FCal is segmented into three layers in depth, the first optimized for eletromagnetic measurements using copper as absorber material and the other two devoted to the measurement of the hadronic interactions using tungsten as absorber material. The covered pseudorapidity range is $3.1 < |\eta| < 4.9$.

2.5 Muon Spectrometer

The driving performance requirement for the muon spectrometer was a 10% momentum resolution for 1 TeV muon tracks. For these tracks the sagitta along the beam axis is approximately 500 μm given the bending power provided by the toroid magnet systems. In order to achieve the desired momentum resolution, the sagitta has to be measured with a precision of $\leq$50 μm. Due to the large volume of the muon spectrometer the relative alignment between the chambers is crucial for its overall performance. The precision of the relative alignment of chambers has to be 30 μm. Optical alignment sensors are used in addition to track–based alignment algorithms to meet this requirement.

The muon spectrometer covers a pseudorapidity range of $|\eta| < 2.7$ and can be used for triggering on muon tracks up to $|\eta| < 2.4$. The layout of the muon spectrometer is shown in figure 2.5.

Monitored Drift Tubes

The Monitored Drift Tubes (MDT) are drift tube chambers operating with a gas mixture of 93% Ar and 7% CO_2 at 3 bar. The drift time for the MDTs is 700 ns. They cover a pseudorapidity range of $|\eta| < 2.7$ ($|\eta| < 2.0$ for the innermost layer) and provide high

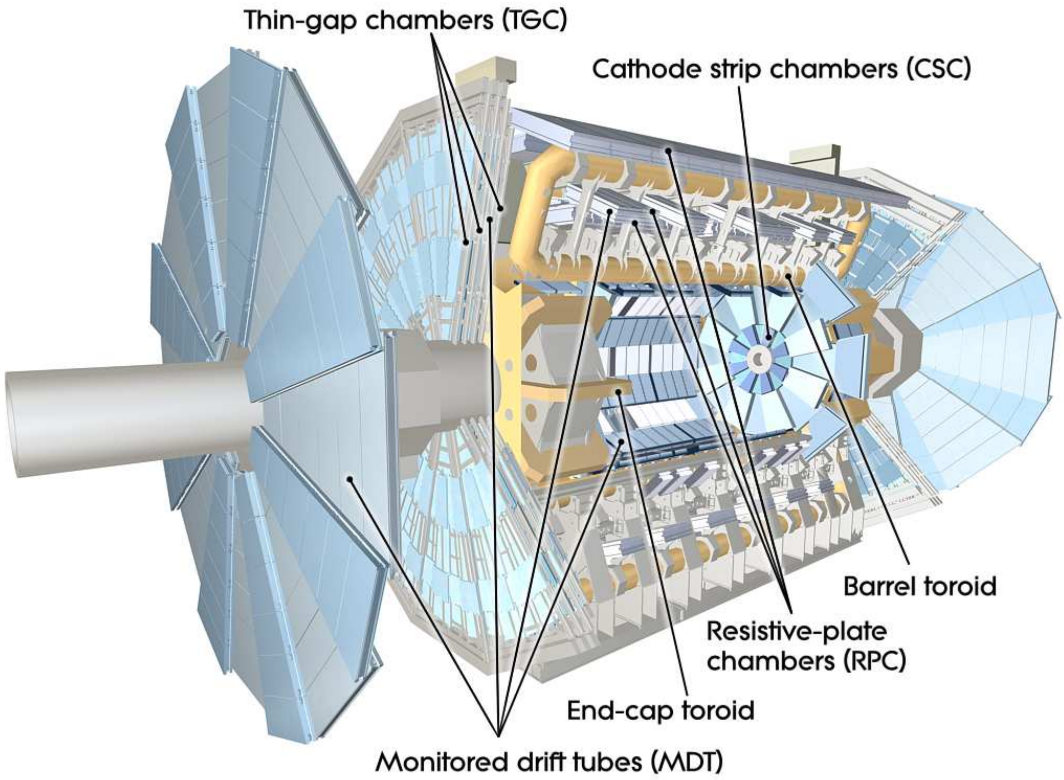

Figure 2.5: Cut-away view of the ATLAS muon system. Taken from [5].

precision measurements of the track coordinates.

There are 1150 MDT chambers with 354000 readout channels in total.

Cathode Strip Chambers

In the pseudorapidity range of $2.0 < |\eta| < 2.7$ in the innermost layer the MDT chambers are replaced by Cathode Strip Chambers (CSC) because of the high particle flux and muon track density. The CSCs are multiwire proportional chambers with the wires oriented in the radial direction. Both cathodes are segmented, one perpendicular and one parallel to the wire. The interpolation between the charges induced on neighbouring cathode strips are used to compute the position of the track.

Together with the MDTs the CSCs contribute to the precision tracking for muons. In total there are 32 CSC with 31000 readout channels.

Resistive Plate Chambers

In the pseudorapidity range of $|\eta| < 1.05$ Resistive Plate Chambers (RPC) are used to trigger on muon tracks. In addition they will provide a second coordinate measurement in the non–bending φ projection to complement the MDT measurement. The RPC is a parallel electrode–plate detector with a distance of 2 mm between the plates. It is filled with a gas mixture of 94.7% $C_2H_2F_4$, 5% Iso-C_4H_{10} and 0.3% SF_6 and operated at 4.9 kV/mm. The intrinsic time resolution for the RPCs is 1.5 ns. There are 606 RPCs with 373000 readout channels.

Thin Gap Chambers

In the pseudorapidity range of $1.05 < |\eta| < 2.4$ Thin Gap Chambers (TGC) are used to trigger on muon tracks. In addition they will provide a second coordinate measurement in the non–bending φ projection in the pseudorapidity range of $1.05 < |\eta| < 2.7$ to complement the MDT measurement. The TGCs are multiwire proportional chambers filled with a highly quenching gas mixture of 55% CO_s and 45% n–C_5H_{12} (n-pentane) and operated with a gas gain of $3\text{x}10^5$. The intrinsic time resolution for the TGCs is 4 ns. There are 3588 TGCs with 318000 readout channels.

3 Electromagnetic Calorimetry

This chapter describes the fundamental principles of electromagnetic calorimetry and is based on [6–8]. After discussing the energy loss of electrons while passing through matter in section 3.1 and the interaction of photons with matter in section 3.2, the principles of the development of the electromagnetic cascades are described in section 3.3. The deposition of the energy inside the absorber material is discussed in section 3.4 and, finally, the energy resolution of electromagnetic calorimeters is treated in section 3.5.

3.1 Energy loss of electrons

Since for high energy electrons, i.e. with an energy higher than the critical energy defined below, the emission of bremsstrahlung is the dominant process through which they loose energy when traversing matter (see figure 3.1 for the energy loss of electrons in lead), the characteristic length for the energy loss of high energy electrons in matter is the *radiation length* X_0 defined as the mean distance after which the remaining energy of the high energy electron is $1/e$ of its initial energy. A fit to experimental data yields the approximation [6]

$$X_0(\mathrm{g/cm^2}) = \frac{716\ \mathrm{g\ cm^{-2}}\ A}{Z\ (Z+1)\ \ln(287/\sqrt{Z})}, \tag{3.1}$$

where Z is the atomic mass and A is atomic number of the matter that is traversed. The differential cross section can be approximated by [6]

$$\frac{d\,\sigma}{d\,k} = \frac{A}{X_0\,N_A\,k}\left(\frac{4}{3} - \frac{4}{3}y + y^2\right), \tag{3.2}$$

where $y = k/E$ is the fraction of the electron's energy transfered to the radiated photon and N_A is Avogadro's number.

The *critical energy* E_c can be defined as the energy at which the energy losses due to

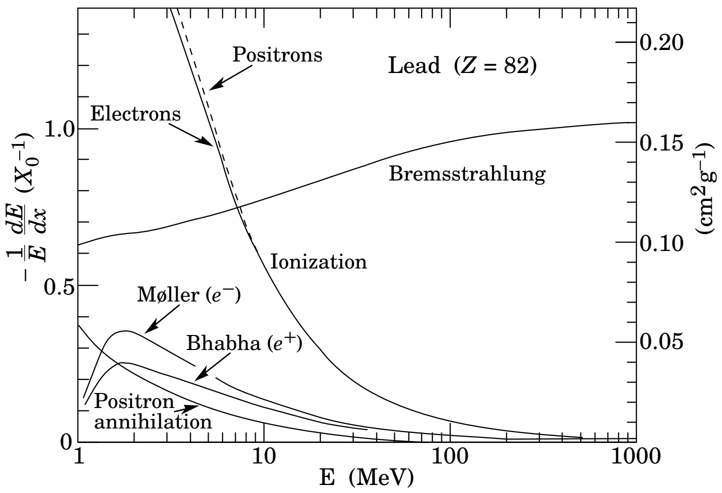

Figure 3.1: Fractional energy loss for electrons and positrons per radiation length in lead ($X_0(\mathrm{Pb}) = 6.37$ g/cm^2) as a function of the electron or positron energy. Taken from [6].

bremsstrahlung and ionization are equal. An approximation for E_c is given by

$$E_c = \frac{610\ (710)\ \mathrm{MeV}}{Z + 1.24\ (0.92)} \tag{3.3}$$

for solid (gaseous) absorber materials.

3.2 Interactions of photons with matter

The cross section of the various interactions of photons with lead are shown in figure 3.2. For high energies pair production in the nuclear field is the dominant process and its cross section can be approximated by

$$\sigma = \frac{7\,A}{9\,X_0\,N_A}, \tag{3.4}$$

where X_0 denotes the radiation length of the material through with the photon travels (see section 3.1), A is the atomic mass of the traversed matter and N_A is Avogadro's number. This means that after traversing a length of $\frac{9\,X_0}{7}$ the probability of a photon to convert into an electron–positron pair is $1 - 1/e$, or, in other words, $1/e$ that it has not converted.

Therefore a common length scale, the radiation length, governs the interactions for electrons and photons at high energies.

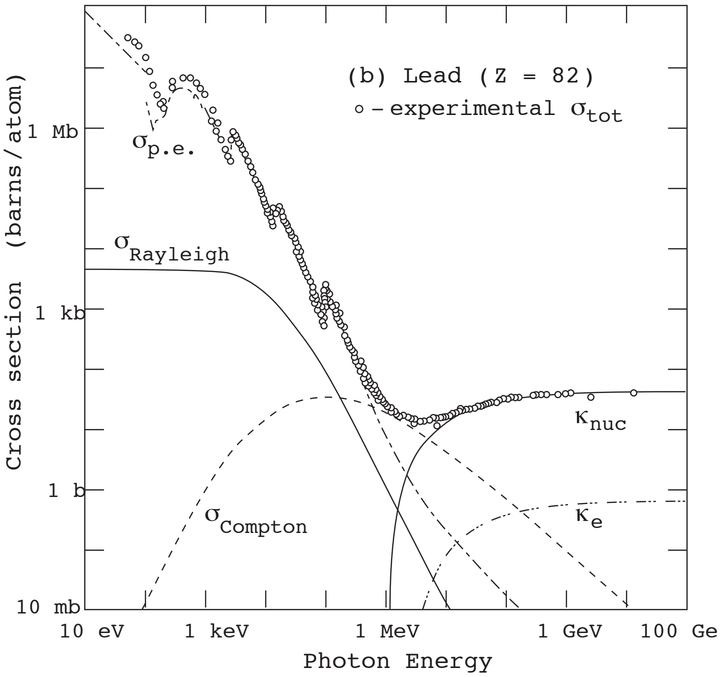

Figure 3.2: Total cross sections for photons in lead as a function of the photon energy. $\sigma_{\text{e.p.}}$ is the cross section for the atomic photoelectric effect, σ_{Rayleigh} and σ_{Compton} for the (coherent) Rayleigh scattering and the (incoherent) Compton scattering, κ_{nuc} and κ_{e} for the pair production in the nuclear field and the electron field. Taken from [6].

3.3 Electromagnetic cascades

As shown in sections 3.1 and 3.2, the dominant process for high energy electrons is bremsstrahlung and for high energy photons it is pair production. Both processes have a common characteristic length scale, the radiation length of the absorber material.

For a high energy electron impinging a block of matter this means that it will most likely emit a bremsstrahlung photon which itself will convert via pair production into an electron–positron pair. This electron and positron will themselves emit bremsstrahlungs photons, which will also convert. This results in a whole cascade of bremsstrahlung and pair production events that create a shower of electrons/positrons and photons. This mechanism is called *electromagnetic cascade* and its main properties can be characterized by the radiation length X_0 of the absorber material.

The mean longitudinal shower profile obtained from Monte Carlo simulation is shown in figure 3.3. It can be described with the so-called Longo–Sestilli formula [9]

$$\frac{dE}{dt} = E_0\, b \frac{(bt)^{a-1} e^{-bt}}{\Gamma(a)}, \tag{3.5}$$

where E_0 denotes the initial energy of the incident particle, $t = x/X_0$ is the depth inside the material in radiation lengths and the parameters a and b depend on the type of the incident particle, i.e. whether it is an electron, a positron or a photon.

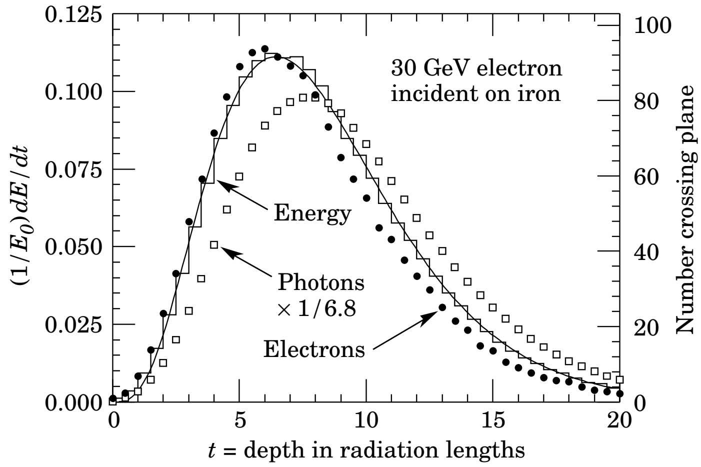

Figure 3.3: Fractional energy deposition of a 30 GeV electron–induced electromagnetic cascade in iron obtain with Monte Carlo simulation (EGS4). Circles indicate the number of electrons with total energy greater than 1.5 MeV crossing planes at $X_0/2$ intervals (scale on the right) and the squares the number of photons with an energy greater than 1.5 MeV crossing the planes (scaled down to have the same area as the electron distribution). Taken from [6].

The mean position t_{max} of the shower maximum can be approximately described by

$$t_{max} \approx \ln \frac{E_0}{E_c} + t_0, \tag{3.6}$$

with t_{max} in radiation lengths, E_0 denotes the initial energy of the incident particle and t_0 depends on the type of the incident particle, i.e. 0.5 for electrons/positrons and -0.5 for photons. Equation 3.6 shows that the mean position t_{max} of the shower maximum scales logarithmically with the initial energy

The depth range $[0, t_{95\%}]$ where on average 95% of the energy of the incident particle is deposited, is approximately given by

$$t_{95\%} = t_{max} + 0.08\,Z + 9.6. \tag{3.7}$$

As t_{max}, $t_{95\%}$ scales logarithmically with the initial energy making it feasible to build calorimeters for very high energies.

3.4 Energy deposition

During the electromagnetic cascade by bremsstrahlung and pair production processes, the energy of the initial particle is distributed among all the shower particles; energy is deposited in the material mostly by ionization and excitation.

3.5 Energy resolution of electromagnetic calorimeters

The basic working principle of calorimetry is the measurement of the energy of an incident particle through total absorption of the particle and its shower.

Therefore and due to the fact that the energy is mainly deposited by ionization and excitation, the measured energy E for an incident electron with initial energy E_0 is in first order proportional to the sum T_0 of the lengths of all charged tracks in the electromagnetic cascade, also denoted the total track length,

$$E \propto T_0. \tag{3.8}$$

The total track length itself is proportional to the inital energy E_0

$$T_0 \propto E_0. \tag{3.9}$$

Under the assumption that the total track length T_0 is Poisson distributed, its standard deviation is $\sigma_{T_0} = \sqrt{T_0}$. Putting this together with equations 3.8 and 3.9 and dividing by the initial energy to obtain the resolution of the energy measurement due to fluctuations of the electromagnetic cascade as a function of the initial energy E_0 yields

$$\frac{\sigma_E(E_0)}{E_0} \propto \frac{1}{\sqrt{T_0}} \propto \frac{1}{\sqrt{E_0}}. \tag{3.10}$$

For a realistic calorimeter the resolution of the energy measurement for an incident electron with initial energy E_0 can be described by

$$\frac{\sigma_E(E_0)}{E_0} = \frac{a}{\sqrt{E_0}} \oplus \frac{b}{E_0} \oplus c \tag{3.11}$$

where $\oplus$ denotes quadratic summation. The three terms on the right hand side are discussed in the following subsections.

3.5.1 Stochastic term

The first term on the right hand side of equation 3.11 is denoted *stochastic term* and describes the contribution of the stochastic fluctuations of the energy deposition of the electromagnetic cascade. For *homogenous calorimeters*, i.e. calorimeters where the energy reduction and the signal generation occur in the same material, a is typically a few $\%\,\mathrm{GeV}^{\frac{1}{2}}$. For *sampling calorimeters*, i.e. calorimeters where the main energy absorption and the signal generation occur in alternating layers of absorber and active material, the fraction of the energy deposited in the active medium wrt. the total energy deposit fluctuates from event to event. The number of charged particles N_{ch} that cross the active layers of the sampling calorimeter is proportional to the initial energy E_0 of the incident particle and inversely proportional to the thickness of the absorber layers t_l

$$N_{ch} \propto \frac{E_0}{t_l}. \tag{3.12}$$

Applying the same arguments as for the derivation of equation 3.10 leads to

$$\frac{\sigma_E(E_0)}{E_0} \propto \frac{1}{\sqrt{N_{ch}}} \propto \sqrt{\frac{t_l}{E_0}}. \tag{3.13}$$

This implies that by decreasing the thickness of the absorber layers t_l the resolution can be improved. In reality this approach is limited by external factors like the constraints of the fabrication process.

Typical values of a for sampling calorimeters are 5-20$\%\,\mathrm{GeV}^{\frac{1}{2}}$.

3.5.2 Noise term

The second term on the right hand side of equation 3.11 is denoted *noise term* and describes the contribution of the electronic noise of the read–out chain.

A theoretical limit can be set by the thermal noise before the preamplifier. The equivalent noise charge Q of the electronic noise induced by the thermal noise is given by

$$Q = \sqrt{4\, k_B\, T\, R\, \delta F} \tag{3.14}$$

where k_B is Boltzmann's constant, T the temperature, R the equivalent noise resistance of the preamplifier and δF the bandwidth. High rates imply a high bandwidth which means – applying equation 3.14 – a large noise.

For sampling calorimeters, the *sampling fraction* has an impact on the noise term. The sampling fraction f_{samp} is defined by

$$f_{\text{samp}} = \frac{E_{mip}^{active}}{E_{mip}^{active} + E_{mip}^{absorber}} \tag{3.15}$$

where E_{mip}^{active} and $E_{mip}^{absorber}$ denote the energy deposited by a minimum ionizing particle in active and in the absorber material.

Increasing the sampling fraction means a larger signal from the active medium, which means a higher signal–to–noise ratio which leads to a decrease of the noise term.

Typical values of b are 50 MeV per readout channel for calorimeters designed for energies of several GeV and 150–300 MeV per readout channel for calorimeters designed for energies up to several TeV.

3.5.3 Constant term

The last term on the right hand side of equation 3.11 is denoted *constant term* and describes the nonuniformity coming from variations of the response of the calorimeter wrt. the impact position of the particle.

Possible sources of these variations are irregular detector geometries, temperature gradients (of the order of 0.3 K for the ATLAS Liquid Argon calorimeter), radiation damage or imperfectly calibrated detector regions.

Typical values of c are $\leq$1%.

4 The ATLAS Electromagnetic Barrel Calorimeter

The ATLAS Electromagnetic Barrel Calorimeter is the central part of the ATLAS Electromagnetic Calorimeter covering the pseudorapidity range of $|\eta| < 1.4$. The main purpose of the ATLAS Electromagnetic Barrel Calorimeter is the precision measurement of electrons and photons. The measured quantities include the energy, the position as well as the longitudinal and lateral shower shape. In addition it measures the first part of hadronic showers as part of the ATLAS calorimeter system.

The performance requirements are presented in section 4.1, the design of the ATLAS Electromagnetic Barrel Calorimeter is discussed in section 4.2 and the shape of the signals produced by the traversing particles is shown in section 4.3.

4.1 Performance requirements

The required resolution [10] for the ATLAS Electromagnetic Barrel Calorimeter is

$$\sigma_E/E = 10\%\,\mathrm{GeV}^{\frac{1}{2}}/\sqrt{E} \oplus c/E \oplus 0.7\% \tag{4.1}$$

where the global constant term 0.7% is determined by the local constant term and the uniformity of the detector. The term c is the noise term which contains the electronic noise contribution (∼200 MeV in the barrel) and the pile–up noise contribution that depends on the luminosity.

The electromagnetic showers must be contained very well in order to reduce the impact of longitudinal leakage on the resolution. The chosen minimal thickness was 22 radiation length.

A good angular resolution is required especially for photons. The computation of the invariant mass for decays like H→ $\gamma\gamma$ has to rely on the angular measurement between the photons from the calorimeter since the photons leave no track in the Inner Detector.

The requirement on the absolute energy scale clearly depends on the given physics process to be studied. For most measurements and searches the absolute energy scale has to be known with a precision of at least 0.5%; however, for some precision measurements the accuracy of the absolute energy scale has to be for better, e.g. 0.02% for the W boson mass measurement [11].

4.2 Design

The Liquid Argon Electromagnetic Barrel Calorimeter is a sampling calorimeter using lead as the absorber and liquid argon as the active material. It covers the pseudorapidity range of $|\eta| < 1.4$ and consists in total of approximately 110.000 read–out channels [12].

4.2.1 Accordion geometry

In contrast to most of the calorimeters used for high energy physics where the absorber layers are positioned in such a way that the particles impinge approximately perpendicularly, the ATLAS Electromagnetic Barrel Calorimeter is designed using the so called *accordion geometry* which is shown in figure 4.1. The absorber layers and the electrodes are shaped like an accordion with the folds approximately perpendicular to the incoming particle. This geometry allows to route the signal and high voltage cables in the front as well as in the back of the detector volume. As a consequence the calorimeter has a seamless geometrical coverage in φ and exhibits no gaps whatsoever for services. Furthermore the cell boundaries are chosen in a way that they point towards the interaction point.

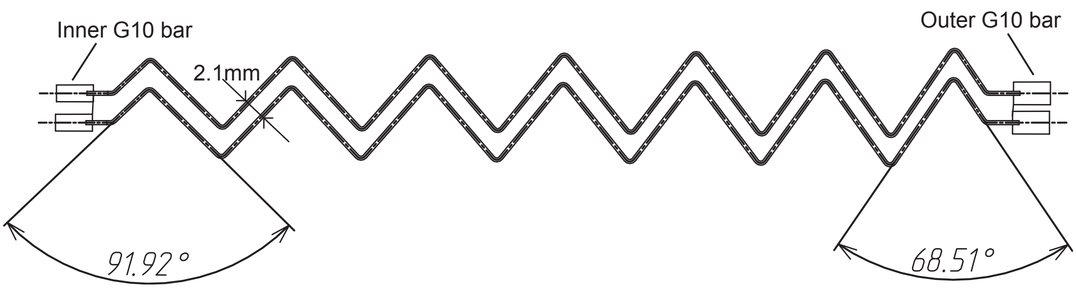

Figure 4.1: Accordion geometry of the absorber.

The gap between the absorber layers and the electrodes is filled with liquid argon. The layout is presented in figure 4.2. The absorber is made out of a steel–lead sandwich of a thickness of 2.2 mm. The lead sheet is 1.53 mm thick for $\eta < 0.8$ and 1.13 mm for $\eta > 0.8$. The width of the liquid argon gap is 2.12 mm for each side of the read-out electrode. The read-out electrodes consist of three copper layers that are glued together and are separated by Kapton layers. The inner layer acts as the signal layer and is isolated from the other two high voltage layers. The nominal setting for the potential between the electrode high voltage layers and the absorbers (ground) is 2000 V.

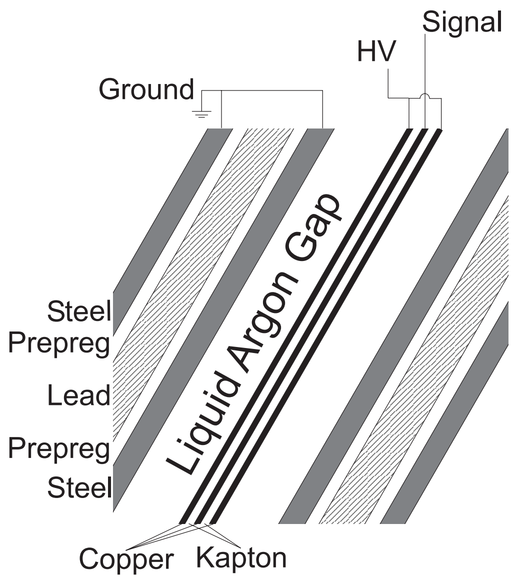

Figure 4.2: Schematic layout of the absorber, the liquid argon gap and the read-out electrode (three layers glued together).

The signal is induced in the read-out electrodes by the drift of the ionization electrons in the electric field created by the high voltage.

4.2.2 Presampler

Since there is a significant amount of material in front of the electromagnetic calorimeter, the amount of energy deposited in this material has to be estimated. This is done using a presampler that is placed in front of the accordion calorimeter.

The presampler is a thin (11 mm) active layer of liquid argon enclosed by a 0.4 mm thin glass-epoxy shell.

The procedure how the presampler is used to estimate the energy deposited upstream electromagnetic calorimeter is described in section 5.7.1

4.2.3 Granularity

The ATLAS Electromagnetic Barrel Calorimeter is longitudinally segmented into three layers, called the strip, middle and back layer or also sampling 1, sampling 2 and sampling 3. A sketch is shown in figure 4.3.

The granularity in the $\eta - \varphi$ plane is different for the three layers and reflects the trade–offs between the required position resolution and shower shape identification on the one side and the number of readout channel on the other. The granularity of the strip layer is very fine in η, providing a good angular resolution in the η direction and π^0 rejection capabilities. The middle cells are also used for seeding clusters for the trigger since most of the energy is deposited in this layer for electrons and photons above approximately 10 GeV (depending on η).

The thickness of the ATLAS Electromagnetic Barrel Calorimeter varies from 22 radiation lengths (barrel) to 33 radiation lengths (gap region).

Layer	$\Delta\eta$	$\Delta\varphi$	Depth (radiation lengths)
Strip	0.025/8	$2\pi/64$	2.5-4.5
Middle	0.025	$2\pi/256$	16.5-19
Back	0.05	$2\pi/256$	1.4-7

Table 4.1: Granularity for the three layers of the ATLAS Electromagnetic Barrel Calorimeter.

4.3 Signal shape

The signal is induced by the drift of the ionization electrons in the electric field in the liquid argon gaps. Its approximately triangular shape is shown in figure 4.4(a).

Right after the signal is amplified by the preamplifier it is transformed by a shaping amplifier in order to optimize the signal-to-noise ratio. The triangular signal is transformed into a narrow peak and a long undershoot (see figure 4.4(b)). The signal is sampled only in the vicinity of the peak because the amplitude of the peak is proportional to the energy deposit in the cell [13]. The calibration of the read out chain is discussed in section 5.5.

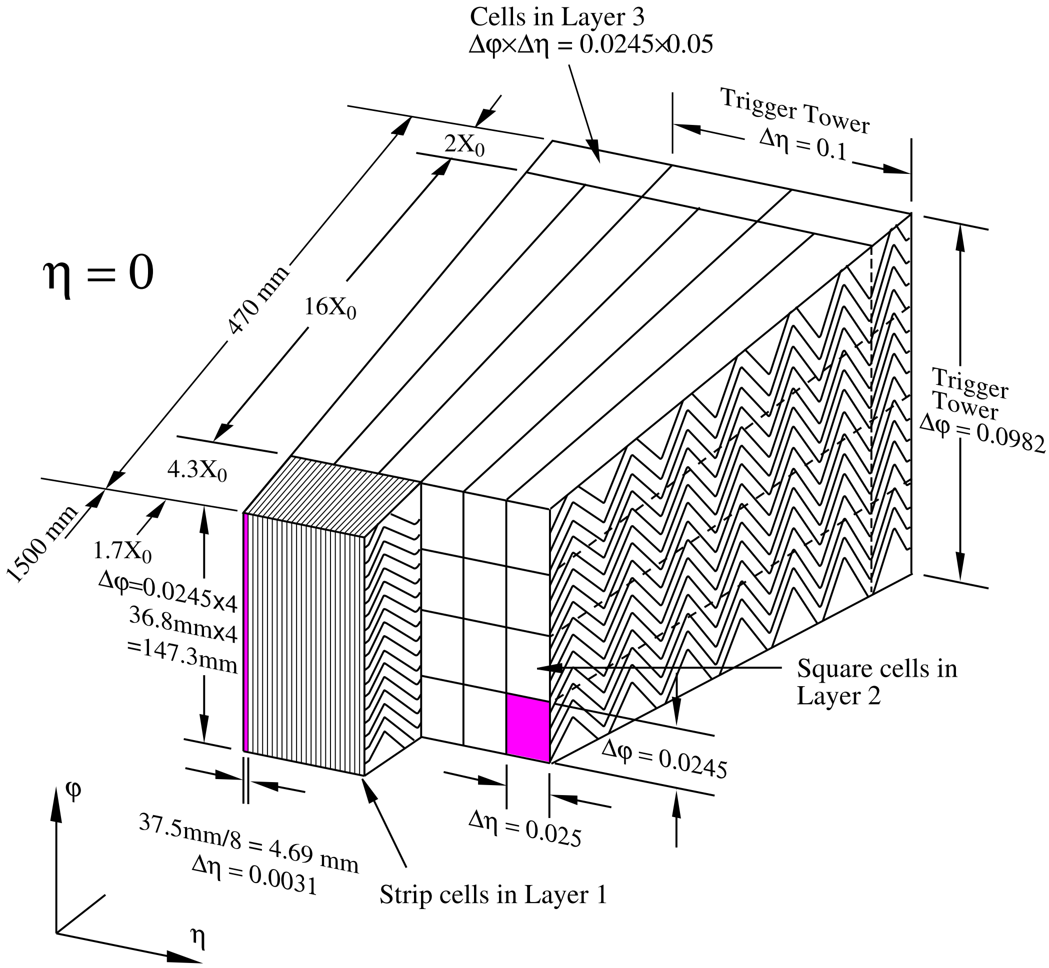

Figure 4.3: Sketch of a barrel module of the electromagnetic calorimeter. The accordion structure and the granularity in η and φ of the cells of each of the three layers is shown.

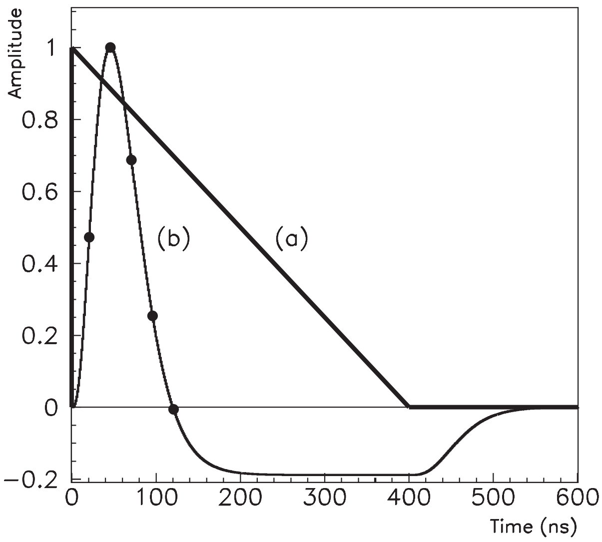

Figure 4.4: Signal (a) induced by the drift of the ionization electrons in the electric field in the liauid argon gaps and the signal after shaping (b). The black circles indicate the sampling points of the shaped signal.

5 Calibrating the Electron Energy Measurement for the Combined Test Beam 2004

This chapter describes the calibration of the electron energy measurement for the Combined Test Beam (CTB) 2004 in the presence of a magnetic field in the Inner Detector. The whole calibration chain for the electron energy measurement in ATLAS consists of the following three consecutive steps:

1. Calibration of the readout channels, also called *electronic calibration*.
2. Calibration of the energy response of the whole electromagnetic calorimeter.
3. Further calibration using physics events in ATLAS from LHC collision data, e.g. electrons from Z→ee decays to calibrate the absolute scale or inclusive electrons using E/p to calibrate the relative scale between the Inner Detector and the electromagnetic calorimeter.

This chapter focuses on calibration of the energy response of the whole electromagnetic calorimeter (item 2) and therefore the term *calibration* will be used in this chapter for this aspect of the calibration chain.

For an electron impinging the detector a cluster of cells, i.e. readout channels, is formed and associated to the electron. Based on the energies from the cells in the cluster the inital energy, denoted calibrated cluster energy, of the electron is computed. The sequence of procedures for this computation is shown in figure 5.1.

After a brief description of the setup (section 5.1) and the data samples (section 5.2), the event selection (section 5.3) and beam related weighting procedures (section 5.4) are presented. Section 5.5 recapitulates the way the energy deposited in a single calorimeter cell is measured and how clusters are formed out of these cells. This is followed by a comparison of the Monte Carlo simulation to data (section 5.6). Finally a Monte Carlo

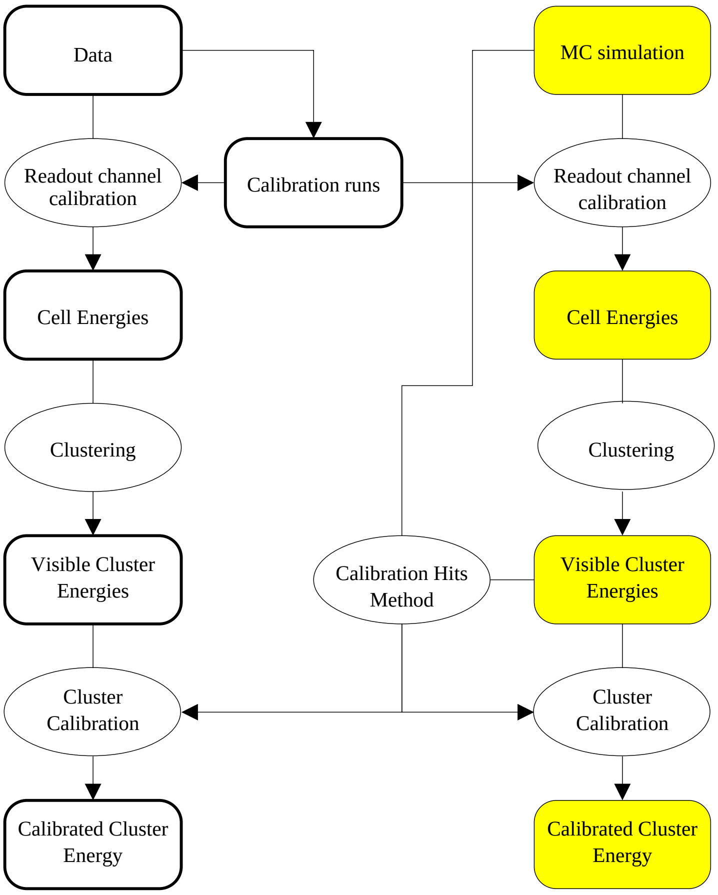

Figure 5.1: Sequence of procedures to compute the calibrated cluster energy. The *Readout channel calibration* and the *Clustering* are briefly discussed in section 5.5. The *Calibration Hits Method* and *Cluster calibration* are presented in section 5.7. Monte Carlo simulation to data comparisons are discussed in section 5.6 for the *Visible Cluster Energies* and in section 5.8 for the *Calibrated Cluster Energy*.

based calibration procedure for the cluster energy is presented in section 5.7 and applied to data in section 5.8 in order to extract the linearity and resolution for the liquid argon calorimeter in the presence of a magnetic field in the Inner Detector.

5.1 The Combined Test Beam 2004

During the Combined Test Beam 2004 data was taken from June until November 2004. The data that is used in this thesis comes from the last data taking period where all sub detectors participated. A sketch of the fully combined setup is shown in figure 5.2, including the coordinate system for the CTB 2004. A detailed description of the CTB

2004 can be found in [14]. The fully combined setup consisted of the following compo-

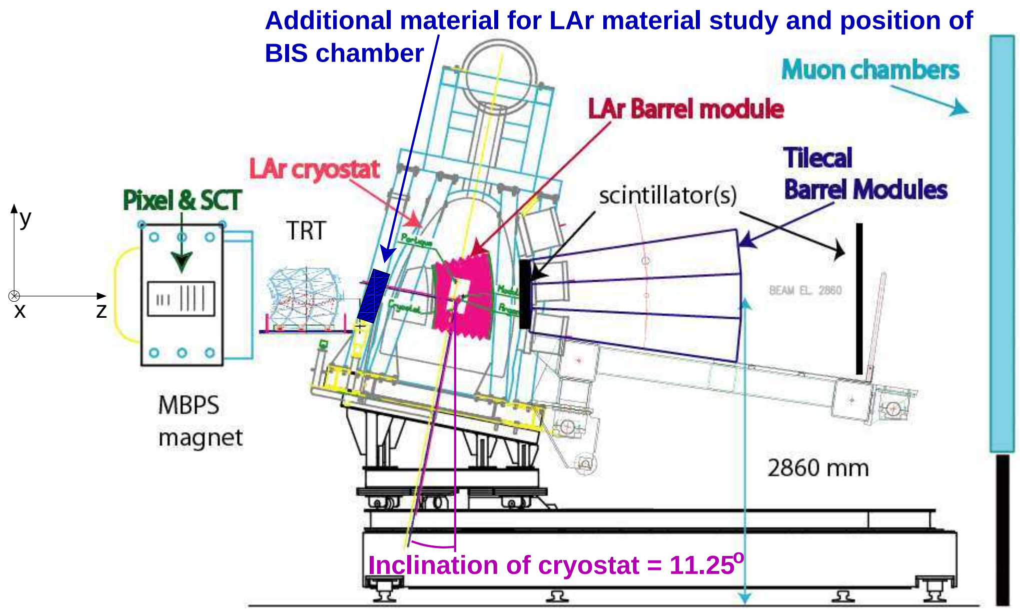

Figure 5.2: Setup of the Combined Test Beam 2004.

nents [15]:

Pixel detector Two modules for each of the three pixel layers (B, 1 and 2 as defined in [16]), adding up to six pixel modules in total.

Semiconductor Tracker (SCT) Two modules for each of the four layers of the SCT [17], meaning 8 modules in total.

Transition Radiation Tracker (TRT) Two barrel wedges, constituting 1/8 of a barrel wheel [18].

LAr electromagnetic barrel calorimeter (LAr EMB) One module, constituting 1/16 of a barrel wheel [19].

Tile calorimeter Three long barrel modules and three extended barrel modules, constituting 3/98 of a barrel wheel [20].

Muon spectrometer Three stations of monitored drift tube barrel chambers and three stations of monitored drift tube endcap chambers. For some runs, including the runs used in this analysis, a monitored drift tube BIS type chamber was positioned in front of the LAr EMB cryostat.

The CTB 2004 setup included a magnet in order to evaluate the performance of the various detector sub systems in the presence of a solenoidal magnetic field in the Inner Detector like it will be the case for the full ATLAS detector taking data from LHC collisions. The MBPS magnet produced a field for the pixel and SCT modules. The magnetic field was directed in such a way that charged particles passing through the pixel and SCT detector were deviated in φ (angle in the y–z plane). Contrary to the full ATLAS setup, the TRT was not positioned inside the magnetic field.

In order to be able to measure the response of the calorimeters to particles impinging at different η[1] positions the electromagnetic and hadronic calorimeter modules were mounted on a movable table that could be rotated in θ (angle in the x–z plane) and translated along the x–direction.

The electrons for the runs that are used in this analysis have been provided by the CERN H8 beam line. The H8 beam is created by directing 400 GeV/c protons from the CERN Super Proton Synchrotron (SPS) onto a primary target made of up to 300 mm of Beryllium. The emerging secondary beam has momenta between 9 GeV/c and 350 GeV/c. The beam line that uses this beam is called the high energy beam line.

A sketch of the H8 beam line instrumentation is shown in figure 5.3, a detailed description is given in [21]. The high energy beam line was equipped with two Čerenkov counters. CHRV1 was furthest upstream and is not shown in figure 5.3. CHRV2,HE was located 1 m upstream of the last bending magnet of the VLE spectrometer. The beam profile was determined using four beam chambers (BC-1, BC0, BC1 and BC2). The main trigger consisted of three scintillators (S1, S2 and S3). In order to reject muon halo from the beam a scintillator (SMH) with a hole of 3.4 cm in diameter was used in anti-coincidence with S1,S2 and S3.

The momentum selection for the high energy beam line is performed using a spectrometer consisting of two collimators and two triplets of bending magnets [14].

The momentum selection for the high energy beam line is done 400 m upstream of the Combined Test Beam 2004 setup. Between the collimator that performs this selection and the setup, the beam particles traverse air, four *mylar* windows of two beam pipes and one Čerenkov counter CHRV1. These contributions add up to 15% of a radiation length and are collectively denoted as *far upstream material*. Since the beam line optic for these 400 m has been designed for the nominal beam momentum and the fact that

[1]The pseudo rapidity η is defined by $\eta = -\ln\tan\frac{\theta}{2}$ where θ is the angle in the x–z plane.

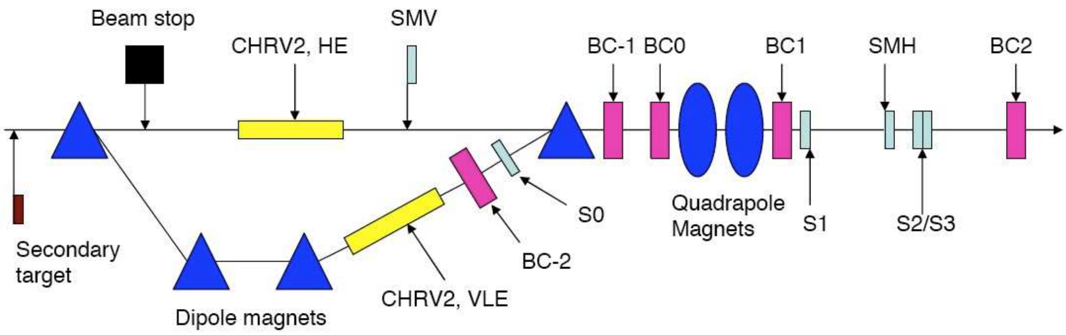

Figure 5.3: H8 beam line instrumentation. The straight line represents the high energy beam line that was used for the data analyzed in this thesis.

Run number	$p_{beam}^{nominal}$ (GeV/c)	$\eta^{nominal}$	MBPS current (A)	Events	$< p_{beam} >$ (GeV/c)	$\sigma(p_{beam})$ (GeV/c)
2102399	100	0.45	-850	200000	99.80 $\pm$ 0.11	0.24
2102400	50	0.45	-850	200000	50.29 $\pm$ 0.10	0.12
2102413	20	0.45	-850	70000	20.16 $\pm$ 0.09	0.05
2102452	80	0.45	-850	200000	80.0 $\pm$ 0.10	0.19

Table 5.1: Run number, nominal beam momentum, nominal η impact position, current in the MBPS magnet that provides the field for the inner detector, total number of events taken, estimated average beam momentum and beam spread for the data samples used in this analysis.

some particles loose energy (and therefore momentum) while traversing the far upstream material, the acceptance of this part of the beam line has to be taken into account in the simulation. This is described in subsection 5.4.1.

5.2 Data samples

The data samples that were taken during the CTB 2004 and used for the analysis in this thesis are listed in table 5.1. The average beam momentum $< p_{beam} >$ and the beam spread $\sigma(p_{beam})$ was computed for each run using the collimator currents from the beam momentum selection spectrometer described in section 5.1.

5.3 Event selection

This section describes the event selection procedure for the CTB 2004. Subsection 5.3.1 is devoted to particle identification for electrons, subsection 5.3.2 describes the requirements concerning the beam quality and subsection 5.3.3 deals with detector imperfections. Finally subsection 5.3.4 discusses the quality requirements for reconstructed electron–like objects.

5.3.1 Particle identification

The purpose of the procedures described in this subsection is to select only events for the analysis that are triggered from an electron from the beam entering the calorimeter. Requirements concerning measurement variables from the beam line instrumentation present only in the data samples are only applied there. Requirements that involve measurement variables from the calorimeters or the inner detector are applied both to the data and to the simulation samples in order to avoid introducing any bias. Where this has not been possible it is explicitly stated.

The following requirements have to be met for an event to be accepted:

1. Less than 700 MeV are deposited in the first tile calorimeter layer. The purpose of this requirement is to reject pions.

2. Less than one percent of the energy deposited in the calorimeters is deposited in the tile calorimeter. The purpose of this requirement is to reject pions.

3. There must be at least 20 hits in the TRT. The purpose of this requirement is to be sure to have a good track in the TRT.

4. TRT High Level Hit Probability>0.15: The purpose of this requirement is to reject pions and muons. This requirement is applied only to the data samples, since the TRT High Level Hit Probability is not correctly modeled in the simulation, and only electrons have been simulated.

5. Trigger from the trigger scintillators S1$\wedge$S2: This requirement guarantees that only beam particle triggered events are considered and not random tirggers that were injected to measure pedestal levels. Since the trigger scintillators are not simulated, the requirement is applied only to the data samples.

6. Muon halo veto scintillator (SMH) $<$ 460 ADC: The purpose of this requirement is to reject muons. Since the muon halo veto scintillator is not simulated, the requirement is applied only to the data samples.

7. Cherenkov counter CHRV2,HE $>$ 650 ADC: The purpose of this requirement is to reject pions for the run at 20 GeV/c nominal beam momentum. Since the

cherenkov counter is not simulated, the requirement is applied only to the data samples.

5.3.2 Beam quality

Two additional cuts[2] are applied to the data to ensure that only particles from the central part of the beam and no particles from the beam halo are used.

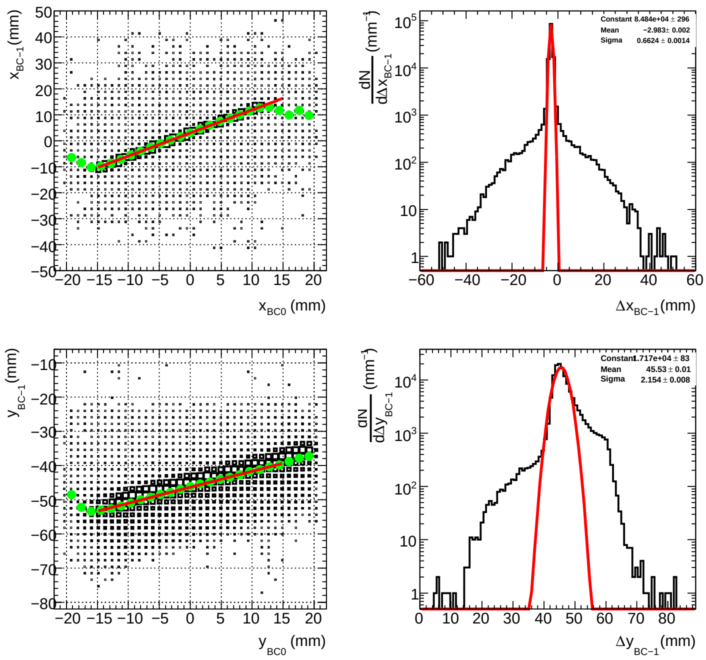

Figure 5.4: Beam chambers BC-1 vs. BC0 x (top left) and y (bottom left) measurements with fitted line. Distribution of the orthogonal distances ($\Delta x_{\text{BC-1}}$ and $\Delta y_{\text{BC-1}}$) from this line for x (top right) and y (bottom right) values together with a Gaussian fitted to the core of the distribution.

1. The x values measured by the beam chambers BC-1 and BC0 are linearly correlated since the setup is rigid and there is no magnetic field in the flight path between these two beam chambers. The same is true for y values. The left plots of figure 5.4 show the distributions for x and y. A line is fitted to each of the distributions and the orthogonal distances ($\Delta x_{\text{BC-1}}$ and $\Delta y_{\text{BC-1}}$) are plotted in the right plots of figure 5.4. Gaussians are fitted to the orthogonal distance distributions and 3 times the σ of a Gaussian is defined as the largest allowed absolute orthogonal

[2]The term *cut* refers to a requirement to has to be fulfilled for an event to be considered for the analysis. If the requirement is not fulfilled, the event is *cutted* away from the analysis.

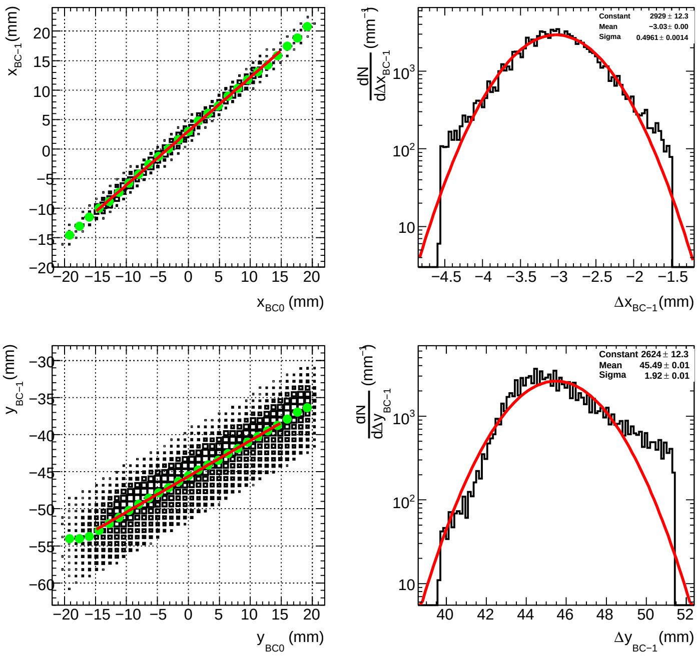

Figure 5.5: Beam chambers BC-1 vs. BC0 x (top left) and y (bottom left) measurements with fitted line with 3σ cut applied. Distribution of the orthogonal distances ($\Delta x_{\text{BC-1}}$ and $\Delta y_{\text{BC-1}}$) from this line for x (top right) and y (bottom right) values together with a Gaussian fitted to the core of the distribution.

$p_{beam}^{nominal}$ (GeV/c)	(min,max) $BC1_x$ (mm)	(min,max) $BC1_y$ (mm)
20	$(-15, +7)$	$(-13, +12)$
50	$(-15, +5)$	$(-15, +15)$
80	$(-5, +7)$	$(-10, +10)$
100	$(-15, +7)$	$(-15, +15)$

Table 5.2: Allowed ranges for the x and y values (denoted $BC1_x$ and $BC1_y$) of beam chamber BC1 for all beam momenta.

distance. The x and y distributions and the corresponding orthogonal distance distributions with these cuts applied are shown in figure 5.5.

2. The x and y values (denoted $BC1_x$ and $BC1_y$) of beam chamber BC1 are restricted to ranges where the total visible energy in the electromagnetic calorimeter is flat with respect to $BC1_x$ and $BC1_y$. The intervals used are given in table 5.2.

5.3.3 Detector imperfections

This subsection describes the procedures to discard events that have been affected by detector imperfections.

Coherent noise in the presampler

This cut is used to reject events with coherent noise in the presampler layer. In order to achieve this, the distribution of the presampler cell energies of all cells outside the region where the beam hits the calorimeter is considered, i.e. $|\eta_{cell} - \eta_{beam}| > 0.2$. If there is no coherent noise present, this distribution is a Gaussian with mean equal to 0 and an rms equal to the average noise of the cells. Let n^+_{PS} denote the number of presampler cells with positive energy and n^-_{PS} the number of presampler cells with negative energy. An event is rejected if $\left|\frac{n^+_{PS}-n^-_{PS}}{n^+_{PS}+n^-_{PS}}\right| > 0.6$. Since the coherent noise is not simulated this cut is only applied to the data samples.

Shaper problem

The cells at $0 < \varphi_{cell} < 0.1$, $\eta_{cell} = 0.3875$ in the middle layer suffered from an unstable signal shaper. The stochastic distortion of the signal shape introduced a variation of the order of 3% for the gain values. Although the effect on the reconstructed cluster energy is fairly small, all events with clusters that contain any of these cells are discarded. In order not to introduce a bias this cut is applied both to the data samples and to the simulation samples.

5.3.4 Quality of reconstructed objects

The purpose of the requirements described in this subsection is to select events that have a reconstructed electron–like object. This object consists of a cluster in the electromagnetic calorimeter and a track in the Inner Detector that is geometrically matched to the cluster.

Track to cluster matching

A track in the inner detector can be extrapolated to the liquid argon calorimeter and the η and φ coordinates of this extrapolation can be computed. In order for a track to be matched to a cluster the following two conditions are imposed

- $|\varphi_{Track} - \varphi_{Cluster}| < 0.05$ rad,

- $|\eta_{Track} - \eta_{Cluster}| < 0.01$.

For each event all possible track–cluster combinations are tested whether the track matches to the cluster or not. The event is accepted for the analysis if there is at least one matched track-cluster combination.

Track quality

At least 2 hits in the pixel detector for the matched track are required. This requirement ensures an acceptable track quality.

5.4 Event weighting

This section discusses two weighting schemes that are applied for the CTB 2004. In general, a weighting scheme is a technique in statistical data analysis where a number, i.e. a weight, is assigned to each data item of the analysis. The weight reflects the relative importance of the corresponding data item. As a consequence, some data items are more emphasized than others. In the case of this analysis, a weight is assigned to each event. Since a combination of weighting schemes is employed, the total weight of an event is the product of the individual weights computed by all weighting schemes for the given event.

For some distributions, e.g. the impact profiles, there is a difference between the simulated Monte Carlo samples and the data samples. The purpose of the event weighing is to make these samples comparable. In order to achieve this, the events in the two samples are weighted in such a way that the differences between the simulated Monte Carlo samples and the data samples vanish for the distributions mentioned above.

A weighting scheme to describe the beam line acceptance is presented in subsection 5.4.1. The angular weighting procedure introduced in subsection 5.4.2 is used to match the impact profiles of the Monte Carlo simulation to data.

5.4.1 Beam line acceptance

Particles which loose a signficant amount of energy in the beam line will have a smaller probability to reach the trigger scintillators. Since the beam line was not modeled in the Monte Carlo simulation, a weighting scheme is employed to simulate the acceptance of the beam line. In the simulation a detector is placed directly after the far upstream material (see section 5.1 and subsection 5.6.1). For each event the ratio of the energy of the most energetic particle $\tilde{E}$ measured by this detector and the nominal beam energy, i.e. $\tilde{E}/E_{beam}^{nominal}$, is used to compute a weight from the weighting curve shown in figure 5.6. This weight is attributed all measurement variables of the event. The weighting curve has been obtained by a dedicated beam line simulation beforehand [22]. The application of the beam line acceptance weight has no significant impact on the calorimeter measurements, but is needed for a correct description of the tail of the momentum measurement in the inner detector (see figure 5.7).

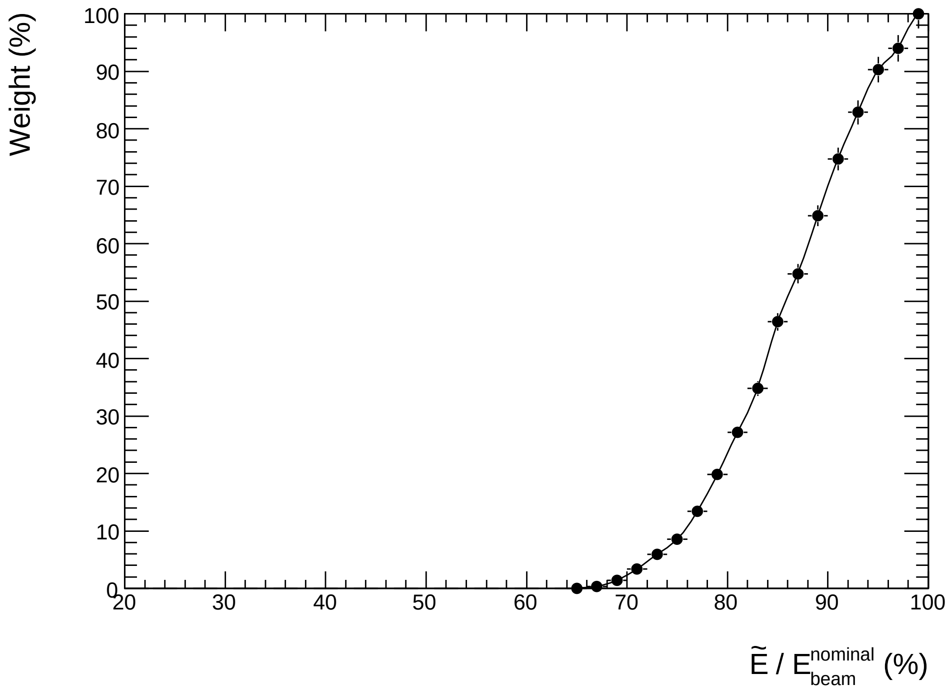

Figure 5.6: Beam line acceptance weight function.

5.4.2 Angular weighting

The beam profile is modeled in the Monte Carlo simulation to reflect the real beam profile. Since this is possible only to a certain extent an additional weighting scheme is introduced. For the data and the Monte Carlo sample for a given nominal beam momentum, the η and φ distributions of the clusters (see subsection 5.6.2) in the calorimeter are computed and binned into histograms. In order to obtain the best angular resolution possible, the strips layer cells are used for the computation of η and the middle layer cells for the computation of φ. For each bin in the η and φ histograms a weighting

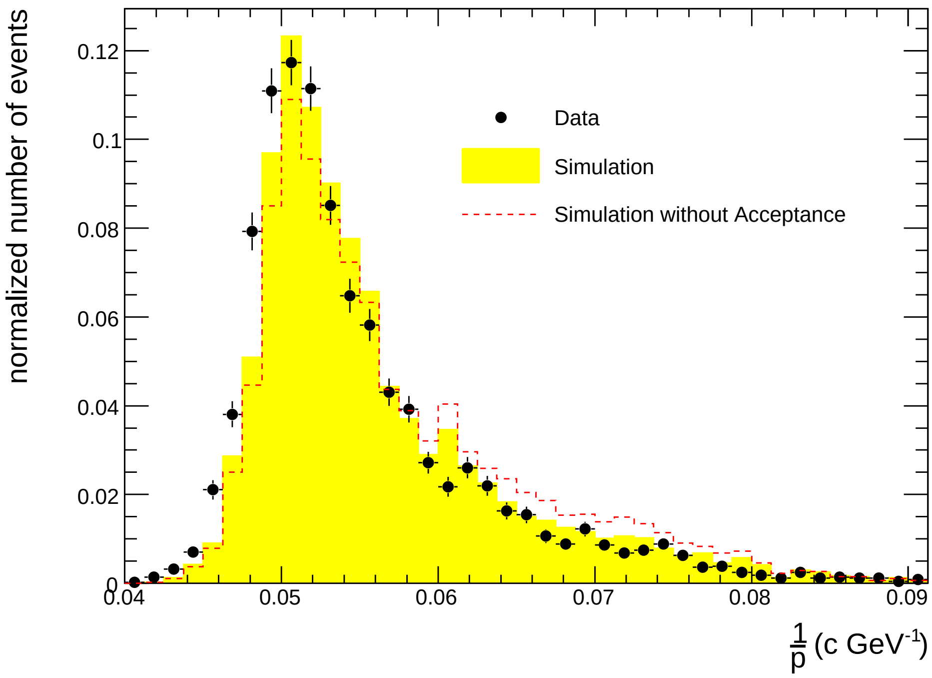

Figure 5.7: The ration of $1/p$ measured with the silicon detector (3 pixel layers and 4 SCT layers) for a beam momentum of p_{beam} =20 GeV/c. The solid circles are the data, the shaded area represents the simulation including the beam acceptance, the dashed line the simulation without the beam acceptance. The remaining discrepancy between the Monte Carlo simulation including the beam acceptance and the data comes from a slight misalignment of the Inner Detector.

factor is computed in the following way: If the bin content for the Monte Carlo sample is larger than for the data sample, this bin gets the ratio between data content and Monte Carlo simulation content (which is by definition smaller than 1) as weight for the Monte Carlo sample and 1 as weight for the data sample. If the bin content for the data sample is larger than for the Monte Carlo sample, it is done the other way round. This ensures that the distributions for the Monte Carlo and the data samples are equal after weighting and that all weights that are used are ≤ 1, therefore avoiding numerical instabilities.

For each event that is accepted for the analysis all measurement variables are weighted with these weighting distributions where the η and φ position of the cluster is used to determine the bins whose weights are used.

5.5 Energy measurement

The calibration of the energy measurement of the LAr calorimeter consists of two consecutive steps. First the raw signal (in ADC counts) for each cell is converted into the deposited energy in the cell. This step is denoted as *electronic calibration* and shortly discussed in subsection 5.5.1. During the second step clusters are formed out of calorimeter cells and an estimate of the initial energy of the impinging particle associated with the cluster is computed. The cluster formation algorithm is briefly described in subsection 5.5.2 and section 5.7 is devoted to a Monte Carlo simulation based procedure for computing the estimate for the initial energy of the particle.

5.5.1 Electronic calibration

A very detailed discussion of the electronic calibration and cell energy reconstruction for the LAr EMB calorimeter is given in [23].

The signals that are induced by the drifting ions in the liquid argon gaps of the calorimeter are amplified, shaped and then digitized at a sampling rate of 40 MHz in one of the three available gain channels. In the CTB 2004 setup six samples are digitized in contrast to ATLAS where five samples are digitized. From these six samples in the CTB 2004 five samples s_i closest to the signal peak are chosen and the signal amplitude ADC_{peak} is computed by the *Optimal Filtering Method* [24]

$$ADC_{peak} = \sum_{i=1}^{5} a_i \left(s_i - p\right) \tag{5.1}$$

where a_i are the optimal filtering coefficients that are computed from the predicted ionization pulses obtained using the technique described in [25] and p is the pedestal value which is the mean of the signal values generated by the electronic noise that is measured in dedicated calibration runs.

From the signal amplitude ADC_{peak} the cell energy E_{cell} is computed by

$$E_{\text{cell}} = F_{DAC\to\mu A} F_{\mu A\to\text{MeV}} \frac{1}{\frac{\text{M}^{Phys}}{\text{M}^{Cal}}} \sum_{i=1,2} R_i \left[\text{ADC}_{peak}\right]^i \tag{5.2}$$

where the factors R_i model the electronic gain with a second order polynomial, converting the ADC_{peak} amplitude into the equivalent current units (DAC). The factor $\frac{\text{M}^{Phys}}{\text{M}^{Cal}}$ takes the difference between the amplitudes of a calibration and an ionization signal of the same current for the electronic gain into account [25–28]. The constants $F_{DAC\rightarrow\mu A}$ and $F_{\mu A\rightarrow \mathrm{MeV}}$ finally transform the current (DAC) into energy (MeV). The details of the computation and validation of all the calibration constants used in equations 5.1 and 5.2 are described in [23].

The conversion factor $F_{\mu A\rightarrow \mathrm{MeV}}$ between the current measured by the LAr readout cells and the corresponding deposited energy[3] applied in the data reconstruction is taken from the 2002 liquid argon standalone test beam [29]. This conversion factor depends on the temperature of the liquid argon in the cells and during the 2002 liquid argon standalone test beam this temperature was not known with a precision of 0.1 K like at the Combined Test Beam 2004. The absolute energy scale of the LAr calorimeter was therefore extracted from CTB 2004 data. The scale factor is computed by comparing Monte Carlo simulation to data for runs with a nominal beam momentum of 180 GeV/c taken in different periods of the Combined Test Beam 2004. The computation yields a scale factor of 1.038±0.007. The error of 0.7% is composed of

- the uncertainty of the spectrometer current measurement for these runs, 0.04%,
- the uncertainty of the absolute scale of the beam momentum selection for $p_{beam} =$ 180 GeV/c, 0.52%,
- the response uniformity of the calorimeter, 0.4%.

5.5.2 Cluster building

In order to reduce the noise contribution to the energy measurement, a finite number of cells is used to calculate the energy. The process of choosing which cells are used is called *cluster building*. Several methods exist, e.g. topological clustering and sliding window clustering. Here a sliding window algorithm is used.

For building clusters of calorimeter cells that correspond to the impinging electron the standard ATLAS clustering [30] is used. For electrons, this means that a window of 3x7 middle cells (ηxφ extension) is slided across the calorimeter and the position with the highest energy content is used as seed position for the cluster. This seed is propagated to the other layers of the calorimeter. For each layer, cells contained in windows centered at the given seed for the layer are added to the cluster. The size of the window is different for the various layers.

[3] This factor contains an average sampling fraction, hence E_{cell} is a rough estimate of the energy deposited in this cell. In reality, the sampling fraction depends on the initial energy of the incident particle and will be corrected afterwards (see section 5.7).

5.6 Monte Carlo simulation and comparison to data

This section is devoted to the Monte Carlo simulation of the CTB 2004. After a description of the Monte Carlo simulation setup in subsection 5.6.1, the results of the Monte Carlo simulation are compared to data taken in the CTB 2004. This comparison is performed for the impact profile (subsection 5.6.2), the energy response for the different layers of the calorimeter (subsection 5.6.3) and the development of the electromagnetic shower (subsection 5.6.4). The Monte Carlo simulation to data comparison for the momentum measured by the Inner Detector is presented in subsection 5.6.5 because this measurement is one of the ingredients for the intercalibration procedure presented in chapter 6.

Since the calibration procedure (section 5.7) relies on Monte Carlo simulation a sufficiently good agreement between the Monte Carlo simulation and the data is necessary to achieve the required level of accuracy for the electron energy measurement. For the required linearity of 5‰ the agreement between the Monte Carlo simulation and the data for the sum of the visible energies of all cells in a cluster also has to be at the level of 5‰.

5.6.1 Monte Carlo simulation of the Combined Test Beam 2004

The response of the detector setup of the Combined Test Beam 2004 to the various beam particles is simulated using the `GEANT4` toolkit [31]. `GEANT4` uses Monte Carlo methods to simulate the physics processes when particles pass through matter. The `QGSP-EMV` physics list was used to parameterize these physics processes. The details of the geometric description of the Combined Test Beam 2004 in `GEANT4` are described in [32]. The simulated energy deposits are reconstructed with the same software as the data. This is all done inside the ATLAS offline software framework ATHENA, release 12.0.95.

The far upstream material (section 5.1) is taken into account with a piece of aluminum with the equivalent thickness of 15% of a radiation length placed directly downstream of the `GEANT4` particle generator. All particles that emerge from the far upstream material are recorded in the simulation and are used to model the effect of the beam line acceptance (subsection 5.4.1).

One effect that is not modeled in the simulation is the cross talk between strip and middle layers. This cross talk has been measured by analyzing the response of the various cells to calibration pulses [33, 34]. A Middle-to-Strips cross-talk of $X_{\mathrm{mi}\to\mathrm{st}} = 0.05\,\%$ and a $X_{\mathrm{st}\to\mathrm{mi}} = 0.15\,\%$ Strips-to-Middle cross-talk have been obtained (peak-to-peak values). They are accounted for after the energy reconstruction by redistributing $8 \cdot X_{\mathrm{mi}\to\mathrm{st}} \cdot E_{\mathrm{Middle}}$ from the middle layer energy[4] to the strip layer energy[5] and $X_{\mathrm{st}\to\mathrm{mi}} \cdot E_{\mathrm{Strips}}$ from the strip layer energy to the middle layer energy.

The simulated electron momentum that is used in the Monte Carlo simulation is the nominal beam momentum $p_{beam}^{nominal}$ for the given run (table 5.1). Since the average beam momentum $< p_{beam} >$ is not identical to the nominal beam momentum $p_{beam}^{nominal}$ all energies in the Monte Carlo simulation are scaled by $< p_{beam} > / p_{beam}^{nominal}$. This is justified because the nonlinearities of the detector response are negligible for such small scaling factors for the investigated beam momentum range.

5.6.2 Impact profile

The impact coordinates η and φ of a cluster are defined as the energy weighted η/φ values of all strip/middle layer cells belonging to the cluster (equation 5.3).

$$
\begin{aligned}
\eta &= \frac{\sum\limits_{i \in stripcells} \eta_i \, E_i}{\sum\limits_{i \in stripcells} E_i}, \\
\varphi &= \frac{\sum\limits_{i \in middlecells} \varphi_i \, E_i}{\sum\limits_{i \in middlecells} E_i},
\end{aligned}
\tag{5.3}
$$

where E_i, η_i and φ_i are the energy, η and φ values of a given cell.

The Monte Carlo simulation to data comparisons for η and φ are shown in figures 5.8 and 5.9 for all beam momenta.

Since the Monte Carlo simulation of the data is not good, the η and φ distributions from the Monte Carlo simulation as well as from the data were used as input for the angular weighting procedure described in subsection 5.4.2. The Monte Carlo simulation to data comparisons for η and φ after the angular and beam line acceptance (subsection 5.4.1) weighting are shown in figures 5.10 and 5.11 for all beam momenta. Due to the angular

[4] The sum of the energies of all cells of a given layer is denoted as its layer energy.
[5] Each middle cell has 8 adjacent strip cells.

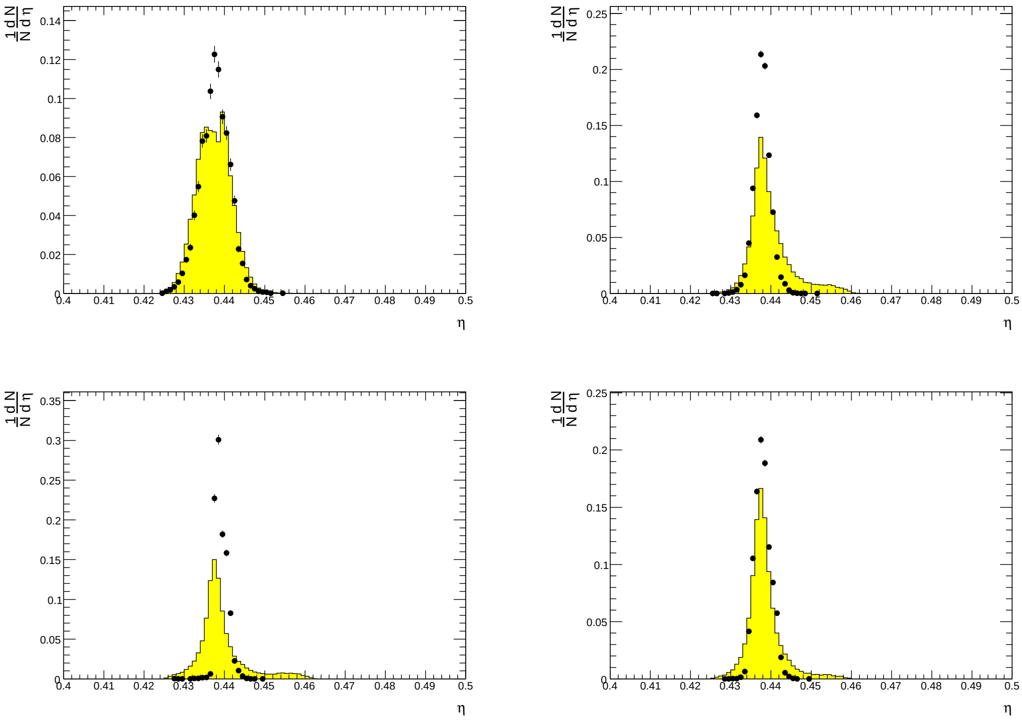

Figure 5.8: The η coordinate of the cluster for beam momenta of 20 GeV/c (left upper plot), 50 GeV/c (right upper plot), 80 GeV/c and 100 GeV/c before weighting. Shaded area: Monte Carlo simulation; dots: data.

weighting the residual differences between the Monte Carlo simulation distributions and the data distributions come from the beam line acceptance weighting procedure.

5.6.3 Energy response

The Monte Carlo simulation to data comparisons for all beam momenta for the reconstructed presampler layer energies E_{PS} are shown in figure 5.12, for the reconstructed strip layer energies E_{strips} in figure 5.13, for the reconstructed middle layer energies E_{Middle} in figure 5.14 and for the reconstructed back layer energies E_{Back} in figure 5.15. The agreement concerning the shapes of the distributions is sufficiently good in general.

The scale agreement can be assessed by the Monte Carlo simulation to data comparisons of the ratio of the means of the energy deposits for the various layers that are presented in figure 5.16 for all beam momenta. For the strip and the middle layers the scale agreement is at the level of 1% except for the middle layer at p_{beam}=20GeV/c where it is 1.5%. The scale agreement for the presampler and the back layer is at the level of

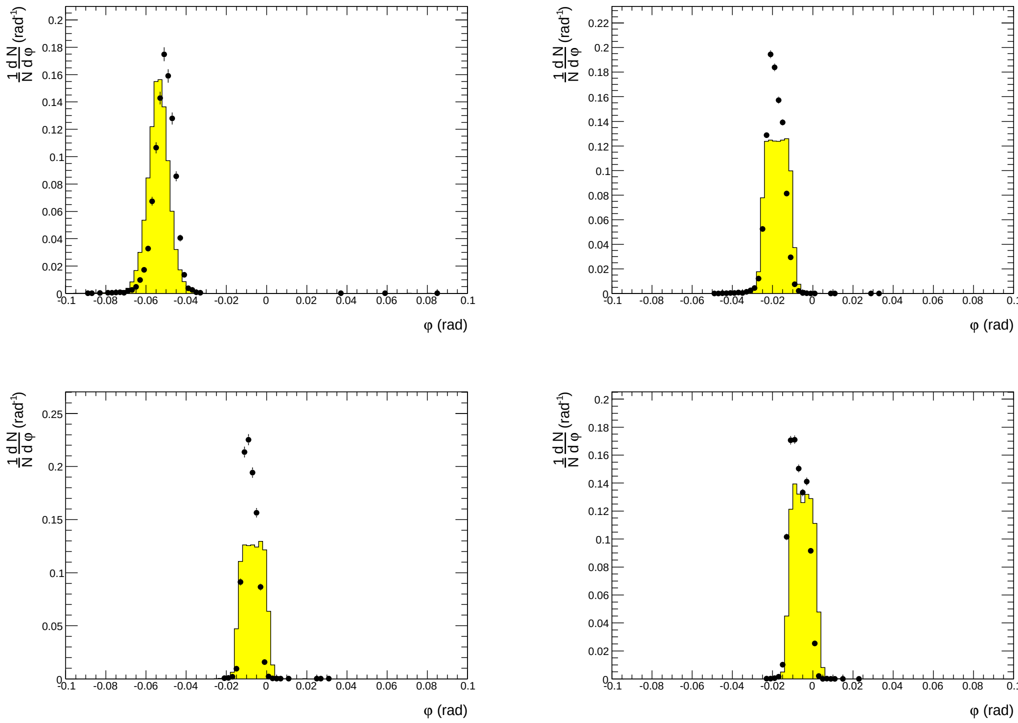

Figure 5.9: The φ coordinate of the cluster for beam momenta of 20 GeV/c (left upper plot), 50 GeV/c (right upper plot), 80 GeV/c and 100 GeV/c before weighting. Shaded area: Monte Carlo simulation; dots: data.

10%. However, since the reconstructed layer energies for these layers are typically 1-3% of the visible energy, the impact on the agreement of the visible energy is below 0.3%.

The Monte Carlo simulation to data comparisons of the visible energy E_{Vis} which is the sum of all layer energies is presented in figure 5.17 for all beam momenta. The shape agreement is best at p_{beam}=20GeV/c and deteriorates with increasing beam momentum. This is caused by tails towards lower energies that are larger in data than in the Monte Carlo simulation. The same behaviour has been found for runs of the CTB 2004 without magnetic field [14, 35]. The reason for this is that the beam line is not modeled in the Monte Carlo simulation.

The visible energy E_{Vis} distributions are fitted with Crystall Ball functions[6] and ratio of the peak $\mu_{E^{data}_{calib}}$ for the data and the peak $\mu_{E^{MC}_{calib}}$ for the Monte Carlo simulation is plotted in figure 5.18 for all beam momenta. The deviation of $\mu_{E^{data}_{calib}}/\mu_{E^{MC}_{calib}}$ from 1 is

[6]The definition of the Crystall Ball function is given in section 6.1.2, equation 6.6.

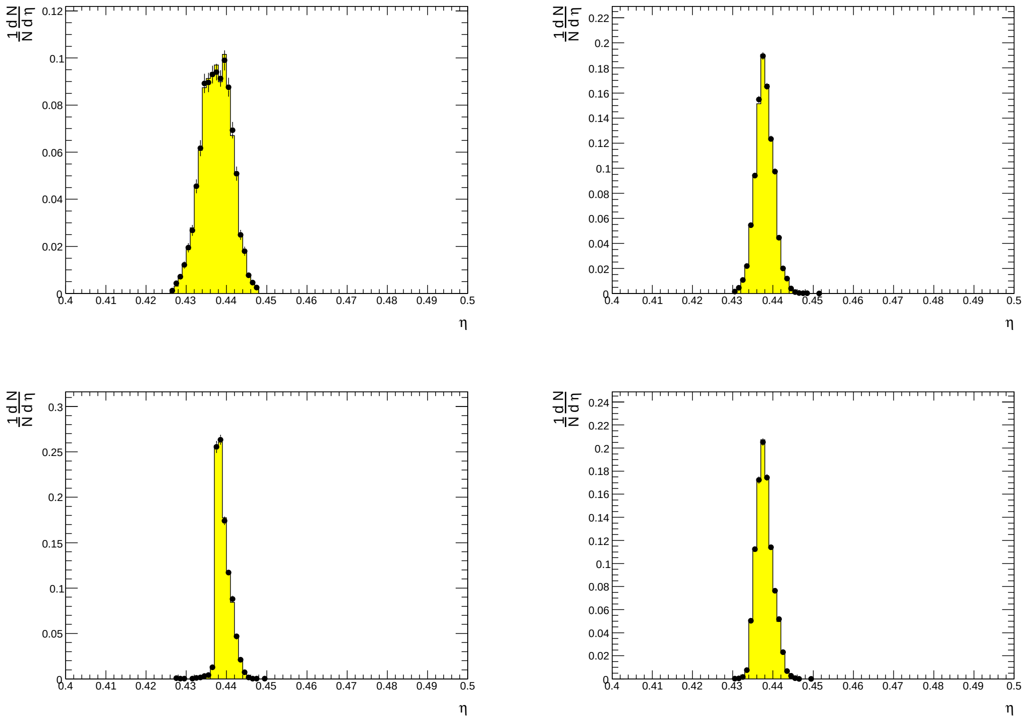

Figure 5.10: The η coordinate of the cluster for beam momenta of 20 GeV/c (left upper plot), 50 GeV/c (right upper plot), 80 GeV/c and 100 GeV/c after weighting. Shaded area: Monte Carlo simulation; dots: data.

within the energy scale uncertainty and the error bars. The main contributions to the errors bars are the beam momentum uncertainty (data only) and the statistical errors.

5.6.4 Shower development

Three quantities are investigated in order to compare the description of the shower development in the simulation with data. Concerning the lateral shower development for each event the energy profile in η direction in the strip layer is aligned with respect to the η position of the strip that received the highest energy deposit in this event. The strip layer is particularly well suited for this task due to its fine granularity $\Delta\eta_{strips}$ in η. The aligned distance in η is denoted $\bar{\eta}$, therefore $\bar{\eta}/\Delta\eta_{strips}$ is the number of strips that separates a given strip from the strip with the highest energy deposit in this event. For each strip its energy relative to the total strip layer energy is filled into an $\bar{\eta}/\Delta\eta_{strips}$ binned histogram. The histograms with the Monte Carlo simulation to data comparisons are shown in figure 5.19 for all beam momenta. The Monte Carlo simulation

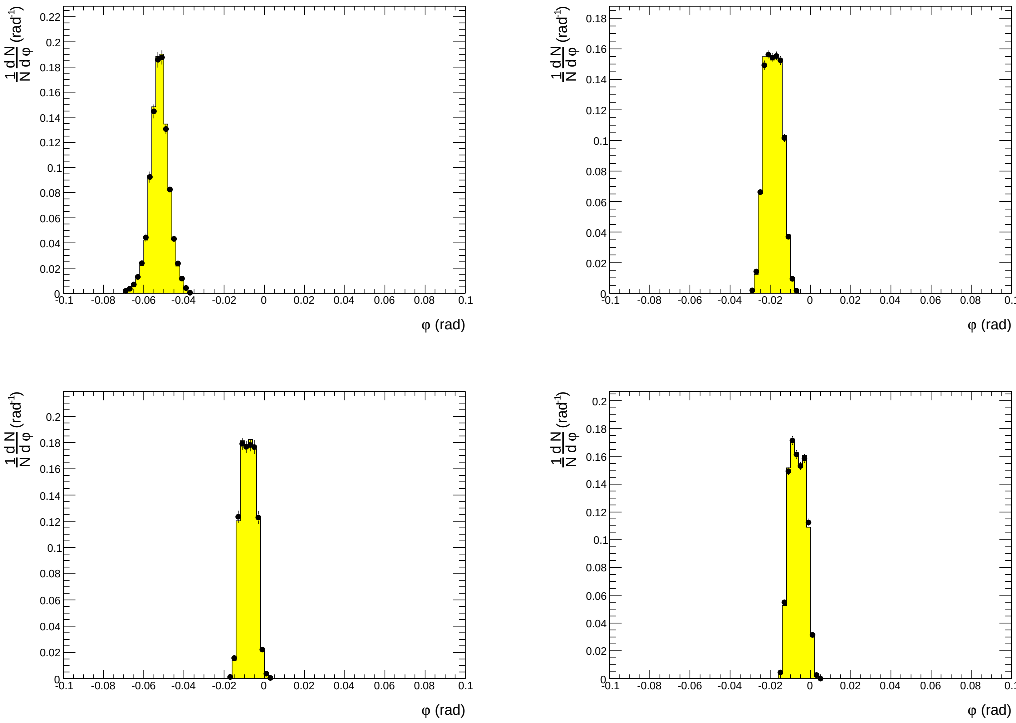

Figure 5.11: The φ coordinate of the cluster for beam momenta of 20 GeV/c (left upper plot), 50 GeV/c (right upper plot), 80 GeV/c and 100 GeV/c after weighting. Shaded area: Monte Carlo simulation; dots: data.

to data comparison for the Root Mean Square (RMS) of these histograms are presented in figure 5.20. The RMS is 6-11% larger in data than in the Monte Carlo simulation, i.e. the showers tend to be a bit narrower in the Monte Carlo simulation than in the data.

For the comparison of the longitudinal shower development two quantities are studied. Since in both quantities reconstructed energies appear in the nominator as well as in the denominator, they are independent of the global energy scale. The first quantity is the shower depth X_{mean} defined as the energy weighted average layer depth of all accordion layers by

$$X_{mean} = \frac{E_{Strips}\, X_{Strips} + E_{Middle}\, X_{Middle} + E_{Back}\, X_{Back}}{E_{Strips} + E_{Middle} + E_{Back}} \tag{5.4}$$

where $X_{Strips}, X_{Middle}, X_{Back}$ denote the average depth of the corresponding layer in units of radiation lengths (X_0) given in table 5.3. The Monte Carlo simulation to data comparisons are shown in figure 5.21 for all beam momenta. Again there is sufficiently good agreement, altough the simulated showers tend to get shorter with respect to the

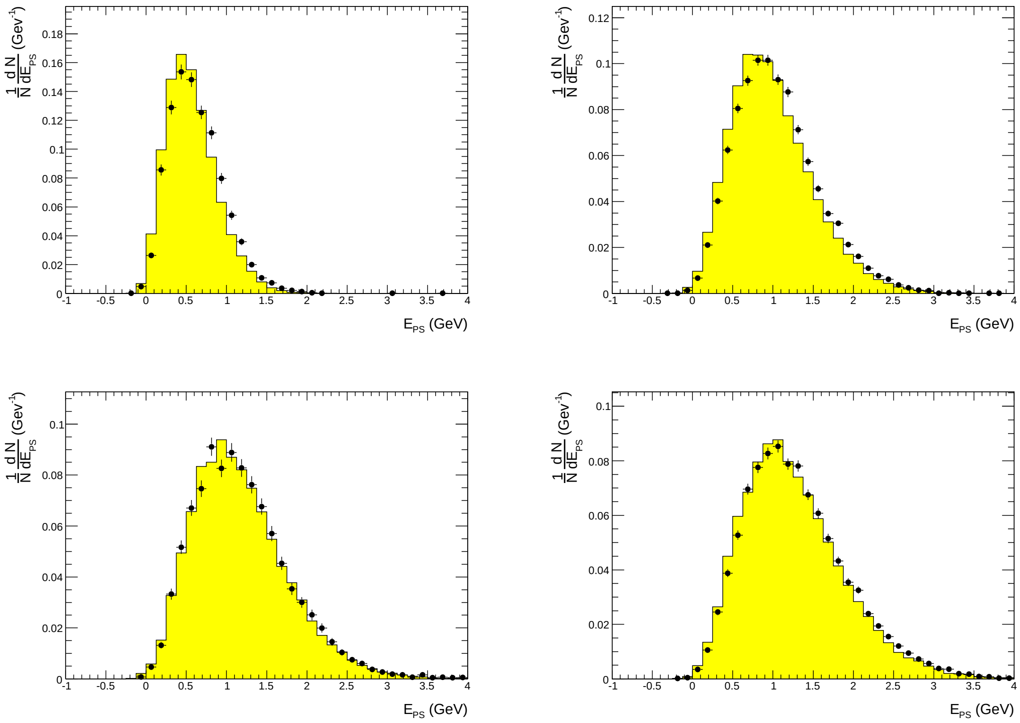

Figure 5.12: Energy deposit in the presampler for beam momenta of 20 GeV/c (left upper plot), 50 GeV/c (right upper plot), 80 GeV/c and 100 GeV/c. Shaded area: Monte Carlo simulation; dots: data.

data with increasing beam momentum.

Layer	X_{layer}^{start} (X_0)	X_{layer}^{stop} (X_0)	X_{layer} (X_0)
Presampler	1.50	1.78	1.64
Strips	2.18	6.41	4.29
Middle	6.41	25.02	15.71
Back	25.02	26.78	25.90

Table 5.3: LAr EMB layer boundaries and average depth at the beam impact point $(\eta = 0.442, \varphi = 0)$.

The second quantity for the longitudinal shower development is the ratio E_{strips}/E_{middle} of the energies of the strip and middle layers. This ratio is very sensitive to the amount of material in front of the calorimeter. Therefore it can be used to assess the level of accurateness of the material description in the simulation. The Monte Carlo simulation to data comparisons are shown in figure 5.22 for all beam momenta. The shape agreement is quite good, but on average E_{strips}/E_{middle} decreases more strongly with increasing

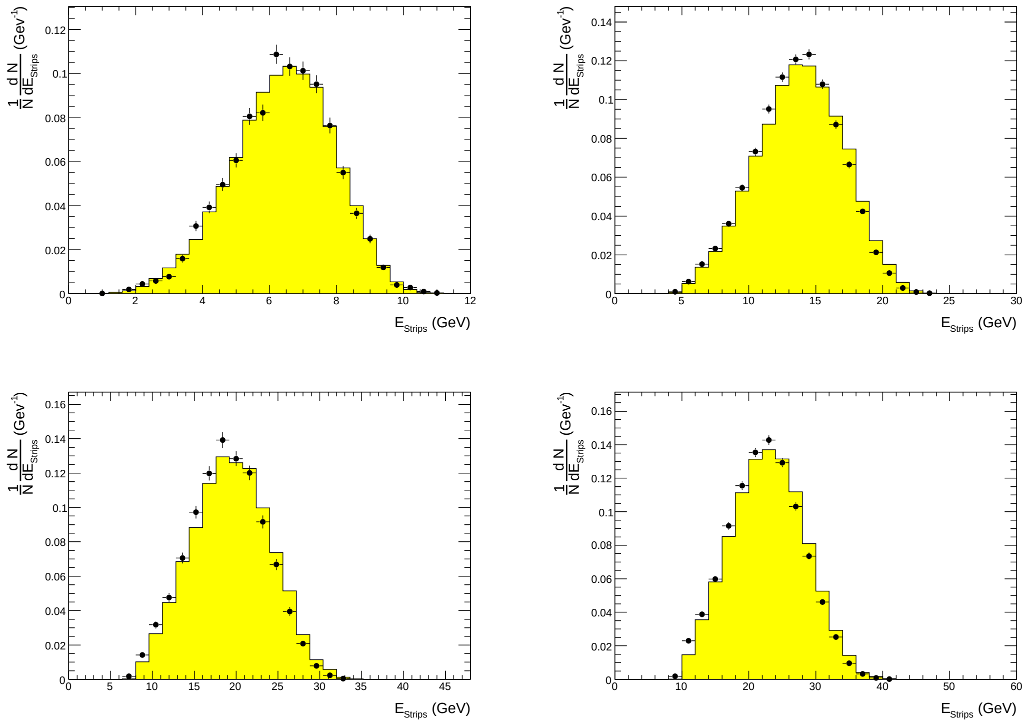

Figure 5.13: Energy deposit in the strip layer for beam momenta of 20 GeV/c (left upper plot), 50 GeV/c (right upper plot), 80 GeV/c and 100 GeV/c. Shaded area: Monte Carlo simulation; dots: data.

beam momentum in the data than in the Monte Carlo simulation . This implies that the showers start earlier in the Monte Carlo simulation than in data confirming the interpretation of the shower depth distributions in figure 5.21.

5.6.5 Momentum Analysis

The ratio p_{beam}/p of the beam momentum and the momentum measured by the Inner Detector is shown in figure 5.23 for all beam momenta and compared to Monte Carlo simulation. The inverse momentum is plotted because this quantity is actually measured in the Inner Detector. The sagitta of the curved track is directly proportional to $1/p$ and without bremsstrahlung and multiple scattering events is distributed like a Gaussian.

The agreement of the description of the tails of the distribution is sufficiently good, but the scale agreement is not better than a few percent because of residual misalignment between the various Inner Detector components that could not be resolved [36].

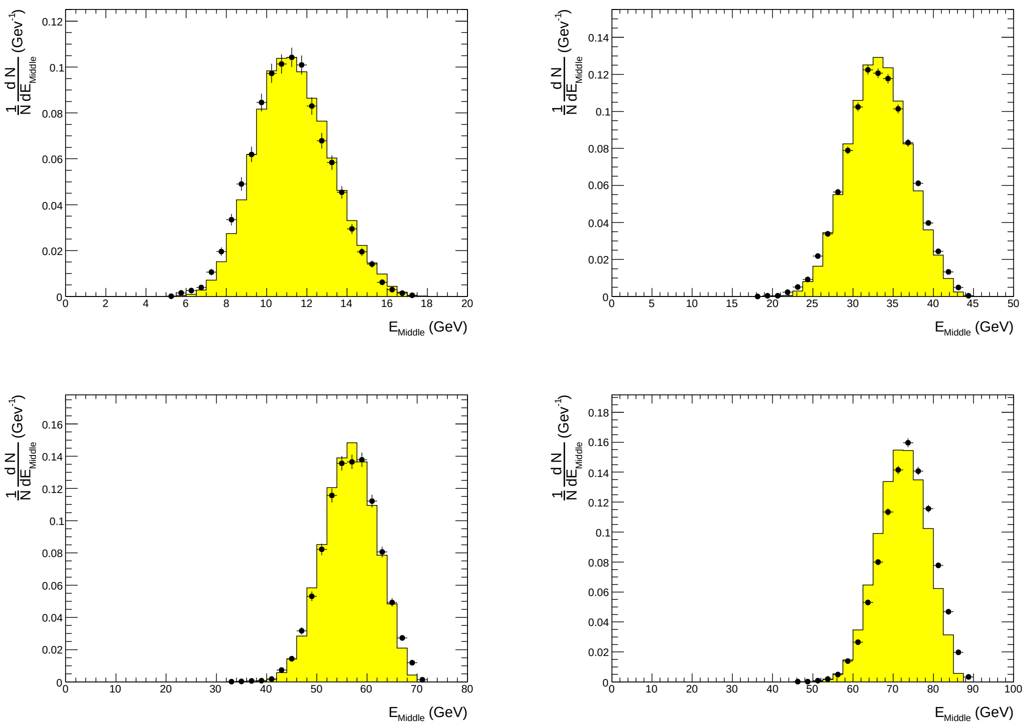

Figure 5.14: Energy deposit in the middle layer for beam momenta of 20 GeV/c (left upper plot), 50 GeV/c (right upper plot), 80 GeV/c and 100 GeV/c. Shaded area: Monte Carlo simulation; dots: data.

5.6.6 Systematic Uncertainties

The level of accuracy of the Monte Carlo simulation description of the electromagnetic shower development in the LAr calorimeter is affected by uncertainties associated with the geometrical set-up and detector description (thickness of the lead absorbers, the depth of the first layer, the exact amount of material in front of the strip compartment, cables, electronics, the thickness of the cryostat and the amount of LAr in front of the presampler). Similar uncertainties will be an issue for ATLAS taking data from LHC collisions. Therefore, it is important to investigate them in the controlled test-beam environment. However, the uncertainties associated with the description of the combined test beam set-up itself will not be present in ATLAS. In order to understand the true systematic effects relevant to ATLAS, the combined test beam set-up-related uncertainties must be understood and a procedure developed to isolate them.

The dominant contributions of the total systematic uncertainty are

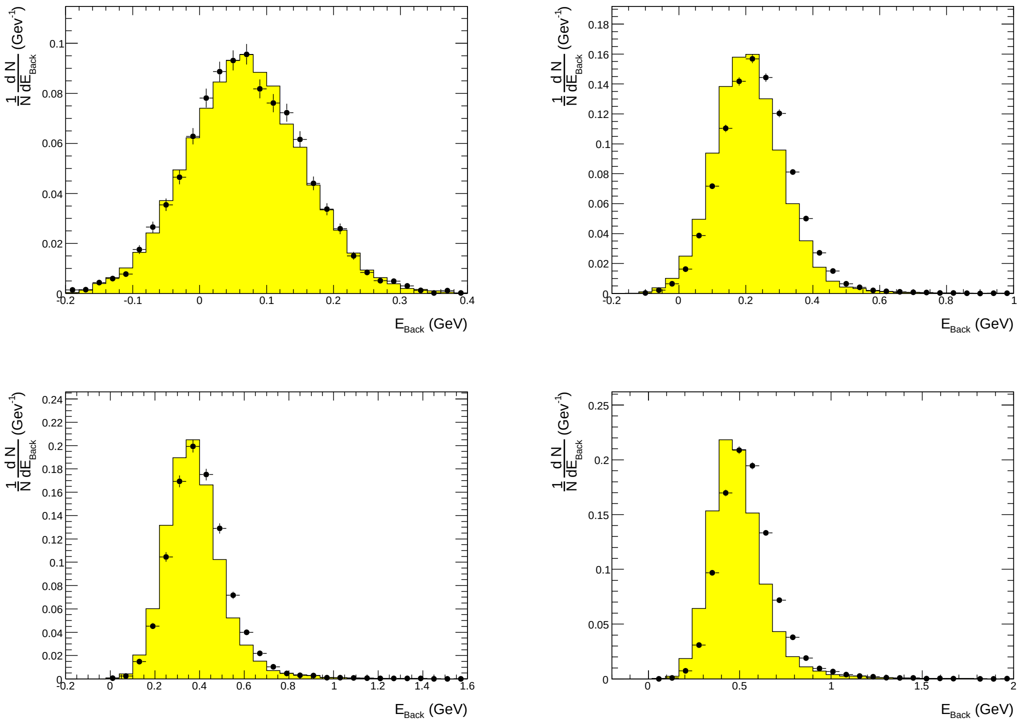

Figure 5.15: Energy deposit in the back layer for beam momenta of 20 GeV/c (left upper plot), 50 GeV/c (right upper plot), 80 GeV/c and 100 GeV/c. Shaded area: Monte Carlo simulation; dots: data.

- Uncertainties in the knowledge of the beam momentum. Although the absolute beam momentum may include large errors, the relative momentum shifts between different nominal beam momenta are considerably smaller and depend on changes in beam conditions (collimator apertures, magnet currents, etc). Their total contribution is generally relatively small at the level of 0.1 % (0.2 % for a beam momentum of 20 GeV/c and below) [14].

- Simulation uncertainties in the description of the electromagnetic shower development by the simulation. Comparisons between `GEANT4.8` (with multiple scattering) and `GEANT4.7` (without multiple scattering) showed small differences at the level of 1 % in the lateral and longitudinal shower development.

- Uncertainties in the Monte Carlo simulation description of the beam line and the description of the cryostat and the calorimeter. The impact of these contributions on the uncertainty of the reconstructed energy is smaller than 0.4 %. However, in terms of linearity, the listed effects have a much larger impact at lower energies

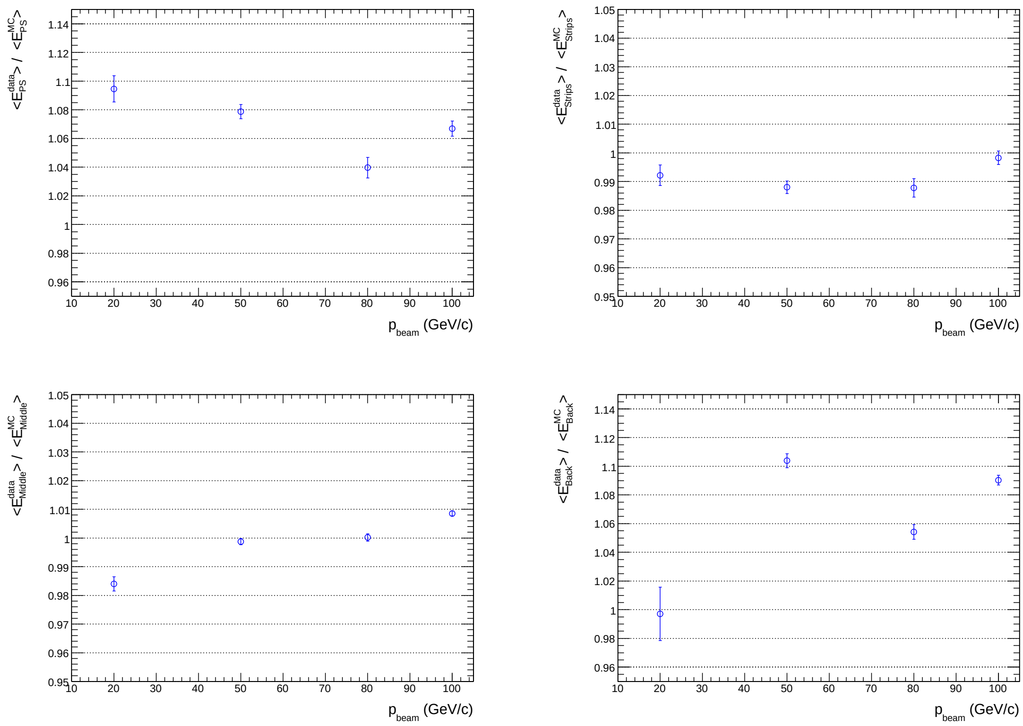

Figure 5.16: Monte Carlo simulation to data comparison for the mean of the energy deposit for the presampler (left upper plot), strips (right upper plot), middle (left lower plot) and back (right lower plot) layer energies.

than at higher energies; their impact on the linearity for energies $> 20\,\mathrm{GeV}$ is estimated to be less than $0.1\,\%$. These uncertainties – except uncertainties of the beam-line description – will also be present for ATLAS and are therefore listed below. Most of them come from the limited precision of the measurement of some parameters like the beam-line geometry, detector geometry, cross-talk, etc.

- Cross-talk in the strip compartment
- $\frac{\mathrm{M}^{Phys}}{\mathrm{M}^{Cal}}$ in the strip compartment (see subsection 5.5.1)
- Cross-talk between the strip and middle compartments
- Depth of the strip section compartment)
- Lead absorber thickness
- Monte Carlo simulation description of the presampler response
- Upstream material in the beam line
- Material in front of the presampler

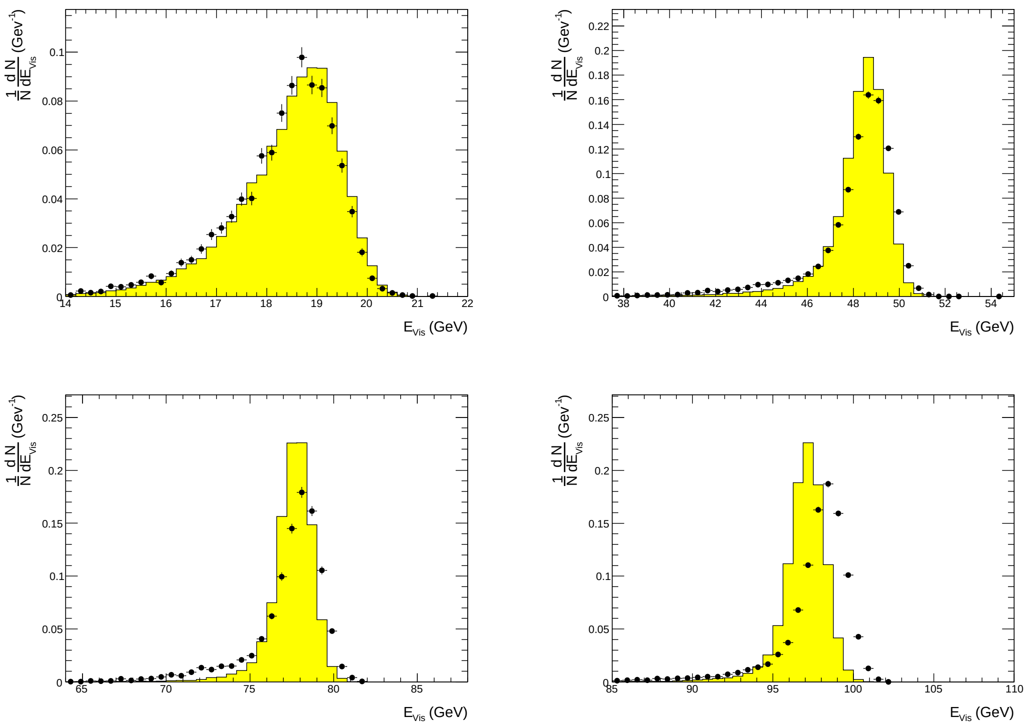

Figure 5.17: Visible energy for beam momenta of 20 GeV/c (left upper plot), 50 GeV/c (right upper plot), 80 GeV/c and 100 GeV/c. Shaded area: Monte Carlo simulation; dots: data.

- Dead material between the presampler and the strip compartment
- Simulation of charge collection
- Monte Carlo simulation description of lateral and longitudinal shower shape

The dominant contributions of the total systematic uncertainty are quantified in table 5.4. A detailed description of the systematic uncertainties can be found in [14].

5.7 The Calibration Hits Method

In the LAr EMB calorimeter only energy deposits inside the active material of the calorimeter are measured. This implies that certain energy deposits are not measured directly. These are

1. **Energy deposited outside the electromagnetic calorimeter:** In the Monte Carlo simulation this energy is split into 3 contributions:

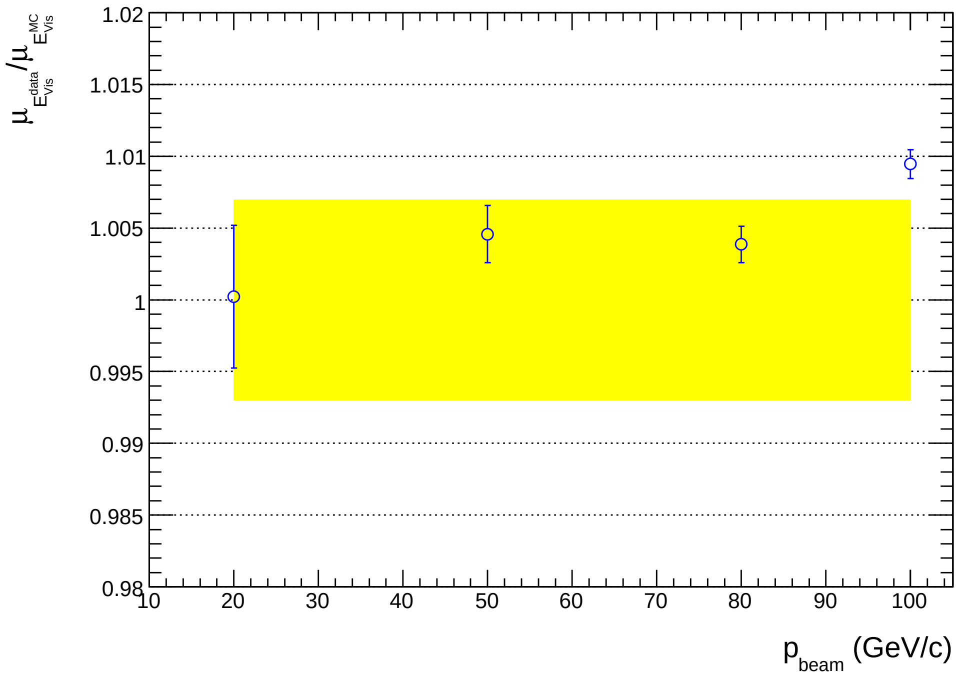

Figure 5.18: Ratio of the peak $\mu_{E^{data}_{calib}}$ of the visible energy E_{Vis} for the data and the peak $\mu_{E^{MC}_{calib}}$ of the visible energy E_{Vis} for the Monte Carlo simulation for all beam momenta. The yellow band representes the energy scale uncertainty for the data.

Error	Magnitude of effect	Uncertainty	Effect on linearity from 9-250 GeV
Cross-talk in strip layer	6 %	0.5 %	0.1 %
M_{phys}/M_{cali} in strip layer		1 %	$<$ 0.1 %
Cross-talk between strip and middle layer	$<$ 1 %	0.1 %	$<$ 0.1 %
Strip-middle layer boundary	-	1 mm	0.0
Lead thickness	-	1 %	$<$ 0.1 %
PS response	-	5 %	$<$ 0.1 %
Material in beam line	0.28 X_0	0.05 X_0	0.1 %
Material in front of PS	1.3 X_0	0.02 X_0	0.05 %
Material between PS-strip layer	0.75 X_0	0.02 X_0	0.2 %
Charge collection simulation	8 %	2 %	0.1 %
EM shower shape modeling	-	1 %	$<$ 0.1 %
Total			$<$ 0.4 %

Table 5.4: Summary of the effects of systematic uncertainties of the detector description in the MC simulation on the electron energy linearity from 9-250 GeV.

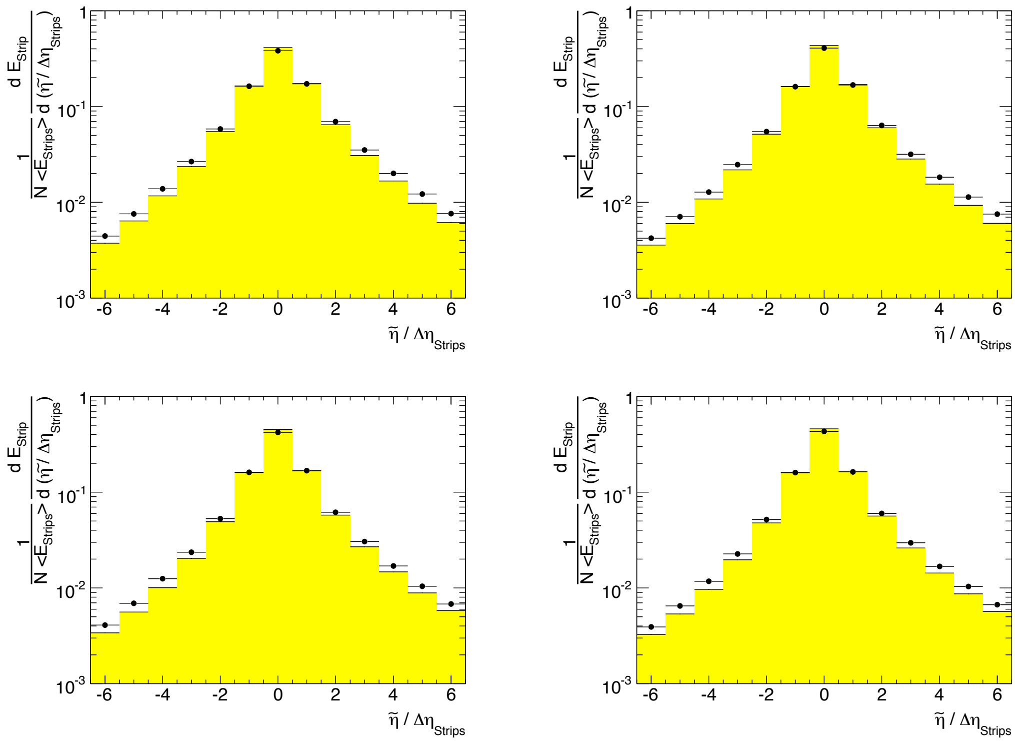

Figure 5.19: Lateral shower profile for beam momenta of 20 GeV/c (left upper plot), 50 GeV/c (right upper plot), 80 GeV/c and 100 GeV/c. Shaded area: Monte Carlo simulation; dots: data.

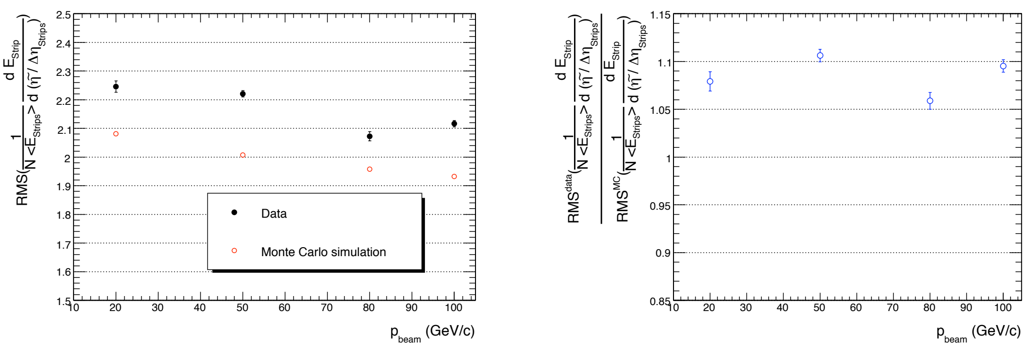

Figure 5.20: Root Mean Square (RMS) of the lateral shower profiles for all beam momenta (left). Monte Carlo simulation to data comparison for the Root Mean Square (RMS) of the lateral shower profiles (right).

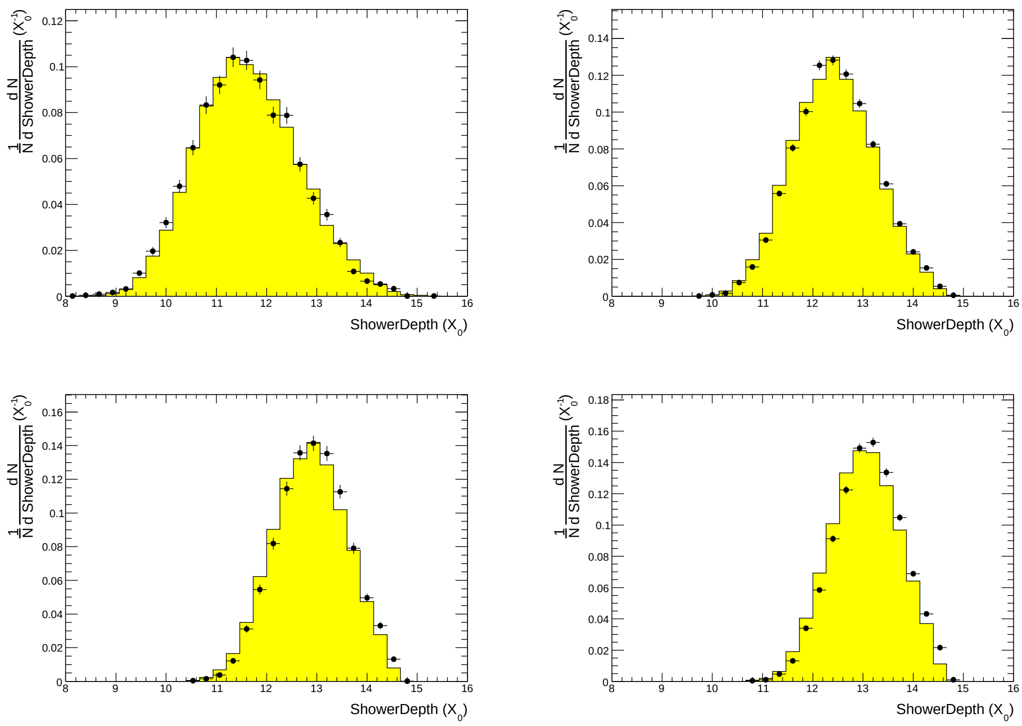

Figure 5.21: Longitudinal shower profile for beam momenta of 20 GeV/c (left upper plot), 50 GeV/c (right upper plot), 80 GeV/c and 100 GeV/c. Shaded area: Monte Carlo simulation; dots: data.

- $E^{true}_{upstreamPS}$ Energy deposited upstream of the presampler, see subsection 5.7.1.
- E^{true}_{PS-Acc} Energy deposited between the presampler and the accordion, see subsection 5.7.1.
- $E^{true}_{downstream}$ Energy deposited downstream of the accordion, see subsection 5.7.3.

2. **Energy deposited inside the electromagnetic calorimeter, but outside of the reconstructed cluster:** In order to minimize the noise contribution, clusters of finite size are used for the energy measurement. However, the energy deposits in the calorimeter cells outside the cluster are not taken directly into account and therefore have to be estimated, see subsection 5.7.2.

3. **Energy deposited inside the reconstructed cluster in the inactive material:** Because the LAr EMB calorimeter is a sampling calorimeter and the development and energy deposition of the electromagnetic cascade for an electron

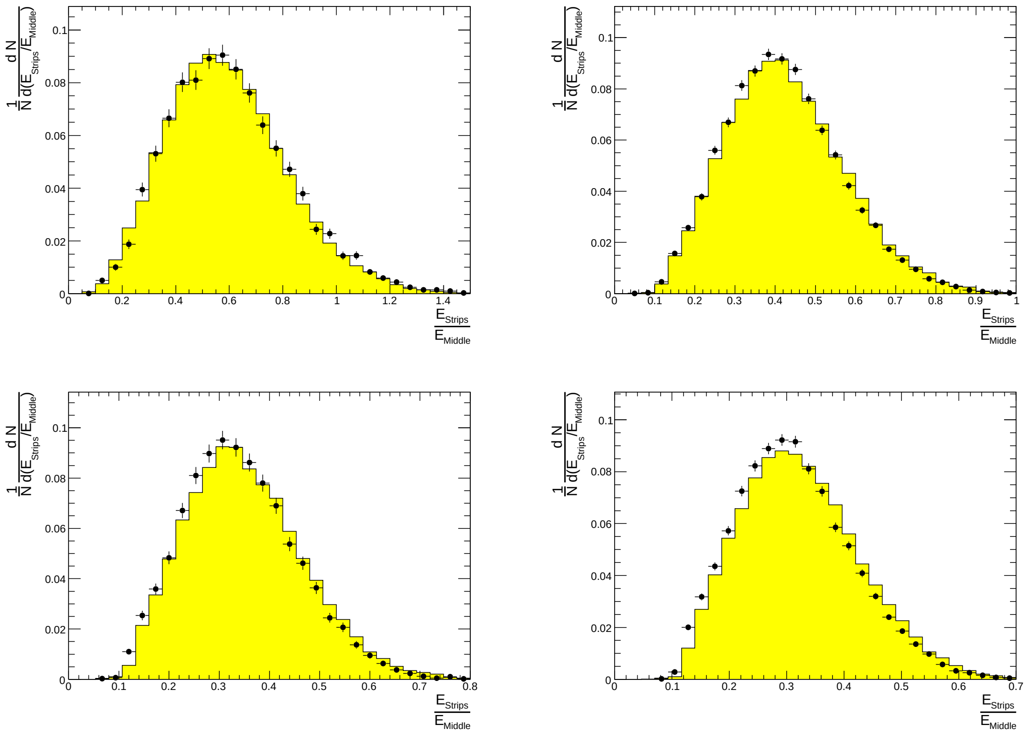

Figure 5.22: Ratio between the energy deposit in the strips layer and in the middle layer for beam momenta of 20 GeV/c (left upper plot), 50 GeV/c (right upper plot), 80 GeV/c and 100 GeV/c. Shaded area: Monte Carlo simulation; dots: data.

is a stochastic process, the ratio of the energy deposits in the active and passive material inside the cluster varies event by event and also as a function of the beam momentum. At 0^{th} order this ratio is approximated by a single factor which is already applied at the cell reconstruction level. Higher order corrections are presented in subsection 5.7.2.

These energy deposits are recorded as additional hits in the simulation, therefore the name *Calibration Hits Method*.

The idea of this calibration procedure is to estimate these different kinds of energy deposits by means of Monte Carlo simulations and correlate them to measurable quantities, namely the measured presampler energy E_{PS}, the measured accordion energy E_{Acc} which is the sum of the strips, middle and back layer energies,

$$E_{Acc} = E_{Strips} + E_{Middle} + E_{Back}, \tag{5.5}$$

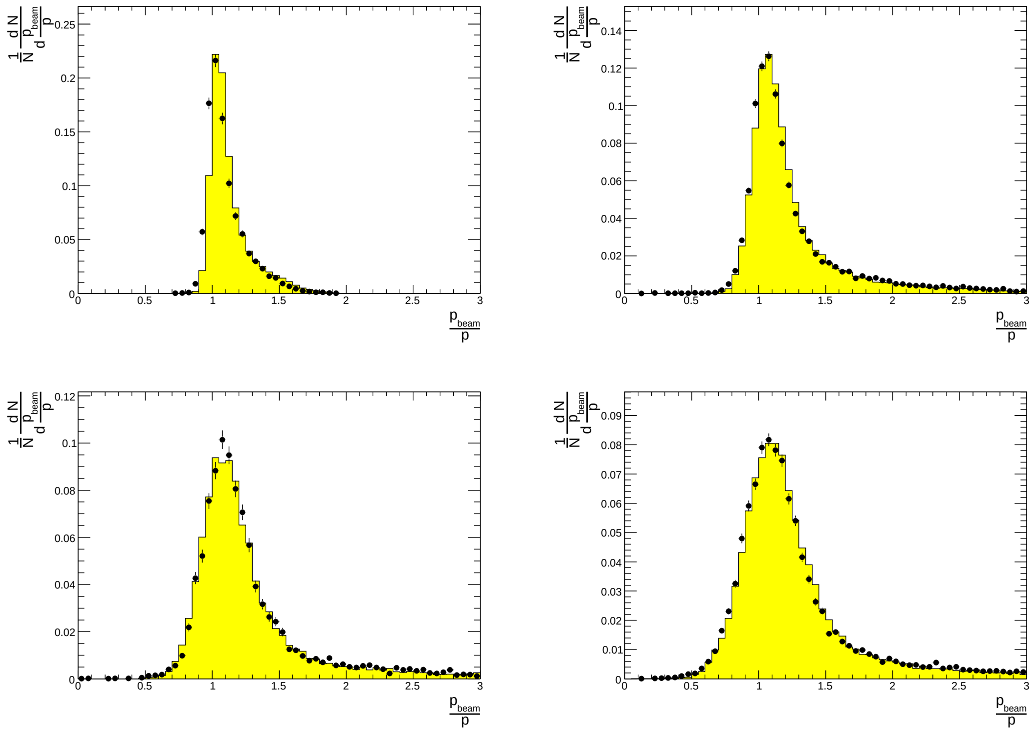

Figure 5.23: Ratio p_{beam}/p of the beam momentum and the momentum measured by the Inner Detector for beam momenta of 20 GeV/c (left upper plot), 50 GeV/c (right upper plot), 80 GeV/c and 100 GeV/c. Shaded area: Monte Carlo simulation; dots: data.

or the shower depth X_{mean}. Therefore quantities for the different energy deposits are defined for each event. These quantites are binned wrt. the measurable quantity that is used to parameterize the energy deposits. For each bin a representative value is computed. Finally a fit to these extracted representative values is made in order to obtain the desired parameterization for the estimate.

General strategy for the computation of representative values for distributions

For the distribution of a random variable there are various ways to extract a characteristic number representing the average value of the random variable. The most obvious choices are the mean, the median or the most probable value, also denoted as the peak position, of the distribution. For an asymmetric distribution the values for these different choices can differ considerably. Most of the distributions in this section as well as the distribution of the variable to be calibrated with this method, the cluster energy, are fairly asymmetric in the presence of a magnetic field in the Inner Detector.

Over the last years a consensus has been established in the ATLAS Egamma group (the group responsible for the calibration of electrons and photons) that the calibration of the electron energy has to be performed with respect to the peak position of the calibrated cluster energy. The reason for this choice is to minimize the effect of event selection cuts for physics analyses. These cuts mostly affect events in the tails of the various distributions and the dependece of peak values on these tails is the smallest among the three possible strategies mentioned above. In order to be consistent, the peak position of a distribution is used to characterize its average value throughout this section. Some example distributions are shown in figure 5.24 in section 5.7.1.

5.7.1 Estimation of the energy deposited upstream of the accordion

The energy deposited upstream of the accordion consists of the energy deposited upstream of the presampler $E^{true}_{upstreamPS}$, the energy deposited in the presampler E^{true}_{PS} and the energy deposited between the presampler and the accordion E^{true}_{PS-Acc}. For a given beam momentum the sum of these energies, denoted $E^{true}_{upstreamAcc}$ is estimated as a function of the measured presampler energy E_{PS}. For bins of E_{PS} covering the whole energy range of presampler energy measurements, the $E^{true}_{upstreamAcc}$ distributions are accumulated. The $E^{true}_{upstreamAcc}$ distributions are shown in figure 5.24 for p_{beam}=20GeV/c to demonstrate the asymmetry of the distributions.

For each bin a fit with a Gaussian is performed around the peak and the mean of the Gaussian $\bar{E}^{true}_{upstreamAcc}$ is attributed to the measured presampler energy corresponding to the center of the bin. The resulting profiles are plotted in figure 5.25 for all beam momenta.
For each beam momentum a line is fitted. The obtained offsets $\bar{a}(p_{beam})$ and slopes $\bar{b}(p_{beam})$ are shown in figure 5.26. For the runs at the Combined Test Beam 2004 without magnetic field in the Inner Detector the offsets $\bar{a}(p_{beam})$ are a monotonously rising function of p_{beam} [35]. With magnetic field in the Inner Detector, the tracks of the particles with lower momentum are bent more strongly resulting in a smaller impact angle. This leads to an increase of the lengths of the tracks in the cryostat and therfore to an increase of $\bar{a}(p_{beam})$. As a consequence, the obtained offsets $\bar{a}(p_{beam})$ are a nearly constant function of p_{beam} within the erros.

Next, the offset as a function of the beam momentum is parameterized by fitting

$$\hat{a}(p_{beam}) = a_0 + a_1 \log p_{beam}, \tag{5.6}$$

Figure 5.24: $E^{true}_{upstreamAcc}$ distributions for the various E_{PS} bins for p_{beam}=20GeV/c.

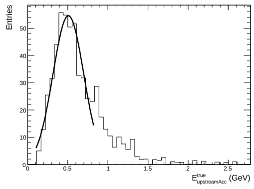

(a) 0.00GeV< E_{PS} <0.06GeV

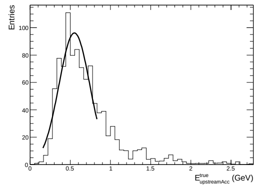

(b) 0.06GeV< E_{PS} <0.12GeV

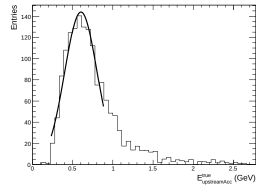

(c) 0.12GeV< E_{PS} <0.18GeV

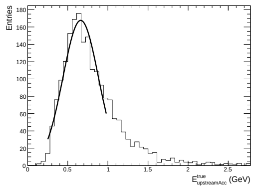

(d) 0.18GeV< E_{PS} <0.24GeV

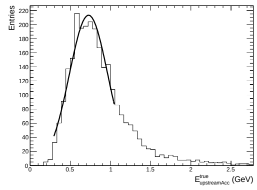

(e) 0.24GeV< E_{PS} <0.31GeV

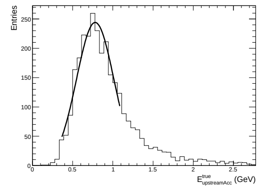

(f) 0.31GeV< E_{PS} <0.37GeV

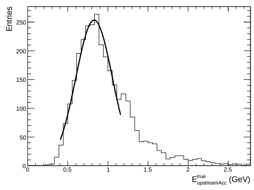

(g) 0.37GeV< E_{PS} <0.43GeV

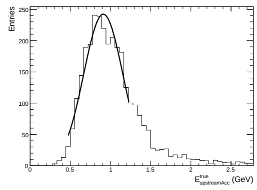

(h) 0.43GeV< E_{PS} <0.49GeV

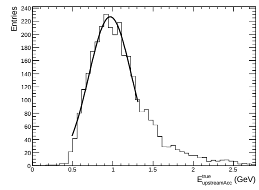

(i) 0.49GeV< E_{PS} <0.55GeV

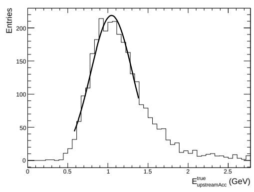

(j) 0.55GeV< E_{PS} <0.61GeV

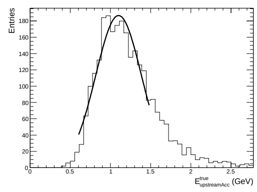

(k) 0.61GeV< E_{PS} <0.67GeV

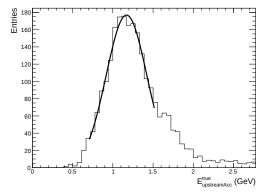

(l) 0.67GeV< E_{PS} <0.73GeV

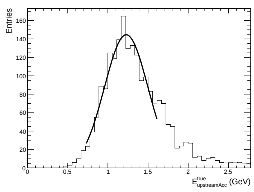

(m) 0.73GeV< E_{PS} <0.80GeV

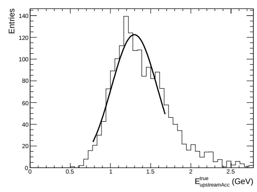

(n) 0.80GeV< E_{PS} <0.86GeV

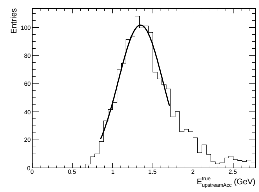

(o) 0.86GeV< E_{PS} <0.92GeV

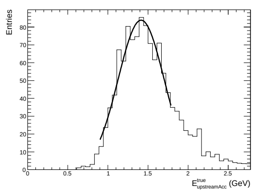

(p) 0.92GeV< E_{PS} <0.98GeV

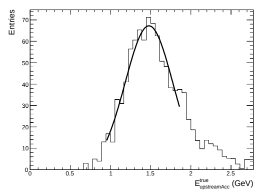

(q) 0.98GeV< E_{PS} <1.04GeV

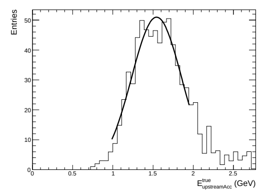

(r) 1.04GeV< E_{PS} <1.10GeV

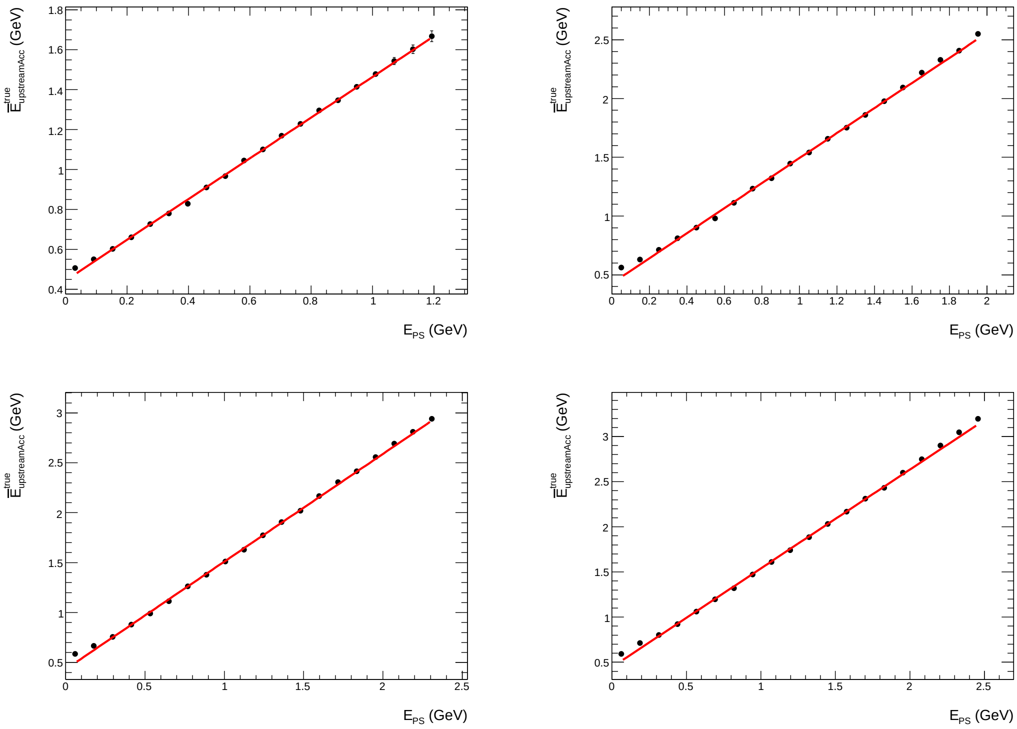

Figure 5.25: Energy deposited upstream of the accordion as a function of the recostructed presampler energy for beam momenta of 20 GeV/c (left upper plot), 50 GeV/c (right upper plot), 80 GeV/c and 100 GeV/c.

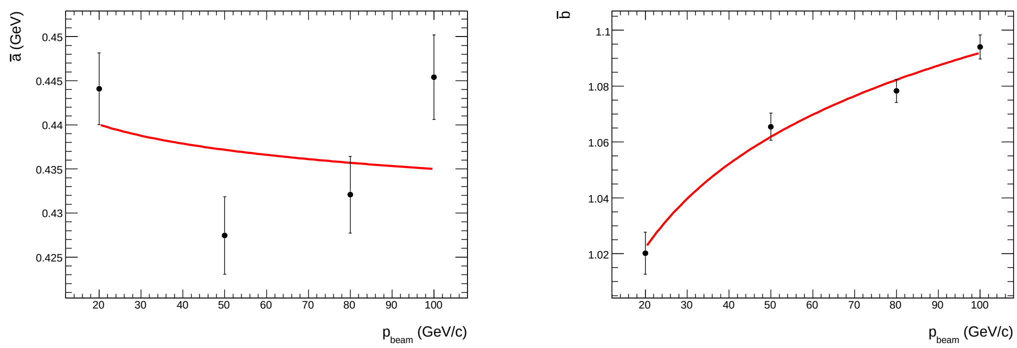

Figure 5.26: Offset (left) and slope (right) of the estimation of the energy deposited upstream of the accordion (equations 5.6 and 5.7).

and the slope by fitting

$$\hat{b}(p_{beam}) = b_0 + b_1 \log p_{beam}. \tag{5.7}$$

with p_{beam} in units of GeV c^{-1} for the logarithms. These are the same parameterizations that have also been used for the runs without magnetic field in the Inner Detector. The slope is very well parameterized and the differences for the offset are at the level of 20 MeV. The fitted values are $a_0 = 0.45(1)$ GeV, $a_1 = -0.003(3)$ GeV, $b_0 = 0.89(2)$ GeV and $b_1 = 0.43(5)$ GeV.

Then for a given event at a given beam momentum the energy deposited upstream of the accordion is estimated by

$$E^{estim}_{upstreamAcc}(E_{PS}, p_{beam}) = \hat{a}(p_{beam}) + \hat{b}(p_{beam})\, E_{PS}. \tag{5.8}$$

In order to determine the particle energy without prior knowledge of the beam momentum, an iterative procedure is applied, see subsection 5.7.4.

5.7.2 Estimation of the energy deposited in the accordion

The energy E^{true}_{Acc} deposited in the accordion can be estimated either as a function of the shower depth or as a function of the beam momentum.

For each event the ratio d of the energy deposited in the accordion and the measured accordion energy (equation 5.5) is defined by

$$d = \frac{E^{true}_{Acc}}{E_{Acc}}. \tag{5.9}$$

Beam momentum parameterization

For each beam momentum a Gaussian is fitted to the d distribution for the specific beam momentum and the mean of this Gaussian $\bar{d}(p_{beam})$ is extracted and plotted in figure 5.27. Then $\bar{d}(p_{beam})$ is approximated by fitting

$$\hat{d}(p_{beam}) = d_0 + d_1 \log p_{beam} + d_2 \log^2 p_{beam}. \tag{5.10}$$

with p_{beam} in units of GeV c^{-1} for the logarithms. The fitted values are $d_0 = 1.262516(15)$, $d_1 = 0.107626(8)$ and $d_2 = 0.011840(1)$.

For a given event at a given beam momentum the energy deposited in the accordion is

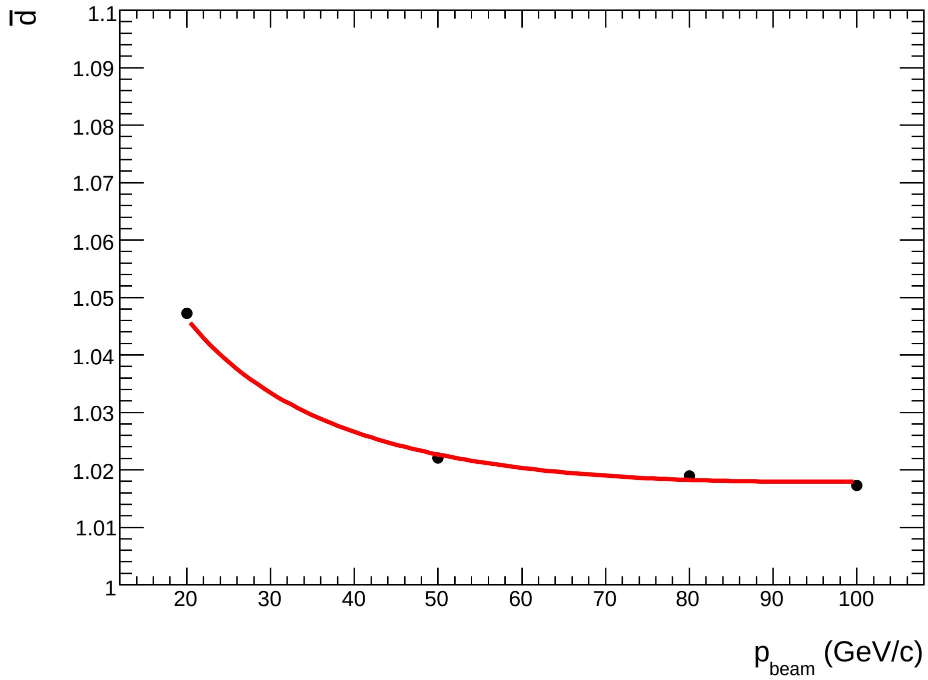

Figure 5.27: Mean $\bar{d}(p_{beam})$ of the Gaussian fitted to the d distribution (equation 5.9) for all beam momenta and its parameterization $\hat{d}(p_{beam})$.

estimated by

$$E_{Acc}^{estim}(E_{Acc}, p_{beam}) = \hat{d}(p_{beam})\, E_{Acc}. \tag{5.11}$$

In order to determine the particle energy without prior knowledge of the beam momentum, an iterative procedure is applied, see subsection 5.7.4.

Shower depth parameterization

The idea of this parameterization is to correct for sampling fraction fluctuations event by event by relating the sampling fraction to the shower depth. Analyses of CTB 2004 data have shown that this method works very well in the case without magnetic field [14].

For bins of the measured shower depth X_{mean} covering the whole shower depth range, the d distributions are accumulated. For each bin a fit with a Gaussian is performed and the mean of the Gaussian $\bar{d}(X_{mean})$ is attributed to the measured shower depth corresponding to the center of the bin. The resulting profiles for all beam momenta are plotted in figure 5.28.

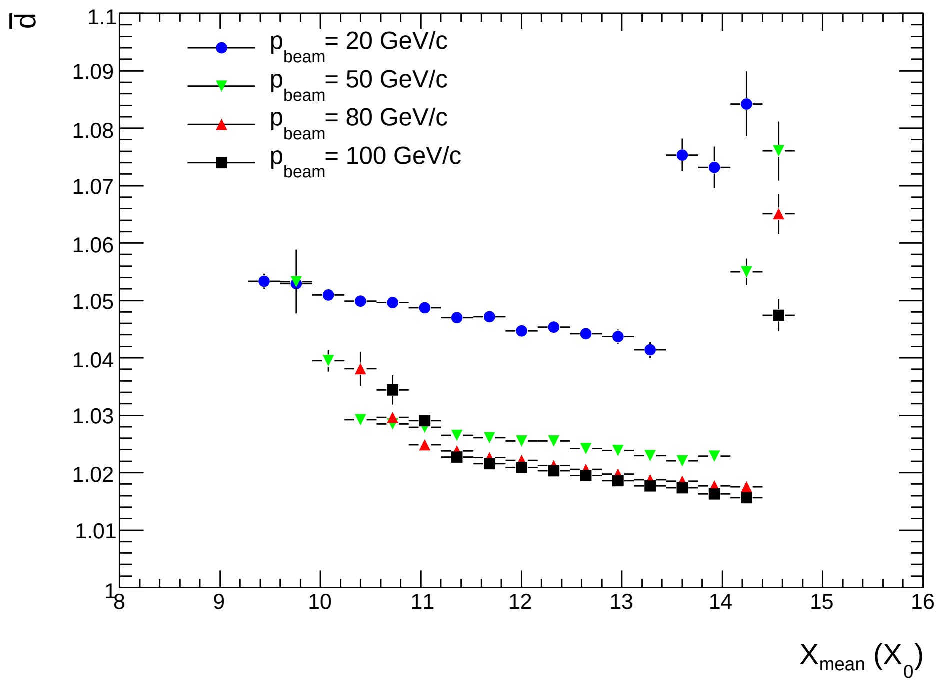

Figure 5.28: Mean $\bar{d}(p_{beam})$ of the Gaussian fitted to the d distribution (equation 5.9) as a function of the shower depth X_{mean} for all beam momenta.

Figure 5.28 demonstrates that the parameterization of $\bar{d}(X_{mean})$ as a function of the shower depth does not remove the dependence on the beam momentum. This is contrary to what has been found for the Combined Test Beam 2004 for runs without magnetic field in the Inner Detector [35]. The reason for this discrepancy is that in the presence of the magnetic field the energy deposited inside the electromagnetic calorimeter but outside of the reconstructed cluster relative to the energy of the particle depends on the beam momentum. In figure 5.29 the mean $\bar{d}_{5x11}(p_{beam})$ of the Gaussian fitted to the d distribution for clusters with a sliding window of 5x11 instead of 3x7 middle cells (subsection 5.5.2) is shown as a function of the shower depth X_{mean} for all beam momenta. These clusters are large enough to contain the whole shower in the calorimeter. The fact that the beam momentum dependence is not there for the 5x11 clusters indicates that the 3x7 cluster size together with the magnetic field generates the dependency of $\bar{d}(X_{mean})$ on the beam momentum. Therefore this parameterization is not used for the linearity and resolution measurements in section 5.8.

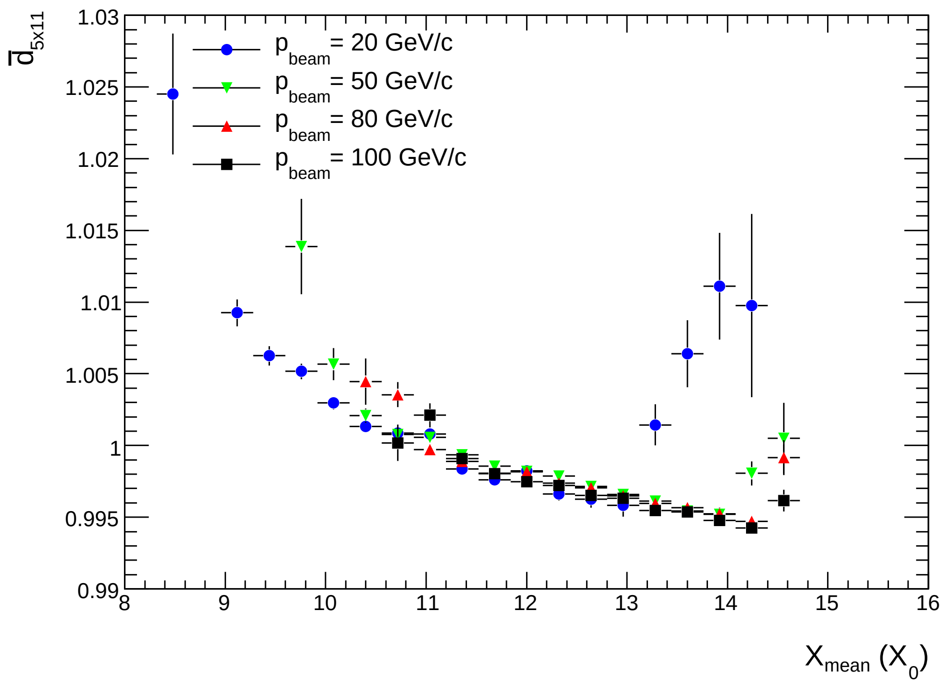

Figure 5.29: Mean $\bar{d}_{5x11}(p_{beam})$ of the Gaussian fitted to the d distribution (equation 5.9) for 5x11 clusters as a function of the shower depth X_{mean} for all beam momenta.

The same effect is also visible in ATLAS Monte Carlo simulation, although the effect there is so small that the shower shape parameterization is used by default for the electron energy calibration [37]. The reason why this effect is much smaller for the ATLAS detector is that the geometric layout of the CTB 2004 is very different from ATLAS including much larger distances between the inner detector components and the LAr EMB calorimeter.

5.7.3 Estimation of the energy deposited downstream of the accordion

The energy $E^{true}_{downstream}$ deposited downstream of the accordion can be estimated either as a function of the shower depth or as a function of the beam momentum.

Beam momentum parameterization

For each beam momentum a Gaussian is fitted to the $E^{true}_{downstream}$ distribution and the mean of the Gaussian $\bar{E}^{true}_{downstream}(p_{beam})$ is obtained and plotted in figure 5.30. Then $\bar{E}^{true}_{downstream}(p_{beam})$ is approximated by fitting

$$E^{estim}_{downstream}(p_{beam}) = l_0\, p_{beam} + l_1\, p^2_{beam}. \tag{5.12}$$

The fitted values are $l_0 = 9(4)\,10^{-4}\,\mathrm{c}$ and $l_1 = 2.3(7)\,10^{-6}\,\mathrm{c}^2\,\mathrm{GeV}^{-1}$.

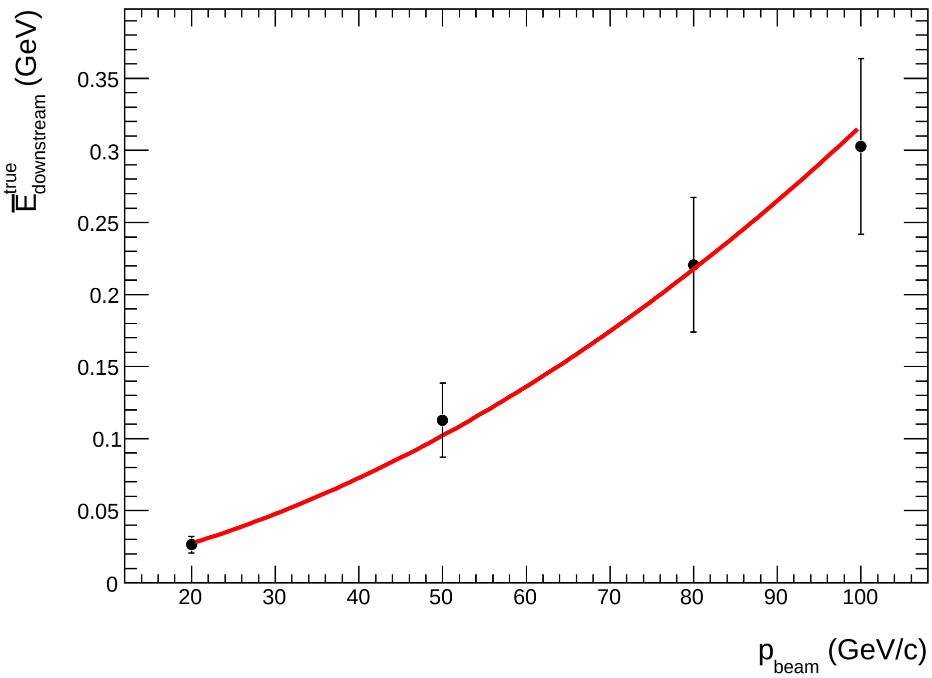

Figure 5.30: Mean of the energy deposited downstream of the accordion the all beam momenta and its parameterization $E^{estim}_{downstream}(p_{beam})$ (equation 5.12).

In order to determine the particle energy without prior knowledge of the beam momentum, an iterative procedure is applied, see subsection 5.7.4.

Shower depth parameterization

For each event the ratio of the energy deposited downstream of the accordion and the measured accordion energy which is the sum of the measured strips, middle and back layer energies is defined by

$$l = \frac{E^{true}_{downstream}}{E_{Acc}}. \tag{5.13}$$

For bins of the measured shower depth X_{mean} covering the whole shower depth range, the l distributions are accumulated. For each bin a fit with a Gaussian is performed and the mean of the Gaussian $\bar{l}(X_{mean})$ is attributed to the measured shower depth corresponding to the center of the bin. The resulting profiles for all beam momenta are plotted in figure 5.31.

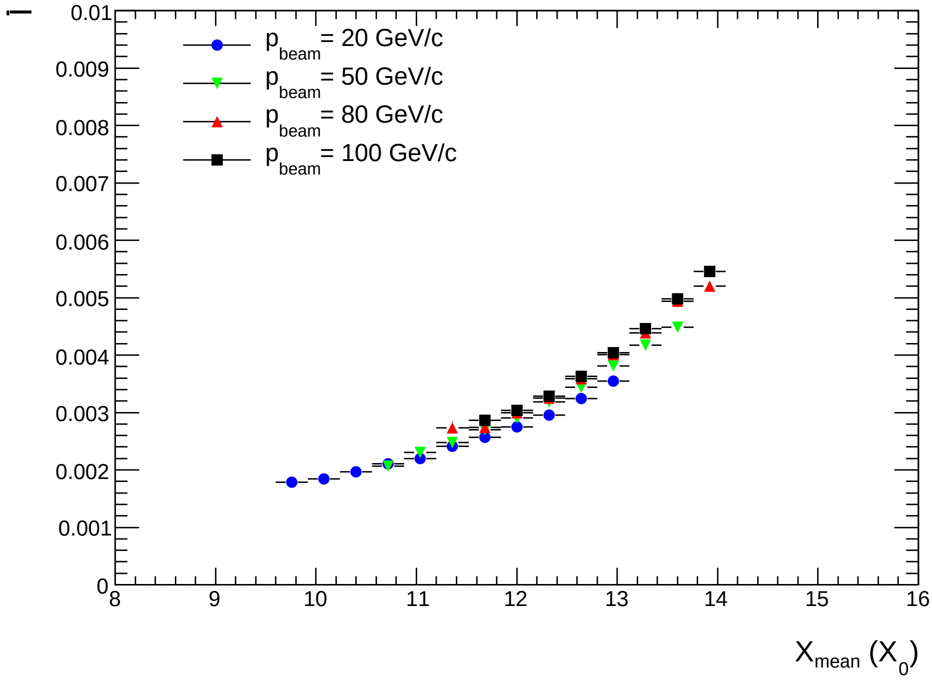

Figure 5.31: Mean $\bar{l}(p_{beam})$ of the Gaussian fitted to the l distribution (equation 5.13) as a function of the shower depth X_{mean} for all beam momenta.

Figure 5.31 shows that the parameterization of the ratio of energy deposited downstream of the accordion and the measured accordion energy does not completely remove the dependence on the beam momentum. The remaining differences are at the half permill level.

For the reasons shown in section 5.7.2, this parameterization is not used for the linearity and resolution measurements in section 5.8.

5.7.4 Iterative procedure

An iterative procedure is applied to compute the calibrated cluster energy. Starting value for the estimate for the calibrated cluster energy is the visible energy. In each iteration step the estimated calibrated cluster energy from the previous step together with

$$E^2 = p^2\, c^2 + m^2\, c^4 \tag{5.14}$$

is used to estimate the proper beam/particle momentum to select the new estimation coefficients. Here the knowledge that electrons have been selected from the beam is used to justify the neglection of the rest mass term contribution to the particle energy.[7] The selected estimation coefficients are then used to compute a new estimate for the calibrated cluster energy.

Beam momentum parameterization

$$\begin{aligned}
E^0_{Calib} &= E_{PS} + E_{Acc} \\
p^0 &= \frac{E^0_{Calib}}{c} \\
&\vdots \\
E^k_{Calib} &= E^{estim}_{upstreamAcc}(E_{PS}, p^{k-1}) + E^{estim}_{Acc}(E_{Acc}, p^{k-1}) + E^{estim}_{downstream}(p^{k-1}) \\
&= \hat{a}(p^{k-1}) + \hat{b}(p^{k-1})\, E_{PS} + \hat{d}(p^{k-1})\, E_{Acc} + E^{estim}_{downstream}(p^{k-1}) \quad k > 0 \\
p^k &= \frac{E^k_{Calib}}{c} \quad k > 0
\end{aligned} \tag{5.15}$$

where p^k is the k-th estimation of the particle momentum and E^k_{Calib} is the k-th estimation of the particle energy. $E^{estim}_{upstreamAcc}(E_{PS}, p^{k-1}) = \hat{a}(p^{k-1}) + \hat{b}(p^{k-1})\, E_{PS}$ is used to estimate the energy deposited upstream of the accordion and $E^{estim}_{Acc}(E_{Acc}, p^{k-1}) = \hat{d}(p^{k-1})\, E_{Acc}$ to estimate the energy deposited in the accordion.

This iteration procedure is executed until the relative difference between the two consecutive E_{Calib} values $|E^k_{Calib} - E^{k-1}_{Calib}|$ is smaller than 10^{-6}. On average 3 iterations are required to meet this termination condition.

[7] The rest mass of an electron is $m_e = 511$ keV/c. The investigated beam momenta are > 10 GeV.

5.8 Linearity and Resolution

The calibrated cluster energies are computed using the iteration scheme for the beam momentum parameterization (equation 5.15). The Monte Carlo simulation to data comparison is shown in figure 5.32 for all beam momenta. The shape agreement for calibrated cluster energy distributions is similar to the shape agreement for the visible energy distributions described in section 5.6.3. This means that the shape agreement is best at p_{beam}=20GeV/c and deteriorates with increasing beam momentum due to low energy tails larger in data than in the Monte Carlo simulation because the description of the beam line is not included in the Monte Carlo simulation and the beam line acceptance weighting (section 5.4.1) does only approximately describe the impact of the beam line.

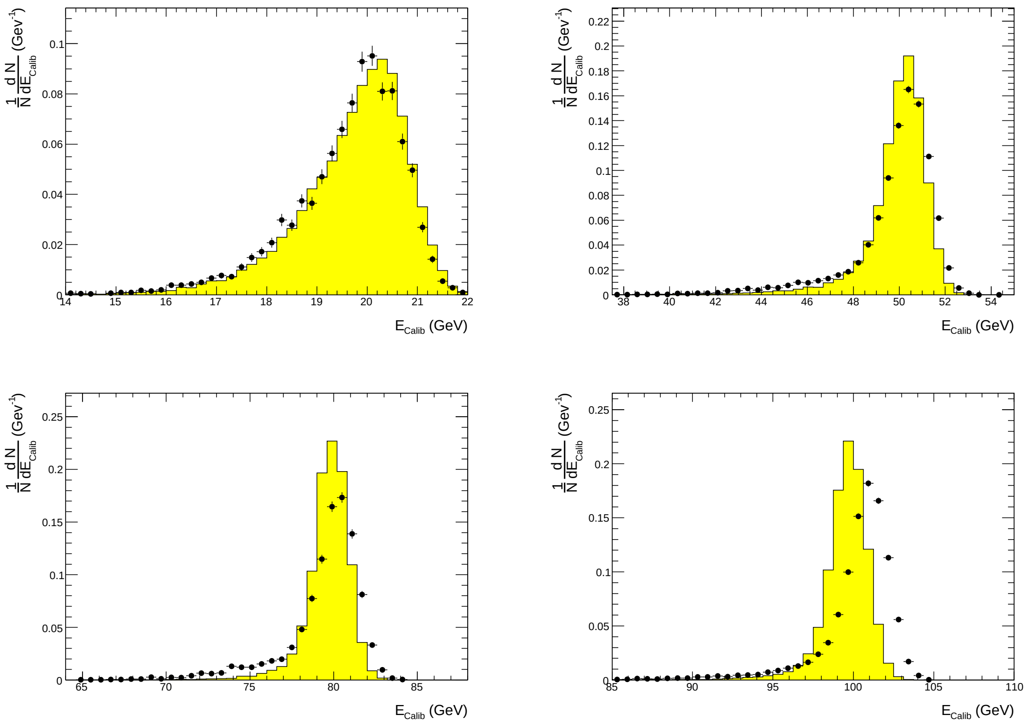

Figure 5.32: Calibrated energy for beam momenta of 20 GeV/c (left upper plot), 50 GeV/c (right upper plot), 80 GeV/c and 100 GeV/c. Shaded area: Monte Carlo simulation; dots: data.

The calibrated cluster energy distributions are fitted with Crystall Ball functions[8] and the mean $\mu_{E_{calib}}$ and the sigma $\sigma_{E_{Calib}}$ of these Crystall Ball functions divided by E_{beam} =

[8] The definition of the Crystall Ball function is given in section 6.1.2, equation 6.6.

$p_{beam} \cdot c$ are plotted in figures 5.33 and 5.34 to assess the linearity and resolution.

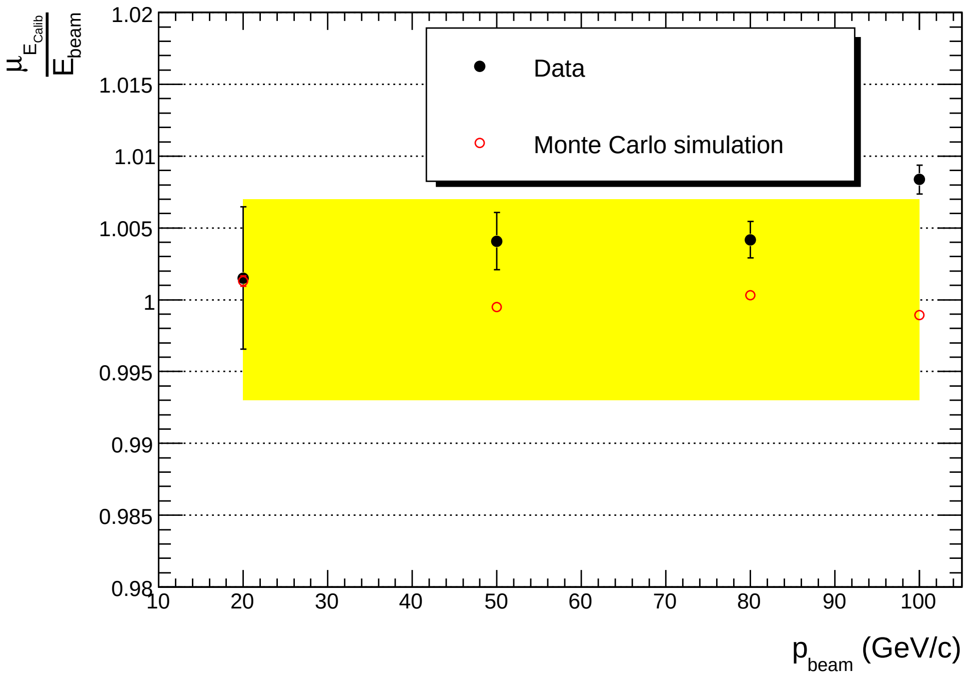

Figure 5.33: Linearity for Monte Carlo simulation and data. The yellow band representes the energy scale uncertainty for the data.

In figure 5.33 the deviation of $\mu_{E_{calib}}/E_{beam}$ from 1 is within the energy scale uncertainty and the error bars. The main contributions to the errors bars are the beam momentum uncertainty (data only) and the statistical errors. The root of the mean squared deviation of $\mu_{E_{calib}}/E_{beam}$ from 1 is 0.10% for the Monte Carlo simulation and 0.60% for the data. For the data this is within the energy scale uncertainty. Adjusting the energy scale, the linearity defined as the unbiased estimate of the standard deviation of $\mu_{E_{calib}}/E_{beam}$ is 0.10% for the Monte Carlo simulation and 0.28% for the data. This is within the estimated systematic uncertainties discussed in section 5.6.6. Therefore the linearity at the CTB 2004 is understood at the level of the estimated systematic uncertainties.

The resolution shown in figure 5.34 is described by

$$\frac{\sigma_{E_{Calib}}(E_{beam})}{E_{beam}} = \frac{a}{\sqrt{E_{beam}}} \oplus \frac{b}{E_{beam}} \oplus c \qquad (5.16)$$

Run number	$p_{beam}^{nominal}$ (GeV/c)	Noise (MeV)
2102399	100	209.7
2102400	50	207.4
2102413	20	207.4
2102452	80	207.9

Table 5.5: Noise values for the 3x7 clusters for all beam momenta.

where the first term in the quadratic sum is the stochastic term, the second the noise term and the third the local constant term as described in chapter 3. Since the noise of the read out electronics was measured regularly during the whole CTB 2004 data taking period by taking dedicated calibration runs, the noise values for the 3x7 clusters have been subtracted quadratically for every measurement point in figure 5.34 before. They have been computed for each run by averaging the noise values for the clusters over all events of the runs. The noise value of a given cluster was computed as the quadratic sum of the noise values of all cells in the cluster in their chosen read out gain for the given event. The noise value of a given cell in a given read out gain was taken from the previously mentioned calibration runs. The noise values are shown in table 5.5. The noise increases slightly with increasing beam momentum because more cells are read out in medium gain than in high gain due to the higher energy deposits and because the noise for the medium gain is higher than for the high gain. The reason for this difference in the noise for the various gains is the different bin size during digitization for the noise amplified by the preamplifier. The impact of the different gain factors on the noise is compensated by the gain depending $F_{DAC \to \mu A} \cdot F_{\mu A \to \mathrm{MeV}}$ factor (see section 5.5.1).

Therefore the fit to extract a is done with $b = 0$ and $c = 0.2\%$ which is known from previous test beams. The value for a extracted by the fit is $(9.7 \pm 0.1)\%$ GeV$^{1/2}$ for Monte Carlo simulation and $(10.1 \pm 0.1)\%$ GeV$^{1/2}$ for data which is compatible with previous test beam results without magnetic field. It is the first measurement of a for the ATLAS LAr calorimeter with particles traversing a magnetic field similar as for ATLAS data taking at the LHC. However, the resolution for beam momenta of 80GeV/c and higher is too small in the Monte Carlo simulation.

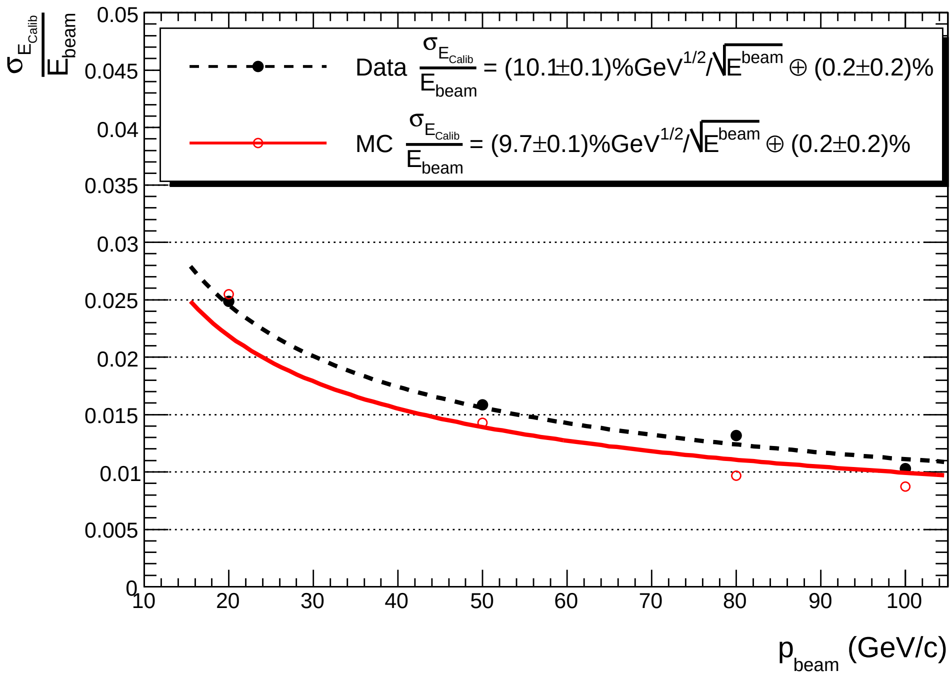

Figure 5.34: Relative energy resolution for Monte Carlo simulation and data for all beam momenta after noise subtraction.

6 Intercalibration with E/p for the Combined Test Beam 2004

This chapter presents a method to intercalibrate the energy scale of the electromagnetic calorimeter and the momentum scale of the Inner Detector. The intercalibration is performed by investigating the ratio E/p for electrons, i.e. the ratio of the energy E measured by the electromagnetic calorimeter and the momentum p measured by the Inner Detector. This method was developed and tested with test beam data and has been applied to ATLAS Monte Carlo simulations (see chapter 7).

The key concept of this intercalibration method is to extract information for the detector response functions of the electromagnetic calorimeter, i.e. E/p_{beam}, and of the Inner Detector, i.e. p_{beam}/p, from a fit to the E/p distribution. In order to be able to achieve this, the E/p distribution has to be parameterized through the two individual detector response functions E/p_{beam} and p_{beam}/p. Since E/p_{beam} and p_{beam}/p describe not necessarily uncorrelated random variables, their correlation also has to be taken into account for the E/p parameterization. Since the knowledge of the true momentum of the particles, i.e. p_{beam}, is necessary to obtain a description of this correlation and this knowledge will not be available for ATLAS, the correlation is computed for Monte Carlo simulation.

The E/p parameterization is fitted to the observed E/p distribution and since it is built upon the individual detector response functions, the fit parameters obtained from the E/p fit reflect the properties of the individual response functions. This chapter is devoted to the extraction of the relative scale of the two individual response functions. Since the momentum scale of the Inner Detector is determined by the magnetic field that has been measured very precisely [38], the relative scale can be used to transform the momentum scale into the absolute energy scale of the electromagnetic calorimeter.

For each beam momentum p_{beam} the intercalibration is done in the following steps:

1. Derive parameterizations for the E/p_{beam} and p_{beam}/p distributions. For this step,

the knowledge of the beam momentum is necessary.

2. E/p is modeled by convoluting E/p_{beam} and p_{beam}/p. This can be done by treating E/p_{beam} and p_{beam}/p as independent random variables or by taking their correlation into account. The knowledge of the beam momentum is used for the description of the correlation.

3. The parameterization for E/p is fitted to the observed E/p distribution. All parameters except a relative scale parameter are kept fixed to their values obtained in step 1.

The modeling of the E/p distribution is described in section 6.1. The details of the relative scale extraction procedure are described in section 6.2 and results for combined test beam data and Monte Carlo simulation are shown in section 6.3.

6.1 Modeling

6.1.1 Motivation

As presented in figure 5.32 in section 5.8 the energy response of the electromagnetic calorimeter to a particle with a given momentum is not gaussian, showing a tail towards lower energies. This comes from energy deposits due to bremsstrahlung in the material upstream to the calorimeter. Using the calibration hits in the simulation and plotting the energy of the particle $E_{beam} = p_{beam}\, c$ minus the energy lost upstream relative to the energy of the particle (figure 6.1) shows this fact. The asymmetry of the curves in figure 6.1 is partly corrected by the presampler in the Calibration Hits Method (see section 5.7.1), however the tail is not completely removed and therefore has to be taken into account for modeling the energy distribution.

6.1.2 Modeling of E/p_{beam}

Convolution model

Motivated by figure 6.1 one can make the following exponential ansatz to model the beam energy minus the energy lost upstream of the calorimeter normalized to the beam energy

$$f_e(e; \tau_E, E_0) := c\, \frac{1}{\tau_E E_0\left(e^{\tau_E} - 1\right)} e^{\frac{e}{\tau_E E_0}}, e < E_0 \tag{6.1}$$

where E_0 is a scale parameter and τ_E describes the tail towards lower energies.

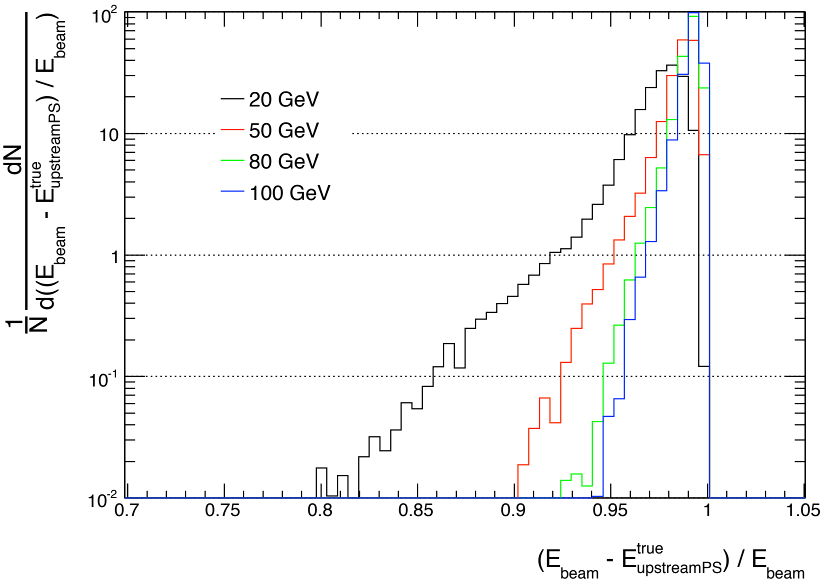

Figure 6.1: Relative energy content that reaches the calorimeter for all beam momenta computed with Monte Carlo simulation. It can be seen that the tail towards lower energies is approximately linear in the log–scale plot, i.e. exponential.

Next the detector resolution without upstream material can be modeled with a gaussian with standard deviation σ_E:

$$D(x;\sigma_E) := \frac{1}{\sqrt{2\pi}\sigma_E} e^{\frac{-x^2}{2\sigma_E^2}} \tag{6.2}$$

Convoluting (6.1) and (6.2) to get the energy response of the calorimeter leads to

$$E(e;\tau_E,E_0,\sigma_E) = \int_0^{E_0} f_e(x;\tau_E,E_0)\, D(e-x;\sigma_E)\, dx \tag{6.3}$$

$$= c\,\frac{e^{\frac{2eE_0\tau_E+\sigma_E^2}{2E_0{}^2\tau_E{}^2}}\left(\mathrm{Erf}\left[\frac{eE_0\tau_E+\sigma_E{}^2}{\sqrt{2}E_0\tau_E\sigma_E}\right]-\mathrm{Erf}\left[\frac{eE_0\tau_E-E_0{}^2\tau_E+\sigma_E{}^2}{\sqrt{2}E_0\tau_E\sigma_E}\right]\right)}{2\left(e^{\frac{1}{\tau_E}}-1\right)E_0\tau_E} \tag{6.4}$$

where $\mathrm{Erf}(x)$ denotes the gaussian error function defined by

$$\mathrm{Erf}(x) = \int_0^x e^{-t^2}\, dt. \tag{6.5}$$

The parameters τ_E, E_0, σ_E depend on the beam momentum p_{beam}. The position of the peak of the distribution $E(e;\tau_E,E_0,\sigma_E)$, denoted μ_e is a function of the parameters

material	τ_E (10^{-2})	σ_E (10^{-2})	E_0	$\mu_e(\tau_E, E_0, \sigma_E)$
nominal	4.84(6)	2.66(7)	1.0275(4)	1.0013(5)
additional	5.78(11)	2.32(9)	1.0267(7)	1.0003(7)

Table 6.1: The parameter values for the convolution model (equation 6.3) obtained from a fit to the E/p_{beam} distribution for a beam momentum of p_{beam}=20 GeV/c without (*nominal*) and with additional material in the Inner Detector.

τ_E, E_0, σ_E, i.e. $\mu_e = \mu_e(\tau_E, E_0, \sigma_E)$.

This parameterization is capable of describing the effect of additional material in front of the electromagnetic calorimeter. Since additional material should not affect the intrinsic detector resolution, only the parameter τ_E should change. For a beam momentum of 20 GeV/c additional material equivalent to 10% of a radiation length was placed between the Pixel detector and the SCT and additional 20% between the SCT and the TRT. The E/p_{beam} distribution without (solid line) and with (dashed line) this additional material in the Inner Detector is shown in figure 6.2 together with the corresponding fits with the convolution model. The obtained parameters are given in table 6.1. The two values of E_0 (with and without additional material) are compatible within the error bars, whereas μ_e is as expected slightly lower for the run with additional material. There is some correlation between the resolution σ_E and the tail parameter τ_E. The difference of the resolution σ_E for the different material description is of the order of 3 standard deviations, but the tail parameter τ_E is approximately 10 standard deviations larger for the geometry description with additional material demonstrating the sensitivity of this parameter to additional material in front of the electromagnetic calorimeter.

Although the convolution model describes the E/p_{beam} distributions at p_{beam}=20 GeV/c very well, the Crystall Ball model presented in the next subsection describes the E/p_{beam} distributions far better at beam momenta above 20 GeV/c. The Crystall Ball model is therefore used for the combined test beam 2004 for E/p_{beam} distributions for the sake of consistency.

Crystall Ball model

The E/p_{beam} distribution, see figure 5.32, for the CTB 2004 is modeled using the so–called Crystall Ball function. The Crystal Ball function [39], named after the Crystal Ball Collaboration, is a probability density function commonly used to model various processes in high energy physics. It consists of a Gaussian core part and a power-law low-end tail below a certain threshold. These two parts are spliced together (via the coefficients A and B) in such a way that the function and its first derivative are both continuous. The Crystall Ball function f_{CB} is given by

$$f_{CB}(x;\alpha,n,\mu,\sigma) = N \cdot \begin{cases} \exp(-\frac{(x-\mu)^2}{2\sigma^2}) & \text{for } \frac{x-\mu}{\sigma} > -\alpha \\ A \cdot (B - \frac{x-\mu}{\sigma})^{-n} & \text{for } \frac{x-\mu}{\sigma} \leq -\alpha \end{cases} \tag{6.6}$$

where

$$\begin{aligned} A &= \left(\frac{n}{|\alpha|}\right)^n \cdot \exp\left(-\frac{|\alpha|^2}{2}\right) \\ B &= \frac{n}{|\alpha|} - |\alpha| \; . \end{aligned} \tag{6.7}$$

N is a normalization factor and α, n, μ and σ are parameters.

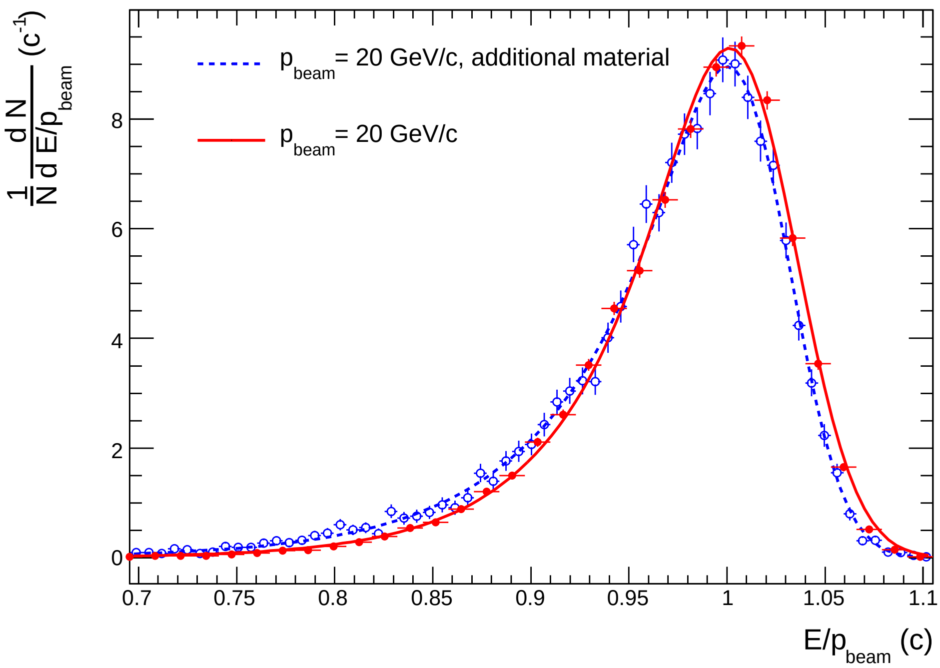

Figure 6.2: The E/p_{beam} distribution for a beam momentum of p_{beam}=20 GeV/c fitted with the convolution model (equation 6.3) without (solid line) and with (dashed line) additional material in the Inner Detector.

The model for the E/p_{beam} distribution, denoted $E(e;\alpha_e,n_e,\mu_e,\sigma_e)$, is given by

$$E(e;\alpha_e,n_e,\mu_e,\sigma_e) = c\, f_{CB}(e;\alpha_e,n_e,\mu_e,\sigma_e) \tag{6.8}$$

where $e = E/p_{beam}$. The parameters $\alpha_e, n_e, \mu_e, \sigma_e$ depend on the beam momentum p_{beam}.

6.1.3 Modeling of p_{beam}/p

The p_{beam}/p distribution for the CTB 2004 is modeled using a Crystall Ball function that is mirrored at $x = \mu$ which is

$$f_{mirror}(x;\alpha,n,\mu,\sigma) = f_{CB}(\mu-(x-\mu);\alpha,n,\mu,\sigma) = f_{CB}(2\mu - x;\alpha,n,\mu,\sigma) \tag{6.9}$$

with the Crystall Ball function defined in equations 6.6 and 6.7.

The model for the p_{beam}/p distribution, denoted $Q(q;\alpha_q,n_q,\mu_q,\sigma_q)$, is given by

$$Q(q;\alpha_q,n_q,\mu_q,\sigma_q) = f_{mirror}(q;\alpha_q,n_q,\mu_q,\sigma_q) \tag{6.10}$$

where $q = p_{beam}/p$.

6.1.4 Modeling of E/p

For electrons in the considered energy range ($E > 1\text{GeV} \gg m_e \approx 511\text{keV}$) we neglect the mass term contribution to the particle energy and therefore use the approximation $E = pc$. Since the measurement variables e and q are random variables, the distribution R of the product $r = e \cdot q$, which describes the ratio E/p, is given by

$$R(r) = \int_{-\infty}^{\infty} f_{(E,Q)}\left(\frac{r}{w}, w\right) \frac{1}{w}\, dw \tag{6.11}$$

where $f_{(E,Q)}(e,q)$ denotes the joint distribution of e and q. Using the parameterizations $E(e;\alpha_e,n_e,\mu_e,\sigma_e)$ and $Q(q;\alpha_q,n_q,\mu_q,\sigma_q)$ for e (equation 6.8) and q (equation 6.10) and the fact that $E(e) > 0\,\forall e \in \mathbb{R}$ and $Q(q) > 0\,\forall q \in \mathbb{R}$, the joint distribution can be rewritten as

$$f_{(E,Q)}\left(e,q;\alpha_e,n_e,\mu_e,\sigma_e,\alpha_q,n_q,\mu_q,\sigma_q\right) = E(e;\alpha_e,n_e,\mu_e,\sigma_e)\, Q(q;\alpha_q,n_q,\mu_q,\sigma_q) \cdot C(e,q) \tag{6.12}$$

where $C(e, q)$ describes the correlation between e and q. No correlation would be equivalent to $C(e, q) = 1$. Inserting (6.12) into (6.11) leads to

$$R(r; \alpha_e, n_e, \mu_e, \sigma_e, \alpha_q, n_q, \mu_q, \sigma_q) = \int_{-\infty}^{\infty} E(\frac{r}{w}; \alpha_e, n_e, \mu_e, \sigma_e)\, Q(w; \alpha_q, n_q, \mu_q, \sigma_q)\, C(\frac{r}{w}, w) \frac{1}{w}\, dw \quad (6.13)$$

Two ways of dealing with the correlation between e and q are considered.

No correlation

It is assumed that there is no correlation between e and q, i.e. e and q are independent random variables. For the modeling this means $C(e, q) = 1$ in equation 6.13. This should be the case for high energy electrons where the impact of bremsstrahlung on the momentum measurement is small. Later it will be shown that the correlation between e and q has to be taken into account in order to achieve a precision for the relative scale at the 5‰ level.

Correlation obtained from Monte Carlo simulation

The continous function $C(e, q)$ in equation 6.12 can be approximated by discrete values for bins in e and q. $C(e, q)$ is determined from Monte Carlo simulations by performing the division

$$C(e, q) = \frac{f_{(E,Q)}(e, q)}{E(e)\, Q(q)} \quad (6.14)$$

bin–wise. In order to be able to compute $C(e, q)$ the knowledge of the beam momentum is necessary, but since the computation is performed bin–wise it is independent of the choice of the parameterizations for $E(e)$ and $Q(q)$. The joint distributions $f_{(E,Q)}(e, q)$ of e and q and $C(e, q)$ extracted from Monte Carlo simulations are shown in for p_{beam} =20 GeV/c in figure 6.3, for p_{beam} =50 GeV/c in figure 6.4, for p_{beam} =80 GeV/c in figure 6.5 and for p_{beam} =100 GeV/c in figure 6.6. For p_{beam} =20 GeV/c the correlation factor $C(e, q)$ derived from Monte Carlo simulation shows a gradient in the up–left direction in the parameter space where most of the events are located indicating correlation. This gradient becomes smaller for p_{beam} =50 GeV/c and vanishes for p_{beam} =80 GeV/c and p_{beam} =100 GeV/c. Therefore these figures show that the correlation decreases with increasing beam momentum. Furthermore, the relative error on $C(e, q)$ can become quite large, especially at higher beam momenta. The qualitative behaviour of the correlation in the data is well described by the Monte Carlo simulation, especially at p_{beam}=20GeV/c where the correlation is most important.

The idea is to extract $C(e,q)$ from Monte Carlo simulations and then apply it to data in the same spirit as for the Calibration Hits Method in section 5.7.

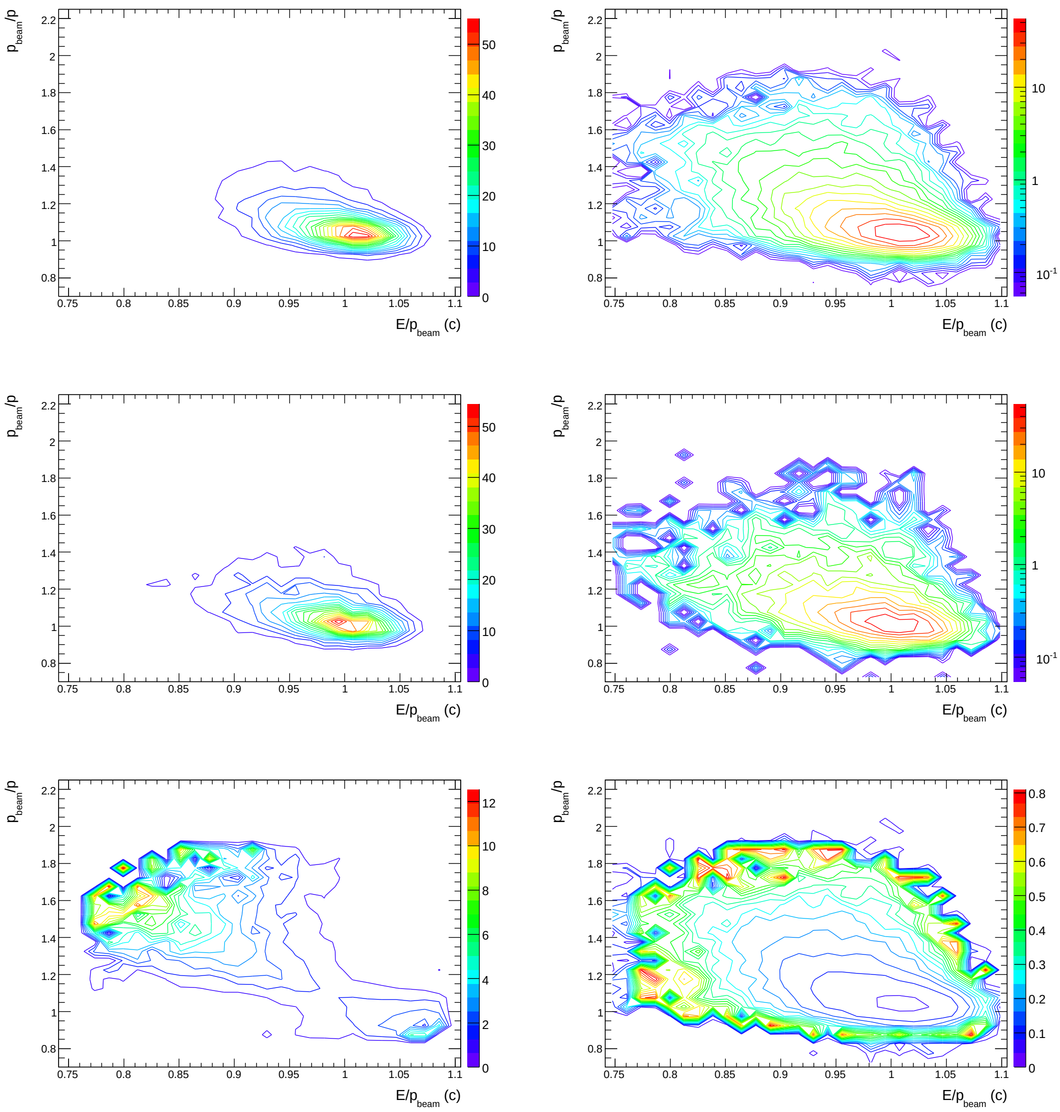

Figure 6.3: The joint distribution $f_{(E,Q)}(e,q)$ (equation 6.11) for Monte Carlo simulation (top left and top right [log scale]), for CTB data (middle left and middle right [log scale]), the correlation factor $C(e,q)$ (equation 6.14) derived from Monte Carlo simulation (bottom left) and the relative error of the correlation factor $C(e,q)$ (bottom right) for p_{beam}=20GeV/c.

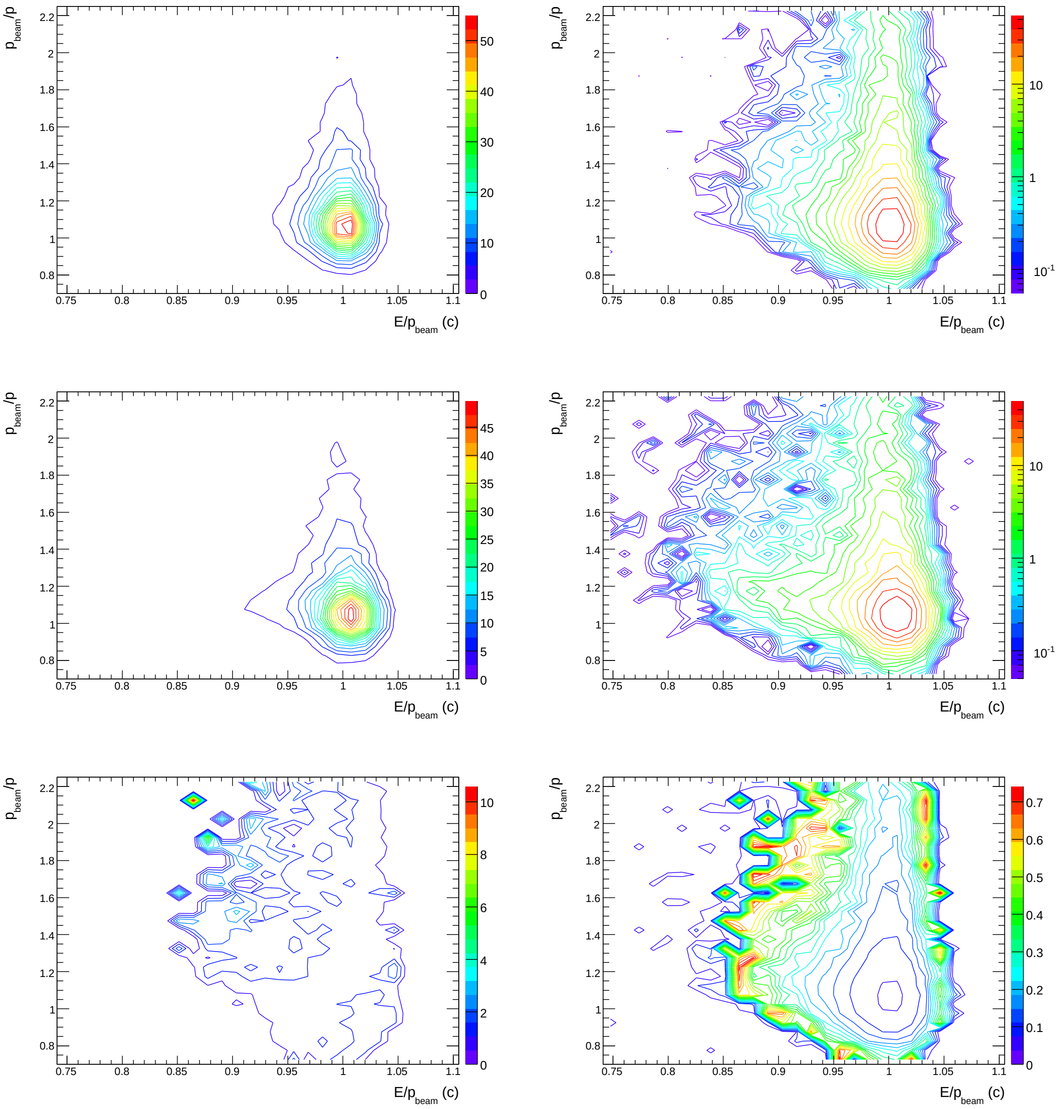

Figure 6.4: The joint distribution $f_{(E,Q)}(e, q)$ (equation 6.11) for Monte Carlo simulation (top left and top right [log scale]), for CTB data (middle left and middle right [log scale]), the correlation factor $C(e, q)$ (equation 6.14) derived from Monte Carlo simulation (bottom left) and the relative error of the correlation factor $C(e, q)$ (bottom right) for p_{beam}=50GeV/c.

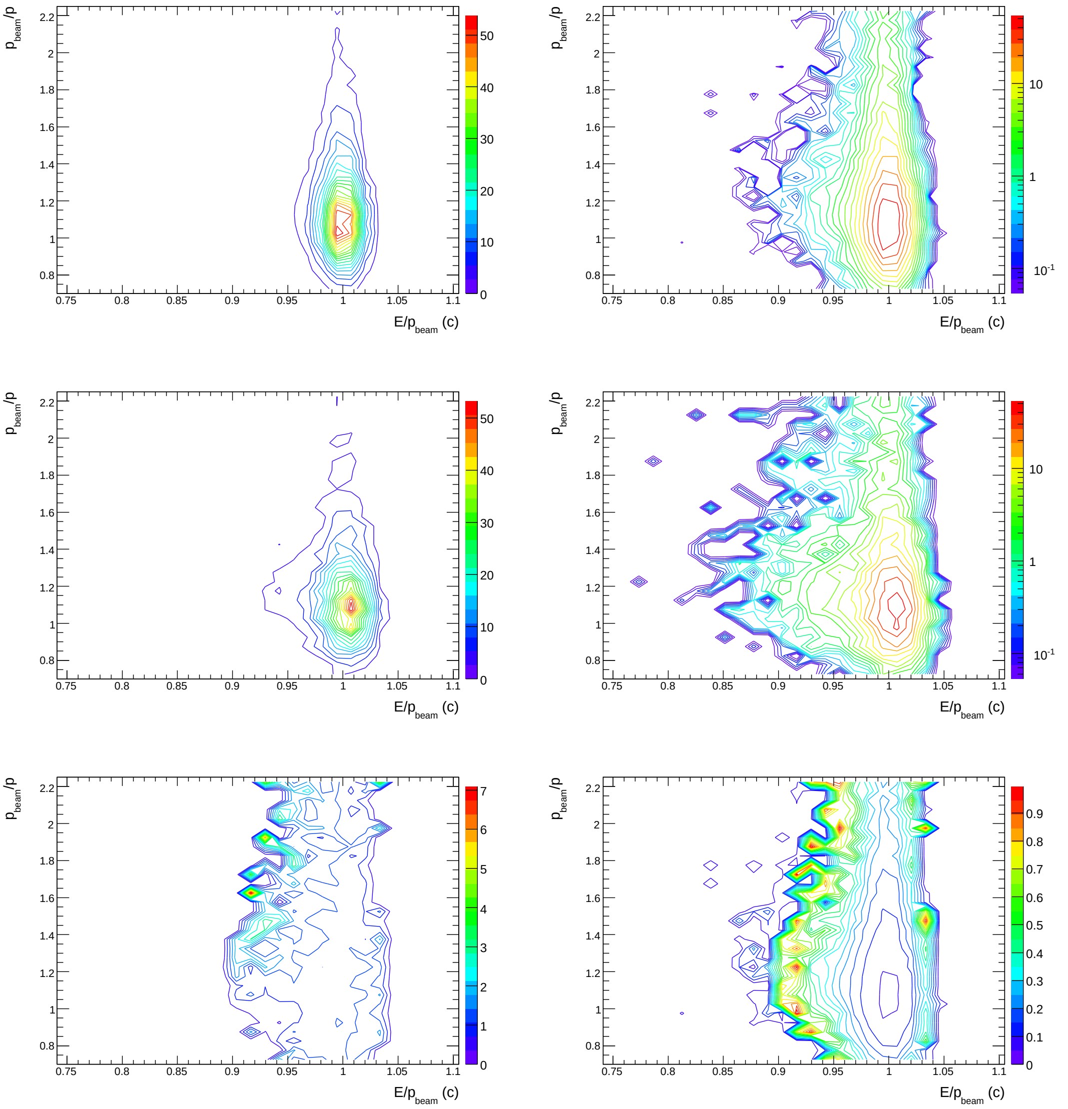

Figure 6.5: The joint distribution $f_{(E,Q)}(e,q)$ (equation 6.11) for Monte Carlo simulation (top left and top right [log scale]), for CTB data (middle left and middle right [log scale]), the correlation factor $C(e,q)$ (equation 6.14) derived from Monte Carlo simulation (bottom left) and the relative error of the correlation factor $C(e,q)$ (bottom right) for p_{beam}=80GeV/c.

6.2 Scale factor extraction

6.2.1 Procedure

This procedure is applied for each beam momentum p_{beam} separately. The parameters $\hat{\alpha}_e, \hat{n}_e, \hat{\mu}_e, \hat{\sigma}_e$ are obtained by fitting the Crystall Ball parameterization $E(e;\alpha_e,n_e,\mu_e,\sigma_e)$

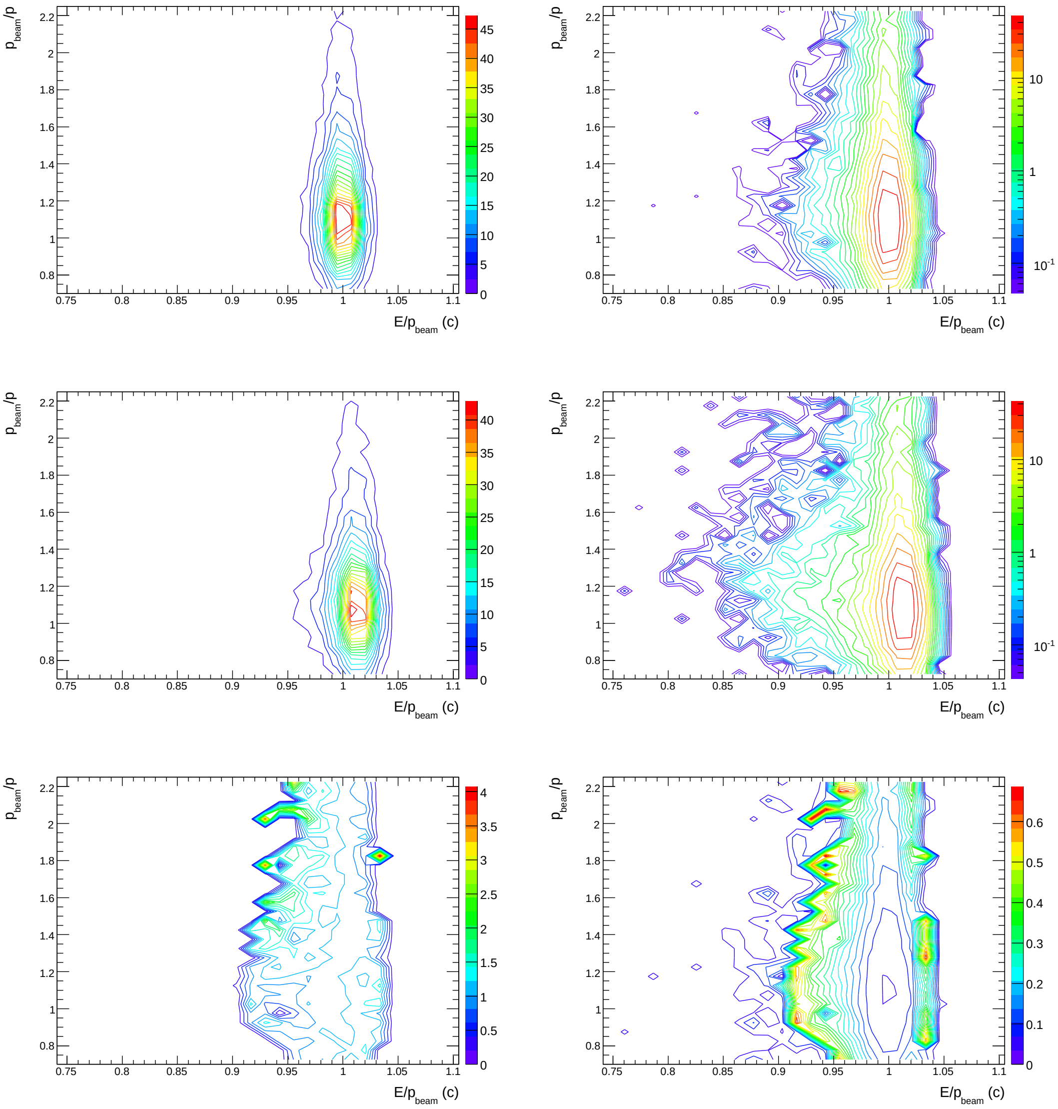

Figure 6.6: The joint distribution $f_{(E,Q)}(e, q)$ (equation 6.11) for Monte Carlo simulation (top left and top right [log scale]), for CTB data (middle left and middle right [log scale]), the correlation factor $C(e, q)$ (equation 6.14) derived from Monte Carlo simulation (bottom left) and the relative error of the correlation factor $C(e, q)$ (bottom right) for p_{beam}=100GeV/c.

(equation 6.8) to the E/p_{beam} distribution. The parameters $\hat{\alpha}_q, \hat{n}_q, \hat{\mu}_q, \hat{\sigma}_q$ are computed by fitting the mirror Crystall Ball parameterization $Q(q; \alpha_q, n_q, \mu_q, \sigma_q)$ (equation 6.10) to the p_{beam}/p distribution. Then the scale parameter $\bar{\mu}_e$ for the E/p_{beam} distribution is calculated by fitting $R(r; \hat{\alpha}_e, \hat{n}_e, \bar{\mu}_e, \hat{\sigma}_e, \hat{\alpha}_q, \hat{n}_q, \hat{\mu}_q, \hat{\sigma}_q)$ (equation 6.13) to the E/p distribution. In this fit only the $\bar{\mu}_e$ parameter is allowed to vary. The other parameters

$\hat{\alpha}_e, \hat{n}_e, \hat{\sigma}_e, \hat{\alpha}_q, \hat{n}_q, \hat{\mu}_q, \hat{\sigma}_q$ are fixed to the values obtained by the E/p_{beam} and p_{beam}/p fits, respectively. The relative scale factor is then defined by the ratio $\bar{\mu}_e/\hat{\mu}_e$.

This procedure is based on the assumption that the relative scale factor is close to 1 and therefore the effect of the scaling of the parameters $\hat{\alpha}_e, \hat{n}_e, \hat{\sigma}_e$ is negligible. Otherwise they would have to be scaled accordingly.

6.2.2 Validation and estimation of systematic errors

The procedure to extract the relative scale factor between the energy scale of the electromagnetic calorimeter and the momentum scale of the inner detector is validated using a dedicated Monte Carlo simulation. The inputs for the Monte Carlo simulation are the number of events N to be generated, the probability density function $t(p_{beam})$ for the beam momentum and the parameterizations for $E(e; p_{beam})$ and $Q(q; p_{beam})$ as functions of the beam momentum. Note that $t(p_{beam})$ can be a Dirac delta function for a specific beam momentum or a function modeling the true momentum distribution of electrons coming for a specific physics process, e.g. W$\rightarrow$eν, in the ATLAS experiment.

An event is generated in the following steps:

1. Generate a random beam momentum $\hat{p}_{beam}$ from $t(p_{beam})$,
2. generate a random $\hat{e}$ from $E(e; \hat{p}_{beam})$,
3. generate a random $\hat{q}$ from $Q(q; \hat{p}_{beam})$.
4. compute $\hat{r} = \hat{e}\,\hat{q}$ (This means that no correlation between e and q is assumed.).

All the generated $\hat{e}$, $\hat{q}$ and $\hat{r}$ form the $\hat{E}(\hat{e})$, $\hat{Q}(\hat{q})$ and $\hat{R}(\hat{r})$ distributions. Then the procedure described in the previous subsection 6.2.1 is applied and the relative scale factor $\bar{\mu}_e/\hat{\mu}_e$ is extracted.

To estimate the errors arising from the fitting procedure, the procedure for a given N and $t(p_{beam})$ has been repeated 10^4 times in the Monte Carlo simulation with different seeds for the random number generator. Each time the relative scale factor $\bar{\mu}_e/\hat{\mu}_e$ is computed and accumulated. The mean and the standard deviation of the distribution of the relative scale factor $\bar{\mu}_e/\hat{\mu}_e$ is examined to validate the scale factor extraction procedure. This distribution is shown for $t(p_{beam}) = \delta(50\text{GeV/c})$ and N=1000 and for $t(p_{beam})$ distributed like the true momentum of electrons coming from W$\rightarrow$eν decays (figure 6.8) and N=8000 in figure 6.7. For $t(p_{beam}) = \delta(50\text{GeV/c})$ the $\bar{\mu}_e/\hat{\mu}_e$ distribution is nicely gaussian whereas for the W→eν decay momentum distribution, which is itself asymmetric, it is asymmetric. Therefore the mean of the distribution is used instead of the mean of a gaussian fitted to the distribution.

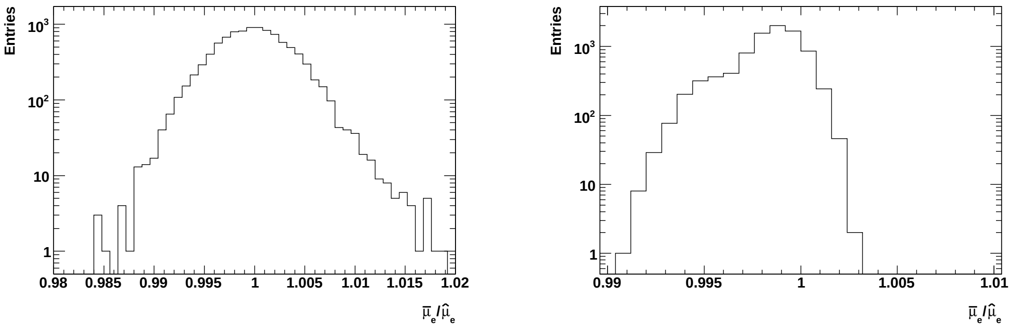

Figure 6.7: Distribution of the relative scale factor $\bar{\mu}_e/\hat{\mu}_e$ for $t(p_{beam}) = \delta(50\text{GeV/c})$ and N=1000 (left) and for $t(p_{beam})$ distributed as the true momentum of electrons coming from W→eν decays (figure 6.8) and N=8000 (right).

The mean and the standard deviation of the distribution of the relative scale factor $\bar{\mu}_e/\hat{\mu}_e$ are plotted as functions of N in figure 6.9 for the following beam momentum probability density functions $t(p_{beam})$:

- $t(p_{beam}) = \delta(20\text{GeV/c})$,
- $t(p_{beam}) = \delta(50\text{GeV/c})$,
- $t(p_{beam}) = \delta(100\text{GeV/c})$,
- $t(p_{beam})$ gaussian with μ=40GeV/c and σ=10GeV/c,
- $t(p_{beam})$ uniformly distributed between 20 GeV/c and 60 GeV/c,
- $t(p_{beam})$ distributed like the true momentum of electrons coming from W→eν decays (figure 6.8)
- $t(p_{beam})$ distributed like the true momentum of electrons coming from W→eν decays for p_{beam} <80 GeV/c
- $t(p_{beam})$ distributed like the true momentum of electrons coming from W→eν decays 20 GeV/c< p_{beam} <60 GeV/c

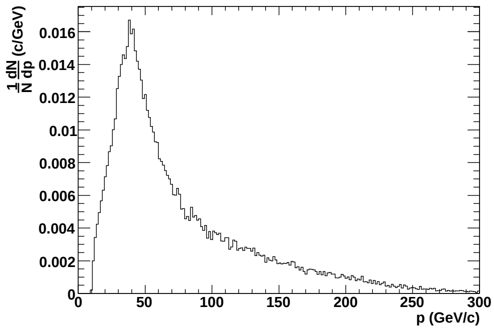

Figure 6.8: Momentum distribution of electrons coming from W→eν decays obtained with PYTHIA.

From figure 6.9 it is clear that the standard deviation of the distribution of the relative scale factor $\bar{\mu}_e/\hat{\mu}_e$ (shown as error bars) decreases with increasing N as it is expected. However after N=4000 the improvement gets very small implying that this is a good working point with a standard deviation of ≈1.5‰.

The mean of the distribution of the relative scale factor $\bar{\mu}_e/\hat{\mu}_e$ is within 1‰; for $t(p_{beam})$ distributed like the momentum of electrons from W→eν decays it is within 2‰due to the asymmetric shape of the distribution of the relative scale factor $\bar{\mu}_e/\hat{\mu}_e$ for this case. When the p_{beam} is restricted to be within 0 GeV/c< p_{beam} <60 GeV/c or 20 GeV/c< p_{beam} <60 GeV/c, the mean of the distribution of the relative scale factor $\bar{\mu}_e/\hat{\mu}_e$ stays within 1‰, and well within the errors.

6.3 Scale parameter extraction for the Combined Test Beam

The E/p_{beam} distribution with the fitted $E(e;\hat{\alpha}_e,\hat{n}_e,\hat{\mu}_e,\hat{\sigma}_e)$ model, the p_{beam}/p distribution with the fitted $Q(q;\hat{\alpha}_q,\hat{n}_q,\hat{\mu}_q,\hat{\sigma}_q)$ model and the E/p_{beam} distribution fitted with $R(r;\hat{\alpha}_e,\hat{n}_e,\bar{\mu}_e,\hat{\sigma}_e,\hat{\alpha}_q,\hat{n}_q,\hat{\mu}_q,\hat{\sigma}_q)$ without and with Monte Carlo simulation correlation modeling are plotted in figure 6.10 (Monte Carlo simulation) and figure 6.11 (data) for p_{beam}=20 GeV/c, in figure 6.12 (Monte Carlo simulation) and figure 6.13 (data) for p_{beam}=50 GeV/c, in figure 6.14 (Monte Carlo simulation) and figure 6.15 (data) for p_{beam}=80 GeV/c and in figure 6.16 (Monte Carlo simulation) and figure 6.17 (data) for p_{beam}=100 GeV/c. The number of events after all cuts is given in table 6.2.

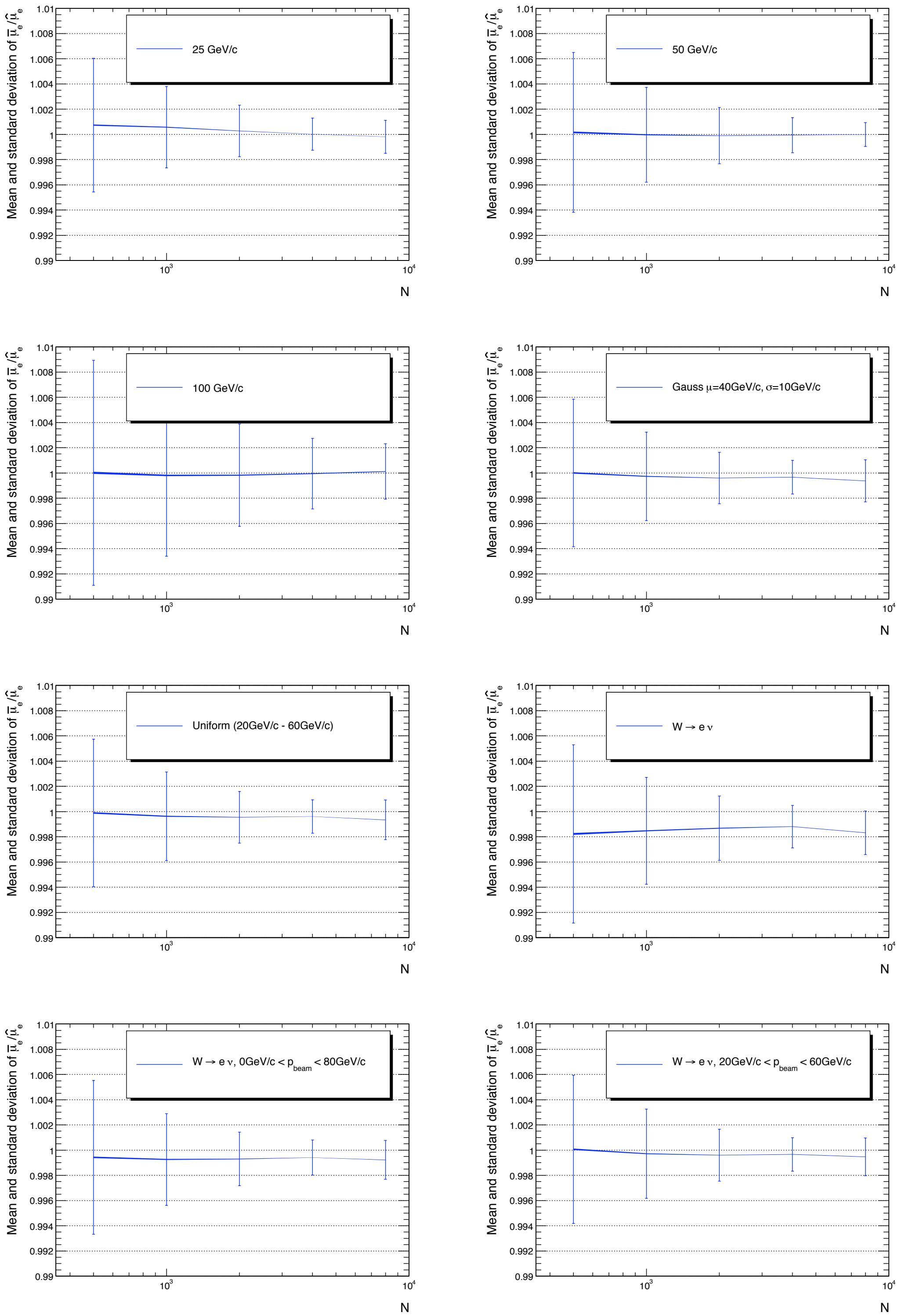

Figure 6.9: Mean (band representing the error on the mean) and standard deviation (error bars) of the distribution of the relative scale factor $\bar{\mu}_e/\hat{\mu}_e$ as functions of N for different beam momentum probability density distributions $t(p_{beam})$.

Run number	$p_{beam}^{nominal}$ (GeV/c)	Events MC	Events Data
2102399	100	55665	19075
2102400	50	56151	19723
2102413	20	41600	6583
2102452	80	57473	8180

Table 6.2: Number of events after all cuts for the Monte Carlo simulation and the data for all beam momenta.

For p_{beam}=20 GeV/c and for p_{beam}=50 GeV/c the modeling of the correlation between e and q is needed to improve the description of the shape of the E/p distributions. The E/p distribution for data for p_{beam}=20 GeV/c is not perfectly described by applying the correlation obtained from the Monte Carlo simulation implying that the correlation is larger in data than in the Monte Carlo simulation. For p_{beam}=50 GeV/c the E/p distribution for data is well described using the correlation obtained from the Monte Carlo simulation. For p_{beam}=80 GeV/c and for p_{beam}=100 GeV/c the modeling of the correlation between e and q yields only small improvements and introduces numerical problems. They lead to small shape distortions around the peak of the E/p model functions.

The relative scale factor $\bar{\mu}_e/\hat{\mu}_e$ without and with Monte Carlo simulation correlation modeling is plotted in figure 6.18 for all beam momenta. For p_{beam}=80 GeV/c and higher the modeling of the correlation between e and q does not improve the relative scale factor. For p_{beam}=50 GeV/c and specially for p_{beam}=20 GeV/c the modeling of the correlation between e and q brings the relative scale factor down to the 2 respectively 5 permill level. Within the available statistics, the uncertainties on the relative scale factor are comparable with the expectation from the dedicated validation Monte Carlo simulation model.

This demonstrates that for the CTB 2004 a Monte Carlo simulation correlation modeling can be used to extract the relative scale factor $\bar{\mu}_e/\hat{\mu}_e$ from the data and therefore a similar approach will be used for ATLAS. The description of the correlation should be easier for ATLAS since the material distribution upstream of the electromagnetic calorimeter is much better understood for ATLAS than for the CTB 2004.

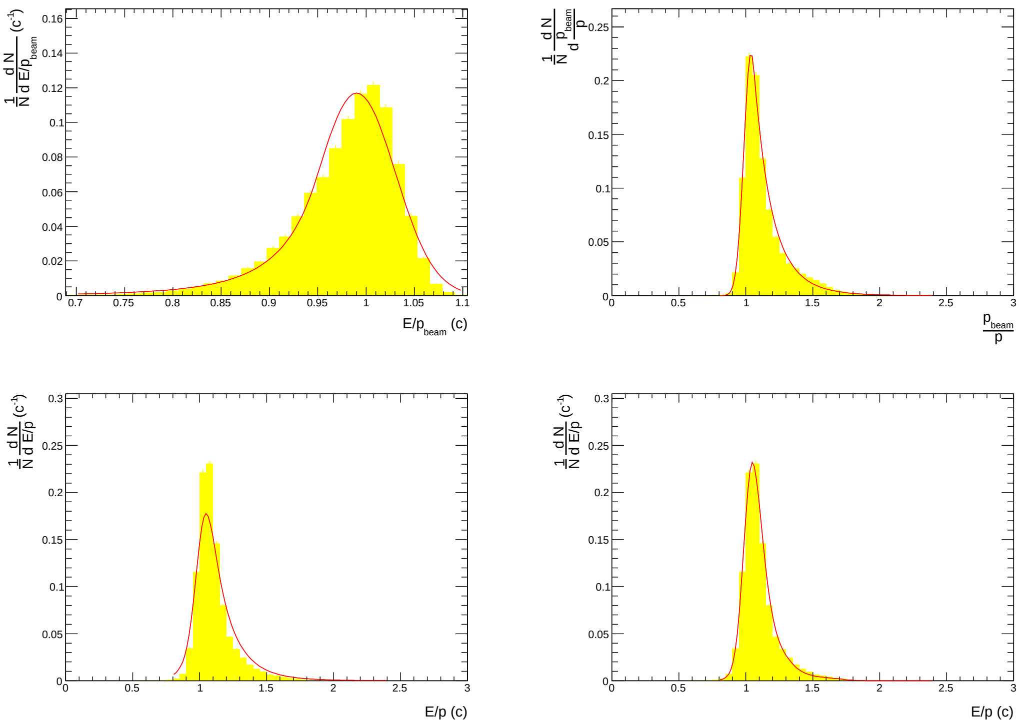

Figure 6.10: Monte Carlo simulation: The E/p_{beam} distribution with the fitted $E(e; \hat{\alpha}_e, \hat{n}_e, \hat{\mu}_e, \hat{\sigma}_e)$ model (top left), the p_{beam}/p distribution with the fitted $Q(q; \hat{\alpha}_q, \hat{n}_q, \hat{\mu}_q, \hat{\sigma}_q)$ model (top right) and the E/p_{beam} distribution fitted with $R(r; \hat{\alpha}_e, \hat{n}_e, \bar{\mu}_e, \hat{\sigma}_e, \hat{\alpha}_q, \hat{n}_q, \hat{\mu}_q, \hat{\sigma}_q)$ without (bottom left) and with (bottom right) Monte Carlo simulation correlation modeling for Monte Carlo simulation for p_{beam}=20GeV/c.

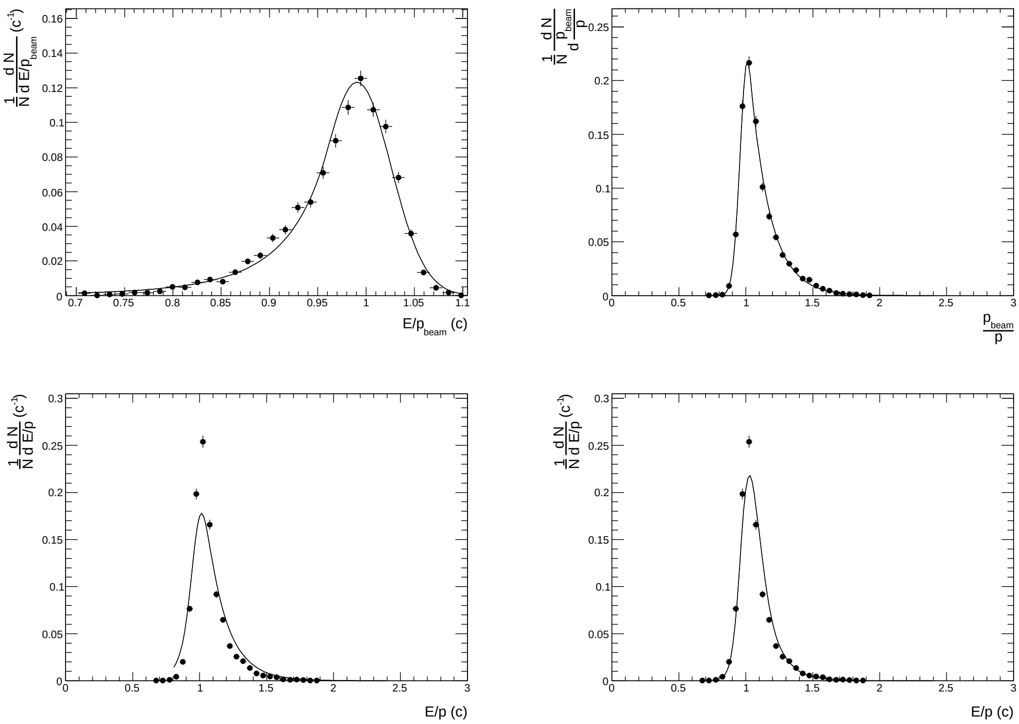

Figure 6.11: CTB data: The E/p_{beam} distribution with the fitted $E(e;\hat{\alpha}_e,\hat{n}_e,\hat{\mu}_e,\hat{\sigma}_e)$ model (top left), the p_{beam}/p distribution with the fitted $Q(q;\hat{\alpha}_q,\hat{n}_q,\hat{\mu}_q,\hat{\sigma}_q)$ model (top right) and the E/p_{beam} distribution fitted with $R(r;\hat{\alpha}_e,\hat{n}_e,\bar{\mu}_e,\hat{\sigma}_e,\hat{\alpha}_q,\hat{n}_q,\hat{\mu}_q,\hat{\sigma}_q)$ without (bottom left) and with (bottom right) Monte Carlo simulation correlation modeling for CTB data for p_{beam}=20GeV/c.

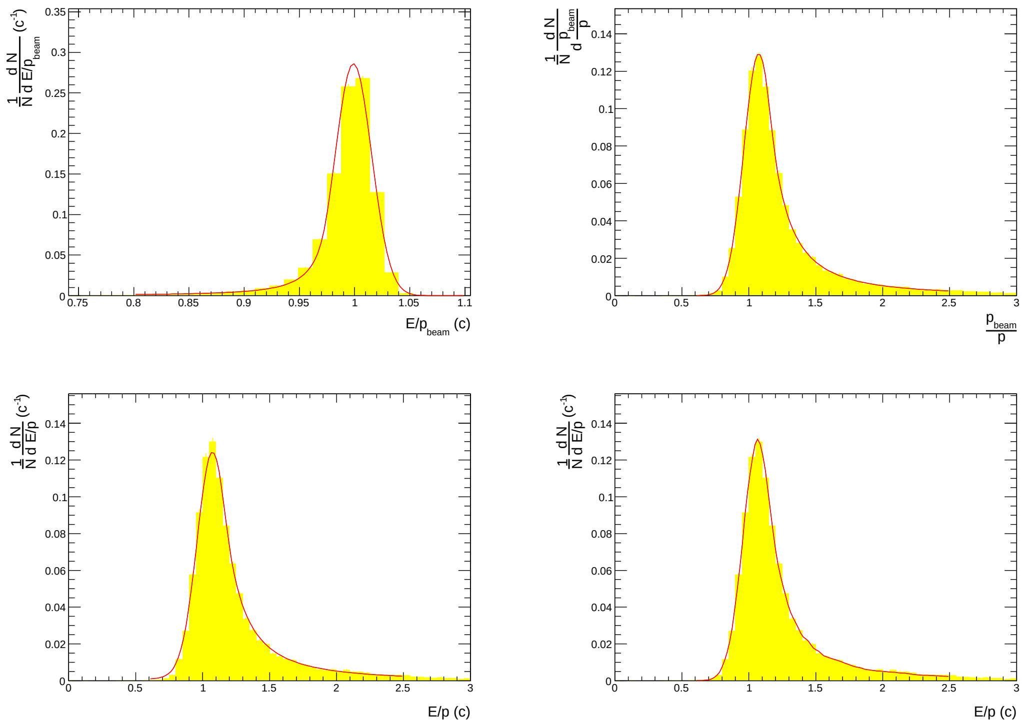

Figure 6.12: Monte Carlo simulation: The E/p_{beam} distribution with the fitted $E(e;\hat{\alpha}_e,\hat{n}_e,\hat{\mu}_e,\hat{\sigma}_e)$ model (top left), the p_{beam}/p distribution with the fitted $Q(q;\hat{\alpha}_q,\hat{n}_q,\hat{\mu}_q,\hat{\sigma}_q)$ model (top right) and the E/p_{beam} distribution fitted with $R(r;\hat{\alpha}_e,\hat{n}_e,\bar{\mu}_e,\hat{\sigma}_e,\hat{\alpha}_q,\hat{n}_q,\hat{\mu}_q,\hat{\sigma}_q)$ without (bottom left) and with (bottom right) Monte Carlo simulation correlation modeling for Monte Carlo simulation for p_{beam}=50GeV/c.

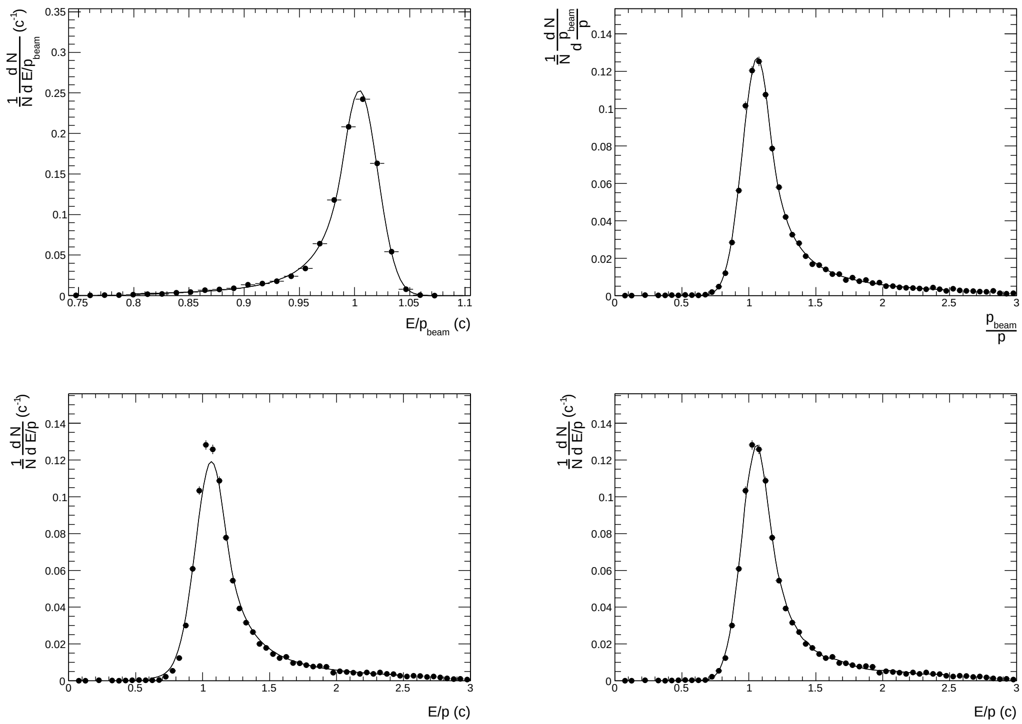

Figure 6.13: CTB data: The E/p_{beam} distribution with the fitted $E(e;\hat{\alpha}_e,\hat{n}_e,\hat{\mu}_e,\hat{\sigma}_e)$ model (top left), the p_{beam}/p distribution with the fitted $Q(q;\hat{\alpha}_q,\hat{n}_q,\hat{\mu}_q,\hat{\sigma}_q)$ model (top right) and the E/p_{beam} distribution fitted with $R(r;\hat{\alpha}_e,\hat{n}_e,\bar{\mu}_e,\hat{\sigma}_e,\hat{\alpha}_q,\hat{n}_q,\hat{\mu}_q,\hat{\sigma}_q)$ without (bottom left) and with (bottom right) Monte Carlo simulation correlation modeling for CTB data for p_{beam}=50GeV/c.

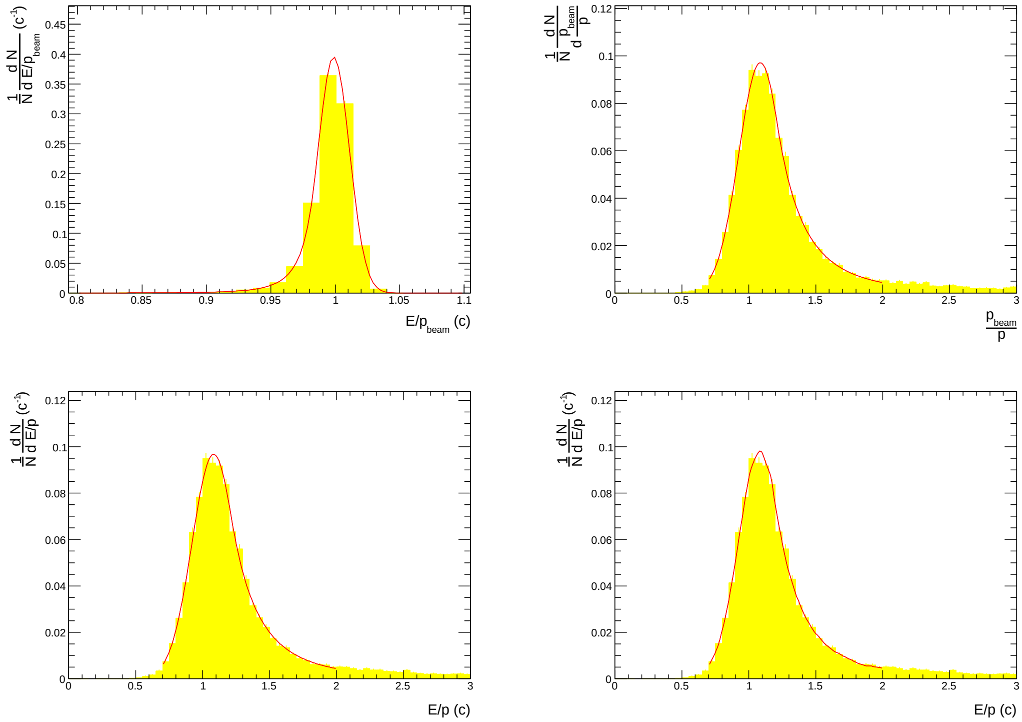

Figure 6.14: Monte Carlo simulation: The E/p_{beam} distribution with the fitted $E(e;\hat{\alpha}_e,\hat{n}_e,\hat{\mu}_e,\hat{\sigma}_e)$ model (top left), the p_{beam}/p distribution with the fitted $Q(q;\hat{\alpha}_q,\hat{n}_q,\hat{\mu}_q,\hat{\sigma}_q)$ model (top right) and the E/p_{beam} distribution fitted with $R(r;\hat{\alpha}_e,\hat{n}_e,\bar{\mu}_e,\hat{\sigma}_e,\hat{\alpha}_q,\hat{n}_q,\hat{\mu}_q,\hat{\sigma}_q)$ without (bottom left) and with (bottom right) Monte Carlo simulation correlation modeling for Monte Carlo simulation for p_{beam}=80GeV/c.

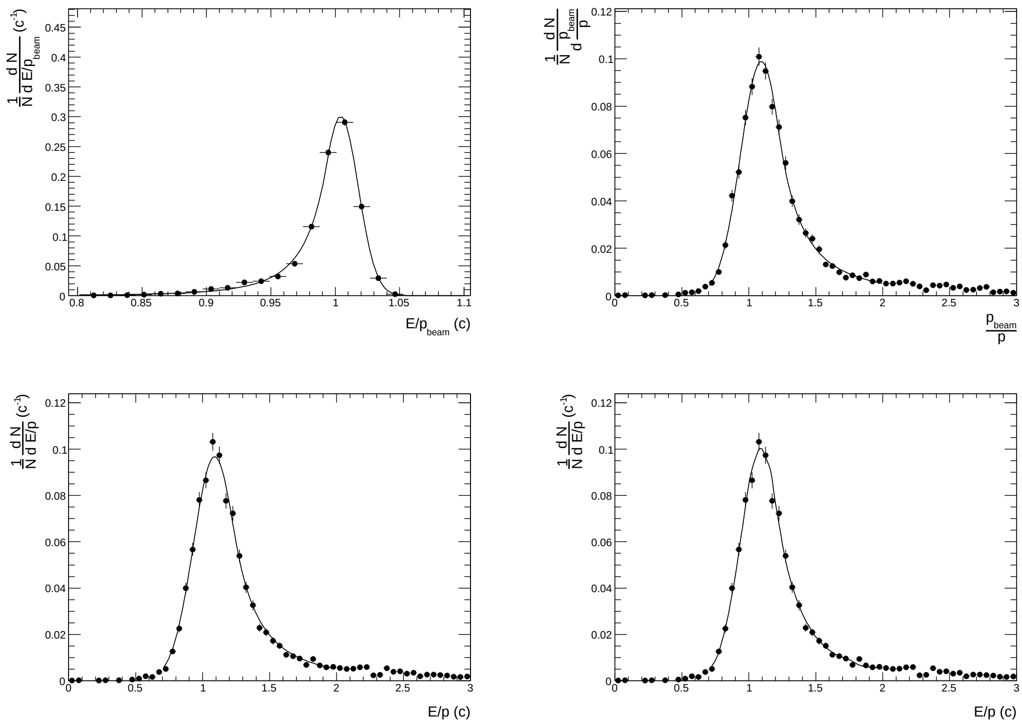

Figure 6.15: CTB data: The E/p_{beam} distribution with the fitted $E(e;\hat{\alpha}_e,\hat{n}_e,\hat{\mu}_e,\hat{\sigma}_e)$ model (top left), the p_{beam}/p distribution with the fitted $Q(q;\hat{\alpha}_q,\hat{n}_q,\hat{\mu}_q,\hat{\sigma}_q)$ model (top right) and the E/p_{beam} distribution fitted with $R(r;\hat{\alpha}_e,\hat{n}_e,\bar{\mu}_e,\hat{\sigma}_e,\hat{\alpha}_q,\hat{n}_q,\hat{\mu}_q,\hat{\sigma}_q)$ without (bottom left) and with (bottom right) Monte Carlo simulation correlation modeling for CTB data for p_{beam}=80GeV/c.

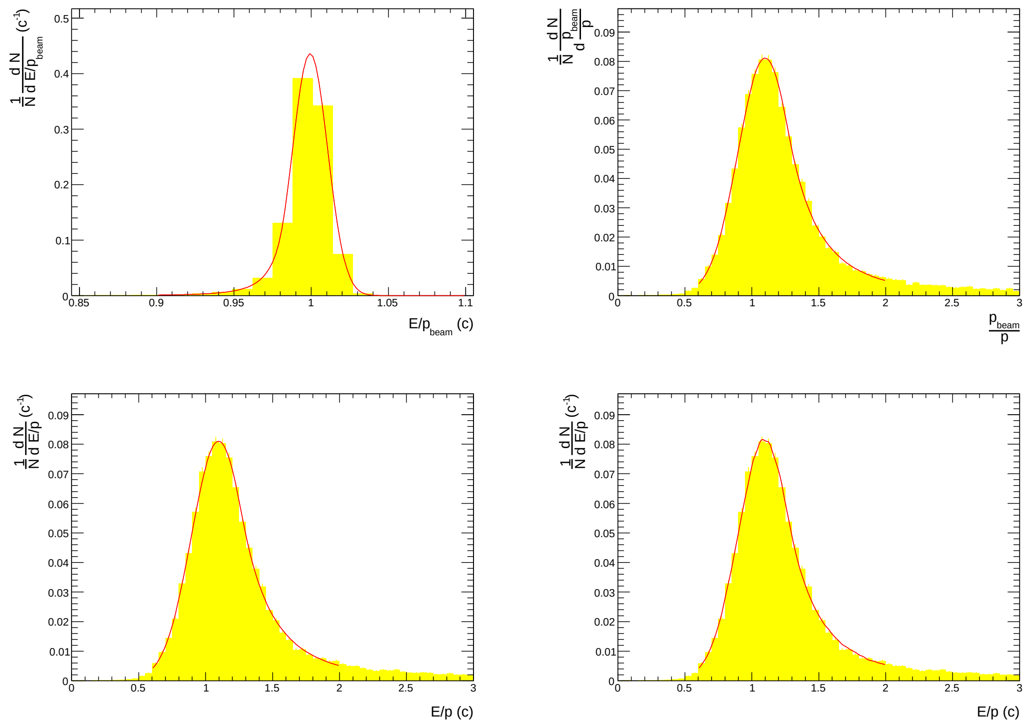

Figure 6.16: Monte Carlo simulation: The E/p_{beam} distribution with the fitted $E(e;\hat{\alpha}_e,\hat{n}_e,\hat{\mu}_e,\hat{\sigma}_e)$ model (top left), the p_{beam}/p distribution with the fitted $Q(q;\hat{\alpha}_q,\hat{n}_q,\hat{\mu}_q,\hat{\sigma}_q)$ model (top right) and the E/p_{beam} distribution fitted with $R(r;\hat{\alpha}_e,\hat{n}_e,\bar{\mu}_e,\hat{\sigma}_e,\hat{\alpha}_q,\hat{n}_q,\hat{\mu}_q,\hat{\sigma}_q)$ without (bottom left) and with (bottom right) Monte Carlo simulation correlation modeling for Monte Carlo simulation for p_{beam}=100GeV/c.

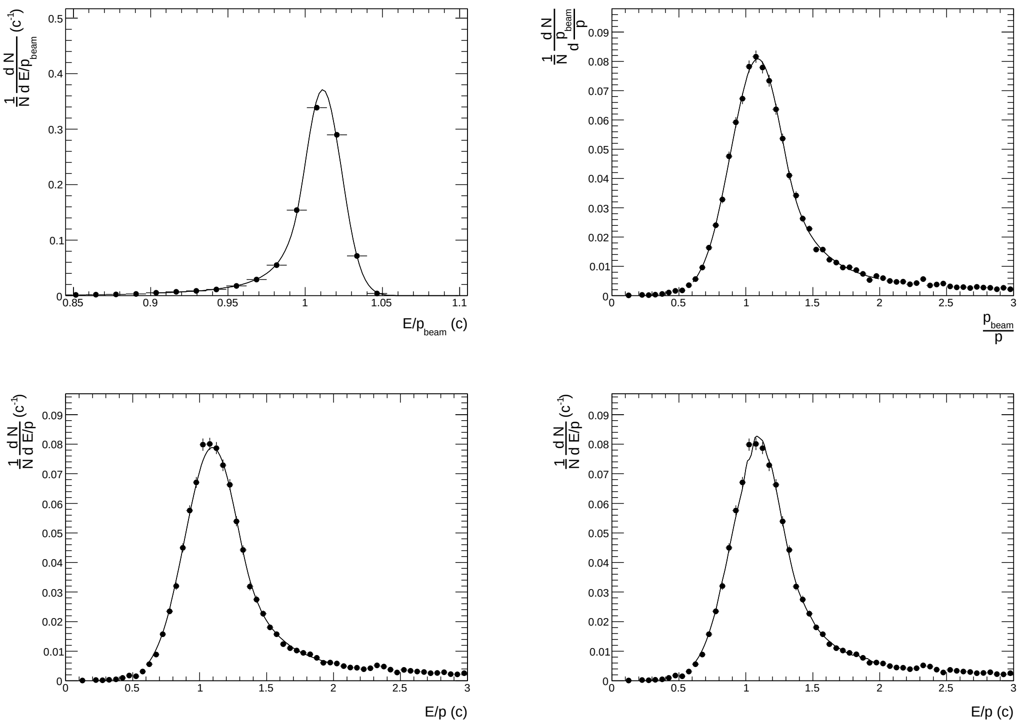

Figure 6.17: CTB data: The E/p_{beam} distribution with the fitted $E(e;\hat{\alpha}_e,\hat{n}_e,\hat{\mu}_e,\hat{\sigma}_e)$ model (top left), the p_{beam}/p distribution with the fitted $Q(q;\hat{\alpha}_q,\hat{n}_q,\hat{\mu}_q,\hat{\sigma}_q)$ model (top right) and the E/p_{beam} distribution fitted with $R(r;\hat{\alpha}_e,\hat{n}_e,\bar{\mu}_e,\hat{\sigma}_e,\hat{\alpha}_q,\hat{n}_q,\hat{\mu}_q,\hat{\sigma}_q)$ without (bottom left) and with (bottom right) Monte Carlo simulation correlation modeling for CTB data for p_{beam}=100GeV/c.

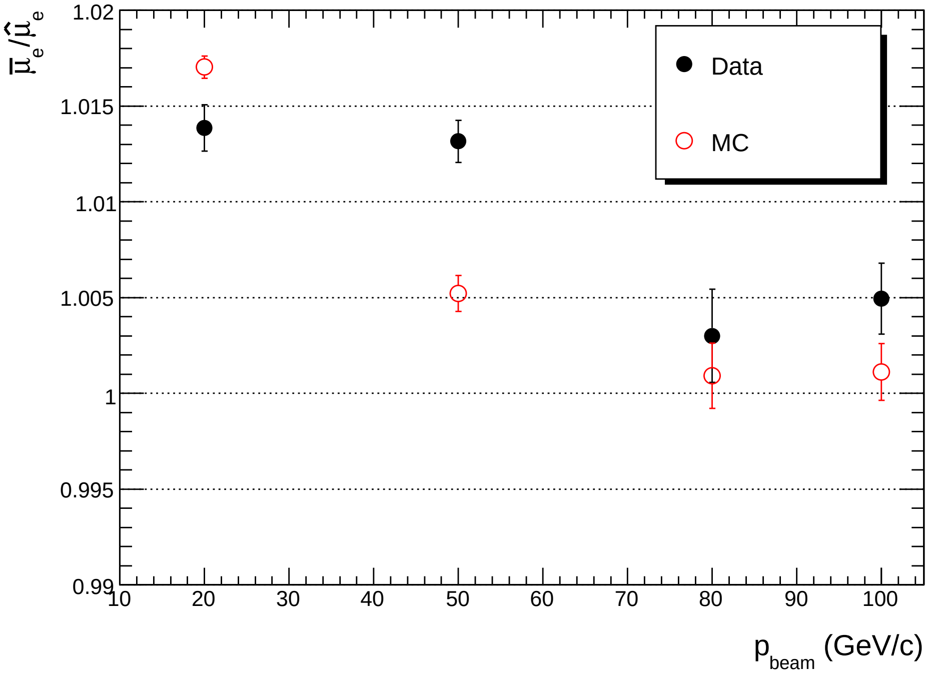

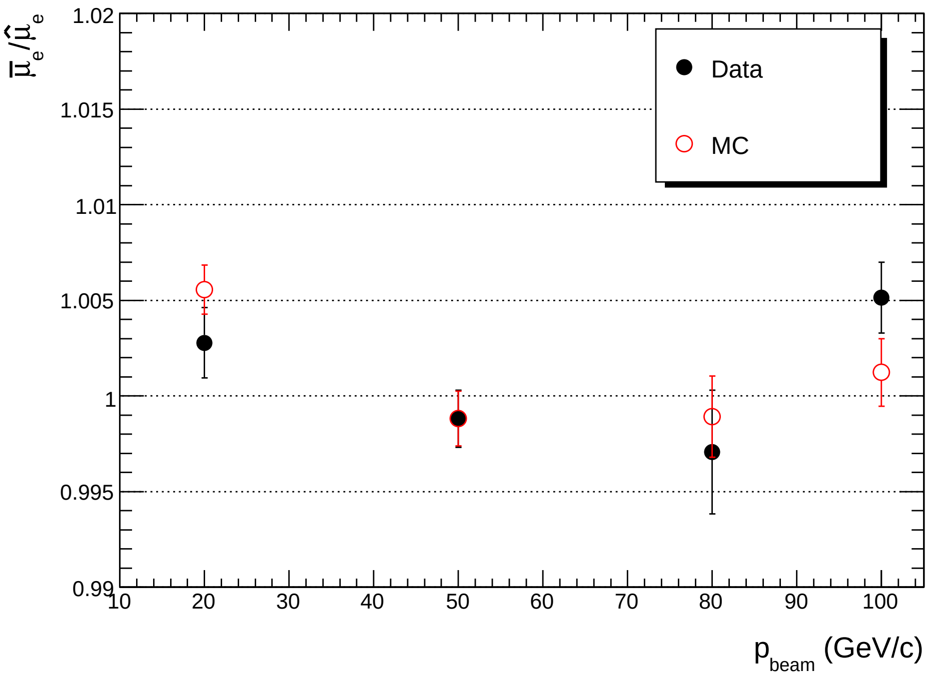

Figure 6.18: The relative scale factor $\bar{\mu}_e/\hat{\mu}_e$ extracted from the E/p distributions without (top) and with (bottom) correlation weighting for Monte Carlo simulation and data for all beam momenta.

6.4 Summary

In this chapter I have developed a parameterization of the E/p distribution that takes the correlation between the energy E measured by the electromagnetic calorimeter and the momentum p measured by the Inner Detector into account. After describing the procedure to extract the relative scale between the two detectors using this parameterization of the E/p distribution, this procedure has been applied to data from the Combined Test Beam 2004. Since the momentum scale of the Inner Detector is determined by the very precisely measured magnetic field, the obtained precision for the absolute energy scale for the electromagnetic calorimeter is 5‰.

7 Intercalibration with E/p for ATLAS using Monte Carlo Simulation

In this chapter the method to intercalibrate the energy scale of the electromagnetic calorimeter and the momentum scale of the Inner Detector which was developed for the combined test beam 2004 (chapter 6) is applied to the Monte Carlo simulations for the ATLAS detector.

The main difference between the two scenarios is that while in the combined test beam 2004 the particle momentum could be adjusted to a specific value, for data taken with ATLAS from LHC collisions the particle momentum is not known a priori. Therefore the parameterizations of the two individual detector response functions and the E/p distribution are generalized to accomodate the distribution of the true particle momentum. Electrons from specific physics processes, where the distribution of the true particle momentum is known, will be used for the intercalibration method in ATLAS.

The modeling of the E/p distribution with an emphasis on the differences with respect to the combined test beam 2004 is described in section 7.1. Section 7.2 is devoted to the physics processes that produce electrons with a sufficient rate to be used for the intercalibration method. The details of the relative scale extraction procedure are described in section 7.4 and results for ATLAS Monte Carlo simulation are shown in section 7.4.

7.1 Modeling

This section describes the modeling of the E/p distribution for electrons from a given physics process (see section 7.2). A specific physics process together with the event and particle selection defines the true momentum distribution $t(p_{true}, \eta, \varphi)$ which also depends on the geometric position (η and φ) where the electron impinges the calorimeter.

Since the performance of the calorimeter and the inner detector varies over the geometrical coverage of the detector systems, a rectangular binning in the (η, φ) space is introduced. Since the model coefficients vary from bin to bin, the modeling of the E/p distribution described in this section is performed for every bin separately. An η–φ bin is specified by the lower and upper bounds on η and φ, i.e. $\eta_{min} < \eta < \eta_{max}$ and $\varphi_{min} < \varphi < \varphi_{max}$.

7.1.1 Modeling of E/p_{true}

The response function of the LAr electromagnetic calorimeter, i.e. the E/p_{true} distribution denoted $E(e)$ where $e = E/p_{true}$, is a function of the geometrical position where the electron impinges in the calorimeter, i.e. η and φ, and of the true electron momentum p_{true}. This means that $E(e) = E(e; \eta, \varphi, p_{true})$. For a given η–φ bin, i.e. $\eta_{min} < \eta < \eta_{max}$ and $\varphi_{min} < \varphi < \varphi_{max}$, and a given true particle momentum distribution after event and particle selection $t(p_{true}, \eta, \varphi)$ the mean response function $E_\Sigma(e)$ is

$$E_\Sigma(e) = \int_{\eta_{min}}^{\eta_{max}} \int_{\varphi_{min}}^{\varphi_{max}} \int_0^\infty t(p_{true}, \eta, \varphi)\, E(e; \eta, \varphi, p_{true}) dp_{true}\, d\varphi\, d\eta. \tag{7.1}$$

This function is parameterized using the convolution model (equation 6.3 in subsection 6.1.2), i.e.

$$E_\Sigma(e) = E_\Sigma(e; \tau_e, E_0, \sigma_e). \tag{7.2}$$

The position of the peak of the distribution $E_\Sigma(e; \tau_e, E_0, \sigma_e)$, denoted μ_e, is a function of the parameters τ_e, E_0, σ_e, i.e. $\mu_e = \mu_e(\tau_e, E_0, \sigma_e)$.

7.1.2 Modeling of p_{true}/p

The p_{true}/p distribution, denoted $Q(q)$ where $q = p_{true}/p$ is a function of the geometrical position where the electron passes through the Inner Detector, i.e. η and φ, and of the true electron momentum p_{true}. Analogous to the response function of the LAr electromagnetic calorimeter described in the previous subsection 7.1.1, this means that $Q(q) = Q(q; \eta, \varphi, p_{true})$. For a given η–φ bin, i.e. $\eta_{min} < \eta < \eta_{max}$ and $\varphi_{min} < \varphi < \varphi_{max}$, and a given true particle momentum distribution after event and particle selection $t(p_{true}, \eta, \varphi)$ the mean p_{true}/p distribution $Q_\Sigma(q)$ is

$$Q_\Sigma(q) = \int_{\eta_{min}}^{\eta_{max}} \int_{\varphi_{min}}^{\varphi_{max}} \int_0^\infty t(p_{true}, \eta, \varphi)\, Q(q; \eta, \varphi, p_{true}) dp_{true}\, d\varphi\, d\eta. \tag{7.3}$$

This function is modeled like the p_{beam}/p distribution for the CTB 2004 (subsection 6.1.3) with a mirrored Crystall Ball function (equation 6.9), i.e.

$$Q_\Sigma(q) = Q_\Sigma(q; \alpha_q, n_q, \mu_q, \sigma_q). \tag{7.4}$$

7.1.3 Modeling of E/p

For electrons in the considered energy range ($E > 1\text{GeV} \gg m_e \approx 511\text{keV}$) we neglect the mass term contribution to the particle energy and therefore use the approximation $E = pc$. Since the measurement variables e and q are random variables, the distribution R of the product $r = e \cdot q$, which describes the ratio E/p, for a given η position, φ position and a given true electron momentum p_{true} is

$$R(r; \eta, \varphi, p_{true}) = \int_{-\infty}^{\infty} f_{(E,Q)}\left(\frac{r}{w}, w; \eta, \varphi, p_{true}\right) \frac{1}{w}\, dw \tag{7.5}$$

where $f_{(E,Q)}(e, q; \eta, \varphi, p_{true})$ denotes the joint distribution of e and q for the given η position, the given φ position and the given true electron momentum p_{true}. For a given η–φ bin, i.e. $\eta_{min} < \eta < \eta_{max}$ and $\varphi_{min} < \varphi < \varphi_{max}$, and a given true particle momentum distribution after event and particle selection $t(p_{true}, \eta, \varphi)$ the mean E/p distribution $R_\Sigma(r)$ is

$$R_\Sigma(r) = \int\limits_{\eta_{min}}^{\eta_{max}} \int\limits_{\varphi_{min}}^{\varphi_{max}} \int\limits_{0}^{\infty} t(p_{true}, \eta, \varphi)\, R(r; \eta, \varphi, p_{true}) dp_{true}\, d\varphi\, d\eta. \tag{7.6}$$

This function is far too complicated to be evaluated in a parameter fitting procedure. Furthermore the joint distribution would have to be known for a larger volume in the $(p_{true}, \eta, \varphi)$ parameter space. Therefore the joint distribution $f_{(E,Q)}(e, q; \eta, \varphi, p_{true})$ is approximated by a mean joint distribution $f^*_{(E,Q)}\left(\frac{r}{w}, w\right)$ for a given η–φ bin and a given true particle momentum distribution after event and particle selection $t(p_{true}, \eta, \varphi)$. Together with rearranging the sequence of the integrations and using the fact that $t(p_{true}, \eta, \varphi)$ is a probability density function this yields

$$R_\Sigma(r) = \int\limits_{\eta_{min}}^{\eta_{max}} \int\limits_{\varphi_{min}}^{\varphi_{max}} \int\limits_{0}^{\infty} t(p_{true}, \eta, \varphi)\, R(r; \eta, \varphi, p_{true}) dp_{true}\, d\varphi\, d\eta \tag{7.7}$$

$$= \int_{\eta_{min}}^{\eta_{max}} \int_{\varphi_{min}}^{\varphi_{max}} \int_{0}^{\infty} t(p_{true}, \eta, \varphi) \int_{-\infty}^{\infty} f_{(E,Q)} \left(\frac{r}{w}, w; \eta, \varphi, p_{true} \right) \frac{1}{w} \, dw \, dp_{true} \, d\varphi \, d\eta \quad (7.8)$$

$$\approx \int_{-\infty}^{\infty} f^{*}_{(E,Q)} \left(\frac{r}{w}, w \right) \frac{1}{w} \, dw \underbrace{\int_{\eta_{min}}^{\eta_{max}} \int_{\varphi_{min}}^{\varphi_{max}} \int_{0}^{\infty} t(p_{true}, \eta, \varphi) \, dp_{true} \, d\varphi \, d\eta}_{=1} \quad (7.9)$$

$$= \int_{-\infty}^{\infty} f^{*}_{(E,Q)} \left(\frac{r}{w}, w \right) \frac{1}{w} \, dw. \quad (7.10)$$

This approximation can also be interpreted in the following way: Instead of taking the $(p_{true}, \eta, \varphi)$ substructure of $E(e)$ and $Q(q)$ into account, e and q are simply treated as random variables for a given η–φ bin, i.e. $\eta_{min} < \eta < \eta_{max}$ and $\varphi_{min} < \varphi < \varphi_{max}$, and a given true particle momentum distribution after event and particle selection $t(p_{true}, \eta, \varphi)$. They are distributed according to the E_Σ and the Q_Σ distributions with a joint distribution $f_{\Sigma,(E,Q)}(e, q)$. Analogue to subsection 6.1.4 the corresponding distribution R_Σ of the product $r = e \cdot q$ is

$$R_\Sigma(r) = \int_{-\infty}^{\infty} f_{\Sigma,(E,Q)} \left(\frac{r}{w}, w \right) \frac{1}{w} \, dw, \quad (7.11)$$

where $f_{\Sigma,(E,Q)}(e, q)$ denotes the joint distribution of e and q and is used as the mean joint distribution $f^{*}_{(E,Q)} \left(\frac{r}{w}, w \right)$. Using the parameterizations $E_\Sigma(e; \tau_e, E_0, \sigma_e)$ and $Q_\Sigma(q; \alpha_q, n_q, \mu_q, \sigma_q)$ for e (equation 7.2) and q (equation 7.4) and the fact that $E_\Sigma(e) > 0 \, \forall e \in \mathbb{R}$ and $Q_\Sigma(q) > 0 \, \forall q \in \mathbb{R}$, the joint distribution can be rewritten as

$$f_{\Sigma,(E,Q)} \, (e, q) = E_\Sigma(e) \, Q_\Sigma(q) \cdot C_\Sigma(e, q) \quad (7.12)$$

where $C_\Sigma(e, q)$ describes the correlation between e and q. No correlation would be equivalent to $C_\Sigma(e, q) = 1$. Inserting (6.12) into (6.11) leads to

$$R_\Sigma(r; \tau_e, E_0, \sigma_e, \alpha_q, n_q, \mu_q, \sigma_q) = \int_{-\infty}^{\infty} E_\Sigma(\frac{r}{w}; \tau_e, E_0, \sigma_e) \, Q_\Sigma(w; \alpha_q, n_q, \mu_q, \sigma_q) \, C_\Sigma(\frac{r}{w}, w) \frac{1}{w} \, dw \quad (7.13)$$

which is the model that is used in this analysis.

Similar to the combined test beam 2004 (subsection 6.1.4) two ways of dealing with the correlation between e and q are considered.

No correlation

It is assumed that there is no correlation between e and q, i.e. e and q are independent random variables. For the modeling this means $C_\Sigma(e,q) = 1$ in equation 6.13. This should be the case for high energy electrons where the impact of bremsstrahlung on the momentum measurement is small.

Correlation obtained from Monte Carlo simulation

The continous function $C_\Sigma(e,q)$ in equation 7.12 can be approximated by discrete values for bins in e and q. $C_\Sigma(e,q)$ is determined from Monte Carlo simulations by performing the division

$$C_\Sigma(e,q) = \frac{f_{\Sigma,(E,Q)}(e,q)}{E_\Sigma(e)\,Q_\Sigma(q)} \tag{7.14}$$

bin–wise. In order to be able to compute $C_\Sigma(e,q)$ the knowledge of the true particle momentum is necessary, but since the computation is performed bin–wise it is independent of the choice of the parameterizations for $E(e)$ and $Q(q)$.

The idea is to extract $C_\Sigma(e,q)$ from Monte Carlo simulations and then apply it to data like it has been done for the combined test beam 2004 (section 6.1.4)

7.2 Physics processes

A chosen physics process together with the event and particle selection defines the true particle momentum distribution after event and particle selection $t(p_{true}, \eta, \varphi)$ for every η–φ bin. This true particle momentum distribution is needed as an input for the modeling of the E/p distribution in section 7.1.

The five physics processes with the largest electron production cross sections are discussed in the following subsections.

7.2.1 W boson decays

The electrons that are most likely to be used for the intercalibration of the relative scales of the inner detector and the electromagnetic calorimeter are electrons from W boson decays, i.e. a W boson decaying into an electron and its antineutrino, abbreviated as W→eν. For a center of mass energy of 10 TeV the expected cross section is σ=11.764 nb.

The expected efficiency for these events passing the trigger and having an electron in the geometrical acceptance of the Inner Detector and the electromagnetic calorimeter is ϵ=0.88. The $p_{T,true}$ distribution[1] obtained from Monte Carlo simulation for an integrated luminosity = $20\,\mathrm{pb}^{-1}$ is shown in figure 7.1. The $p_{T,true}$ distributions peak slightly below 40 GeV/c and the electron in these events is generally well isolated.

7.2.2 Z boson decays

Electrons from Z bosons decaying into 2 electrons, i.e. $Z \rightarrow e^+e^-$, have a similar p_T spectrum as the electrons from W boson decays and are also well isolated in general. However, the cross section for Z boson decays is approximately 10 times smaller than for W boson decays. Since two electrons are produced per Z boson decay, the number of electrons from Z boson decays is approximately 5 times smaller than from W boson decays. Due to this fact the electrons from Z boson decays will only increase the available statistics by 20% and are therefore of less relevance than the electrons from W boson decays.

7.2.3 Top quark decays

Another source of electrons are top quarks decays. The primary decay channel is the top quark decaying into a b quark and a W boson [40], $t \rightarrow W\,b$. This yields an electron in the case of a leptonic W boson decay, i.e. the W boson decaying into an electron and a neutrino $W \rightarrow e\nu$. The electrons from top quark decays have a similar p_T spectrum as the electrons from W boson decays with a slightly larger tail towards high p_T because they can be more boosted.

The cross section for electrons from top quark decays is much lower than the cross section for electrons from W boson decays. Therefore electrons from top quark decays are not considered in this thesis. Due to the larger tail and with a significant amount of integrated luminosity, electrons for top quark decays are a source for high p_T electrons that can be used to probe the linearity of the electromagnetic calorimeter up to a few hundred GeV.

[1] The true transverse particle momentum is shown instead of the true particle momentum because the p_T spectrum is constant as a function of η for many processes. For a given η position the transverse momentum and the momentum are geometrically related via $p_T = p\,\sin(\theta)$ with $\theta = 2\,\arctan\left(e^{-|\eta|}\right)$.

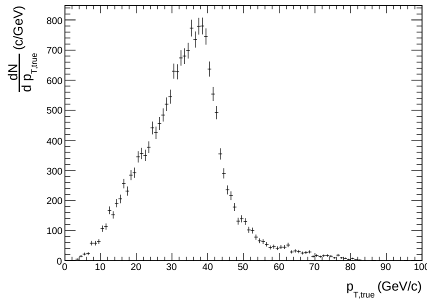

(a) $-2.47 \leq \eta \leq -1.52$

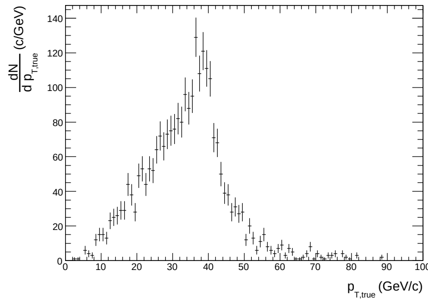

(b) $-1.52 \leq \eta \leq -1.37$

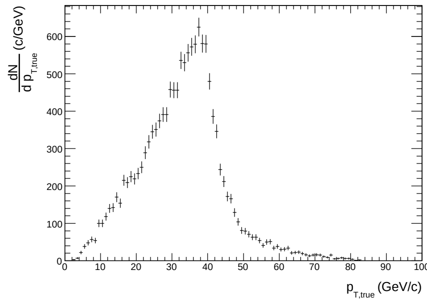

(c) $-1.37 \leq \eta \leq -0.8$

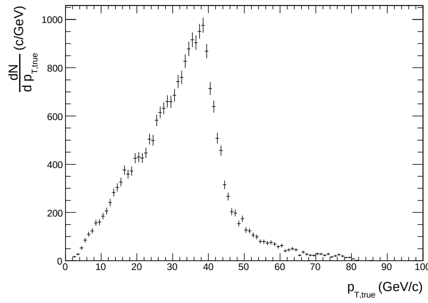

(d) $-0.8 \leq \eta \leq 0$

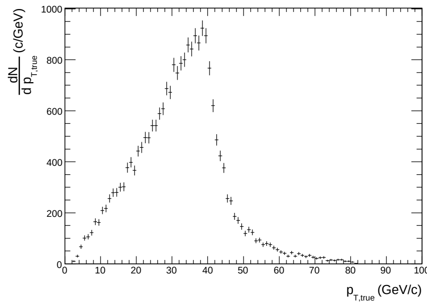

(e) $0 \leq \eta \leq 0.8$

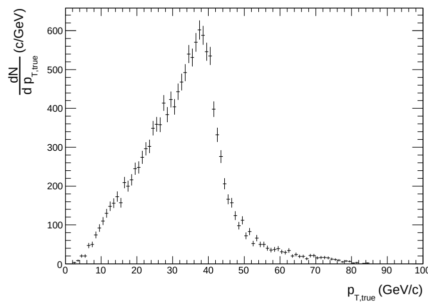

(f) $0.8 \leq \eta \leq 1.37$

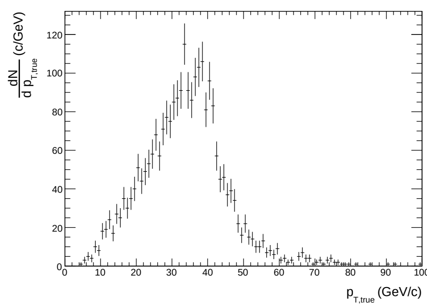

(g) $1.37 \leq \eta \leq 1.52$

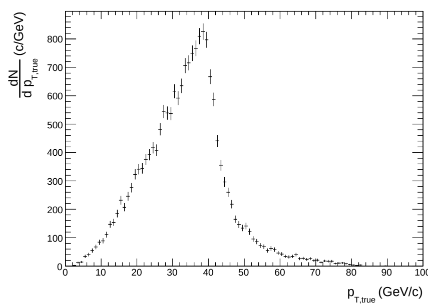

(h) $1.52 \leq \eta \leq 2.47$

Figure 7.1: The $p_{T,true}$ distributions for electrons from W$\rightarrow$eν decays for an integrated luminosity of $20\,\mathrm{pb}^{-1}$ for the different η bins.

7.2.4 J/ψ meson decays

J/ψ mesons decaying into two electrons, i.e $J/\psi \rightarrow e^+e^-$, have an approximately 50 times higher cross section than $Z \rightarrow e^+e^-$ decays. The main difference to the electrons from W and Z boson decays is that the electrons from $J/\psi \rightarrow e^+e^-$ decays have far lower p_T with a p_T spectrum peaking well below 10 GeV/c. This is a clear disadvantage since the performance of the electronmagnetic calorimeter is worse (due to the $\sigma_E/E_0 \sim a/\sqrt(E_0)$ dependance) for low p_T electrons and also less important since the electrons from most of the interesting physics processes to be studied, e.g. W boson, Z boson, top quarks or (perhaps) Higgs boson decays, have a far higher p_T.

7.2.5 Heavy flavour decays

The most luminous source of electrons are QCD processes, namely heavy flavour decays. Most of these electrons are inclusive electrons from b- and, to a lesser extent, from c-quark decays. The cross section for electrons from b-quark decays is expected to be $\sigma = 1.987\mu$b for a center of mass energy of 10 TeV. The main difference to the electrons from W and Z boson decays is that the electrons from heavy flaour decays have far lower p_T with a p_T spectrum peaking well below 10 GeV/c. This is a clear disadvantage since the performance of the electronmagnetic calorimeter is worse (due to the $\sigma_E/E_0 \sim a/\sqrt(E_0)$ dependance) for low p_T electrons and also less important since the electrons from most of the interesting physics processes to be studied, e.g. W boson, Z boson, top quarks or (perhaps) Higgs boson decays, have a far higher p_T. Furthermore the heavy flavour events tend to have many other particles close to the electron. Therefore the electrons are not isolated and this results in a systematic shift of the reconstructed cluster energy for the electron. This shift is on the level of 1% and still has to be understood [41].

7.3 Scale parameter extraction

The scale parameter is extracted for each η–φ bin and each true momentum distribution $t(p_{true}, \eta, \varphi)$ separately. The parameters $\hat{\tau}_e, \hat{E}_0, \hat{\sigma}_e$ are obtained by fitting the convolution model $E_\Sigma(e; \tau_e, E_0, \sigma_e)$ (equation 7.2) to the E/p_{true} distribution. The position of the peak of the E/p_{true} distribution is then given by $\hat{\mu} = \mu(\hat{\tau}_E, \hat{E}_0, \hat{\sigma}_E)$. The parameters $\hat{\alpha}_q, \hat{n}_q, \hat{\mu}_q, \hat{\sigma}_q$ are computed by fitting the mirror Crystall Ball parameterization $Q_\Sigma(q; \alpha_q, n_q, \mu_q, \sigma_q)$ (equation 7.4) to the p_{true}/p distribution. Then the scale parameter $\bar{\mu}_e$ for the E/p_{beam} distribution is calculated by fitting $R(r; \hat{\tau}_e, \bar{E}_0, \hat{\sigma}_e, \hat{\alpha}_q, \hat{n}_q, \hat{\mu}_q, \hat{\sigma}_q)$ (equation 7.13) to the E/p distribution. In this fit only the $\bar{E}_0$ parameter is allowed to vary.

The other parameters $\hat{\tau}_e, \hat{\sigma}_e, \hat{\alpha}_q, \hat{n}_q, \hat{\mu}_q, \hat{\sigma}_q$ are fixed to the values obtained by the E/p_{true} and p_{true}/p fits, respectively. The scale parameter $\bar{\mu}_e$ is given by $\bar{\mu}_e = \mu_e(\hat{\tau}_E, \bar{E}_0, \hat{\sigma}_E)$. The relative scale factor is then defined by the ratio $\bar{\mu}_e/\hat{\mu}_e$. Since the scale parameter $\hat{\mu}_e$ for the E/p_{beam} distribution was computed using the Monte Carlo simulation and therefore is assumed to be correct for the Monte Carlo simulation, the desired value for the extracted relative scale factor $\bar{\mu}_e/\hat{\mu}_e$ is 1.

This procedure is based on the assumption that the relative scale factor is close to 1 and therefore the effect of the scaling of the parameters $\hat{\tau}_e, \hat{\sigma}_e$ is negligible. Otherwise they would have to be scaled accordingly.

7.4 Scale parameter extraction for ATLAS Monte Carlo simulation

The geometrical acceptance region of the electromagnetic calorimeter ($|\eta| \leq$2.47) was divided into eight η bins. The η boundaries of the binning used in this analysis are -2.47, -1.52, -1.37, -0.8, 0., 0.8, 1.37, 1.52 and 2.47, corresponding to the central barrel ($|\eta| \leq$0.8), the extended barrel (0.8$\leq |\eta| \leq$1.37), the gap region (1.37$\leq |\eta| \leq$1.52) between barrel and endcap and the endcap (1.52$\leq |\eta| \leq$2.47). Each bin covers the whole φ range, i.e. $-\pi \leq \varphi \leq \pi$.

The scale parameter extraction procedure is first validated with a dedicated calibration sample consisting only of one electron per event with a momentum of 50 GeV/c. The relative scale factor $\bar{\mu_e}/\hat{\mu_e}$, expected to be 1, extracted from the E/p distributions without and with correlation weighting is shown in figure 7.2 as a function of η. This plot demonstrates that the modeling of the correlation between e and q brings the relative scale factor to 1 to within 5 ‰ for the gap region and to within 2 ‰ for the barrel and the endcap. Without the modeling of the correlation between e and q the deviation of the relative scale factor from 1 can be up to 3%. Even in the central barrel the deviation from 1 is systematically at +0.5%.

The relative scale factor $\bar{\mu}_e/\hat{\mu}_e$, expected to be 1, for electrons from W→eν decays is shown in figure 7.3 as a function of η for an integrated luminosity of 5, 10 and 20 pb^{-1}. The extracted values are compatible with 1 within the error bars. With an integrated luminosity of 20 pb^{-1} the relative scale factor can be computed with a precision of 2 permill for the barrel, with approximately 1% in the endcap and the gap region when the modeling of the correlation is used. The reason for the worse precision in the endcap

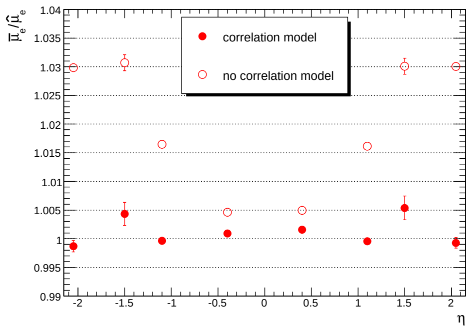

Figure 7.2: The relative scale factor $\bar{\mu}_e/\hat{\mu}_e$ extracted from the E/p distributions without and with correlation weighting for Monte Carlo simulation for 50 GeV/c electrons as a function of η.

and the gap region is the smaller number of electrons due to a lower reconstruction efficiency and a smaller bin size. With decreasing integrated luminosity and therefore statistics, this precision deteriorates for the gap region and the endcap with the extended barrel being affected to a lesser extent. This is due to the smaller bin size (gap region) and the lower reconstruction efficiency in these regions. The modeling of the correlation is indispensable for obtaining a relative scale factor within one percent to 1.

The parameter values obtained by the fits to the E/p_{true} and p_{true}/p distributions (section 7.3) are presented in figure 7.4 as a function of η for an integrated luminosity of $20\,\mathrm{pb}^{-1}$. The tail parameter $\hat{\tau}_e$ and the resolution parameter $\hat{\sigma}_e$ of the E/p_{true} distribution reflect the material distribution in the detector as a function of η. The same is true for the resolution parameter $\hat{\sigma}_q$ of the p_{true}/p distribution and the regime change parameter $\hat{\alpha}_q$ (more material means that the gaussian part of the Crystall Ball function is smaller and therefore $\hat{\alpha}_q$ is smaller). The scale parameter $\hat{E}_0$ of the E/p_{true} distribution has to compensate the effect of the tail and the resolution to bring the peak value to 1 in the ideal case. Since the understanding of the material effects is far less advanced in the crack region [37], the value of $\hat{E}_0$ in the crack region may not be optimal. The peak position $\hat{\mu}_q$ of the p_{true}/p distribution shows the shift of the peak due to more bremsstrahlungs activity in regions with more material in the Inner Detector. The power law parameter $\hat{n}_q$ of the p_{true}/p distribution is of less importance in general and therefore omitted.

In the previous plots the start value of E_0 for the fitting procedure was set to the value from the fit to the E/p_{true} distribution, $\hat{E}_0$. Therefore the knowledge of the relative

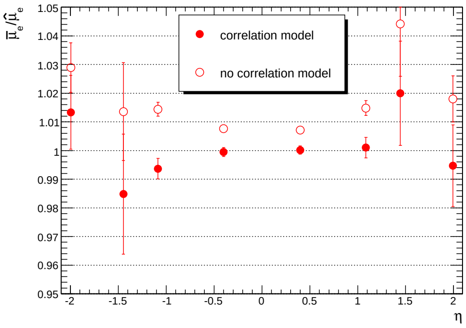

(a) $5\,\mathrm{pb}^{-1}$

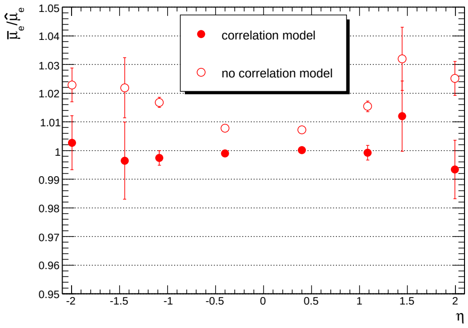

(b) $10\,\mathrm{pb}^{-1}$

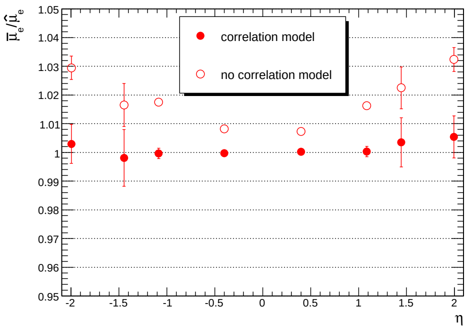

(c) $20\,\mathrm{pb}^{-1}$

Figure 7.3: The relative scale factor $\bar{\mu}_e/\hat{\mu}_e$ extracted from the E/p distributions with correlation weighting for Monte Carlo simulation for electrons from W$\rightarrow$eν decays as a function of η for an integrated luminosity of $5\,\mathrm{pb}^{-1}$, $10\,\mathrm{pb}^{-1}$ and $20\ \mathrm{pb}^{-1}$.

scale was indirectly injected. Furthermore the correlation distribution $C_\Sigma(e,q)$ gets adjusted to the correct $\hat{E}_0$ position. In order to test the robustness of the scale parameter extraction procedure a bias factor on the reconstructed energy E was artificially imposed for the E/p distribution. Figure 7.5 shows the relative scale factor $\bar{\mu}_e/\hat{\mu}_e$ as a function of η for an injected bias factor of $\pm 3\%$, $\pm 1\%$ und $\pm 0.5\%$ for an integrated luminosity of $20\ \mathrm{pb}^{-1}$. For a given injected bias factor λ the desired extracted relative scale factor is $1+\lambda$. Two effects are visible which interfere with each other. First, with increasing $|\lambda|$ the difference between the desired and the actual extracted relative scale factor becomes larger, up to 1-2% for $\lambda = \pm 3\%$. In addition, there is a tendency to overestimate λ. This tendency increases with $|\eta|$. Taking these two effects into account, the following iterative scheme for the extraction of the relative scale factor for each η–φ bin is employed

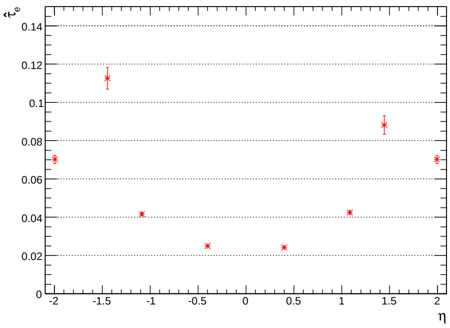

(a) $\hat{\tau}_e$

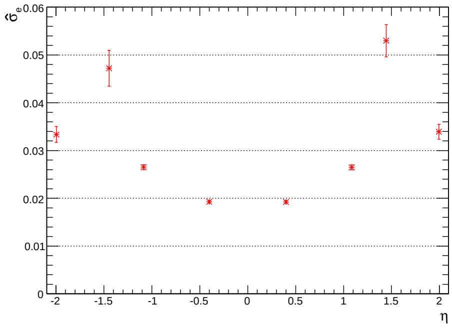

(b) $\hat{\sigma}_e$

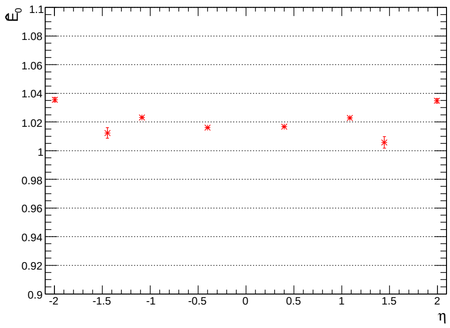

(c) $\hat{E}_0$

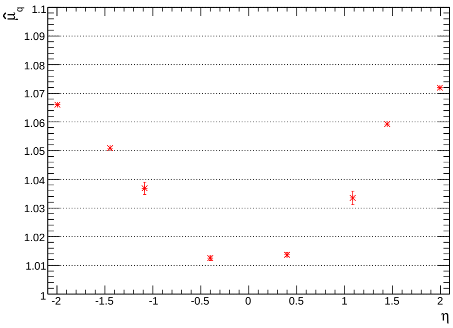

(d) $\hat{\mu}_q$

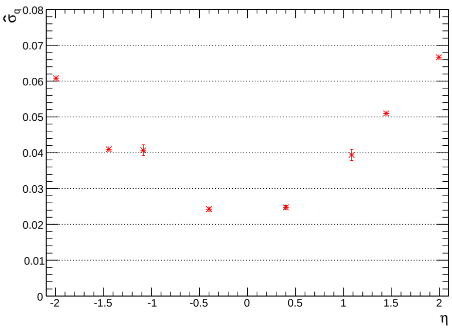

(e) $\hat{\sigma}_q$

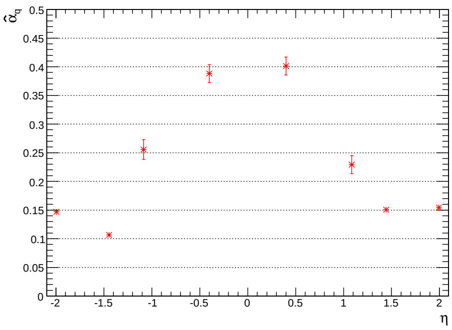

(f) $\hat{\alpha}_q$

Figure 7.4: Parameter values obtained by the fits to the E/p_{true} and p_{true}/p distributions for Monte Carlo simulation for electrons from W→eν decays as a function of η for an integrated luminosity of 20 pb^{-1}.

1. Compute $E^{i+1} = E^i\, \bar{\mu}_e^i/\hat{\mu}_e$ or start with $E^0 = E$ and $i = 0$,
2. Extract an estimate $\bar{\mu}_e^i/\hat{\mu}_e$ for the relative scale factor based on E^i,
3. Continue with point 1 unless the difference between the two consecutive $\bar{\mu}_e^i/\hat{\mu}_e$ values is smaller than a reasonable threshold, i.e. 0.1%.

The precision of the extracted scale factor for an injected/initial bias should be comparable to the one without initial bias (figure) after a few iterations provided that the initial bias is small, i.e. below 2-3% which is assumed to be the precision of the knowledge of the scale factor for the electromagnetic calorimeter based on test beam work.

7.4.1 Geometry with additional material

In order to evaluate the influence of the material description of the detector on the precision of the extracted relative scale factor, a dedicated geometry description of the ATLAS detector with additional material was used. The geometrical acceptance of the detector was divided in 8 regions (4 quadrants in φ and η positive/negative) and a different material configuration was used for each region. In the region $-\pi < \varphi < -\frac{\pi}{2}$ and $\eta < 0$ no material was added and therefore this corresponds to the nominal material description. The amount of material in radiation lengths in the Inner Detector and in front of the electromagnetic calorimeter is shown in figure 7.6 as a function of η. The most important additions are additional material in the Inner Detector in the upper hemisphere $\varphi > 0$ and additional material in the barrel cryostat upstream the calorimeter for $\eta > 0$. Especially for the sensitive layers of the Inner Detector these material additions are all much larger than the uncertainty but smaller increments would not be visible. A detailed description of this dedicated geometry is given in Appendix A.

For the geometry with additional material a Monte Carlo sample of electrons from W$\rightarrow$eν decays with an integrated luminosity of $13.5\,\mathrm{pb}^{-1}$ was used. Since the material description is different for the 8 regions, the η–φ binning is also modified accordingly. Using the bin boundaries in η like before, the φ range is additionally divided into 4 quadrants. Therefore the number of bins is increased by a factor of 4 reducing the available statistic for each bin also by a factor of 4. As a consequence there is an integrated luminosity of $3.4\,\mathrm{pb}^{-1}$ per quadrant.

As a first step the relative scale factor is extracted with correlation taken from the given η–φ bin. This assumes the knowledge of the different amounts of material. Later the

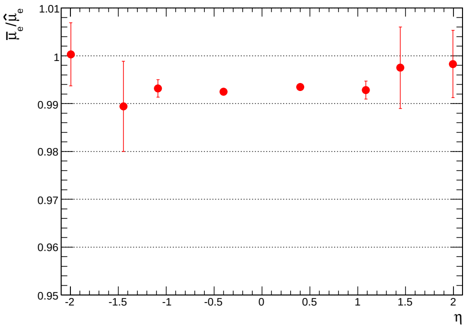

(a) -0.5%

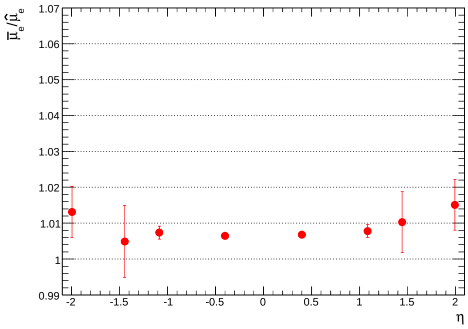

(b) 0.5%

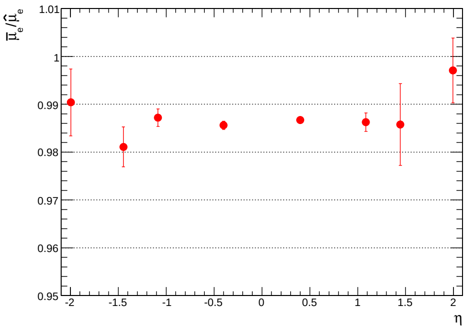

(c) -1%

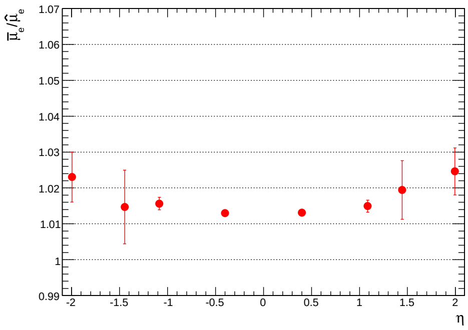

(d) 1%

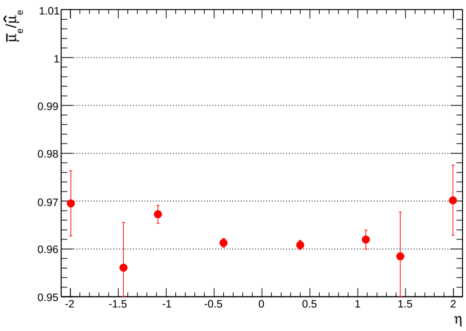

(e) -3%

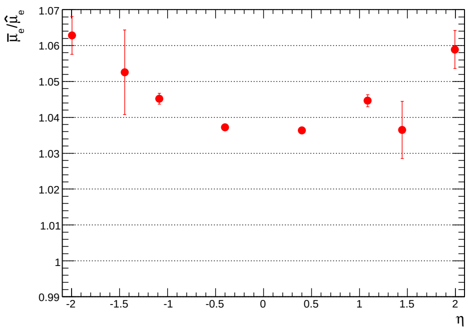

(f) 3%

Figure 7.5: The relative scale factor $\bar{\mu}_e/\hat{\mu}_e$ extracted from the E/p distributions with correlation weighting for Monte Carlo simulation for electrons from W$\rightarrow$eν decays as a function of η for an imposed scale factor of -0.5%, -1%, -3%, 0.5%, 1% and 3% for an integrated luminosity of $20\,\mathrm{pb}^{-1}$.

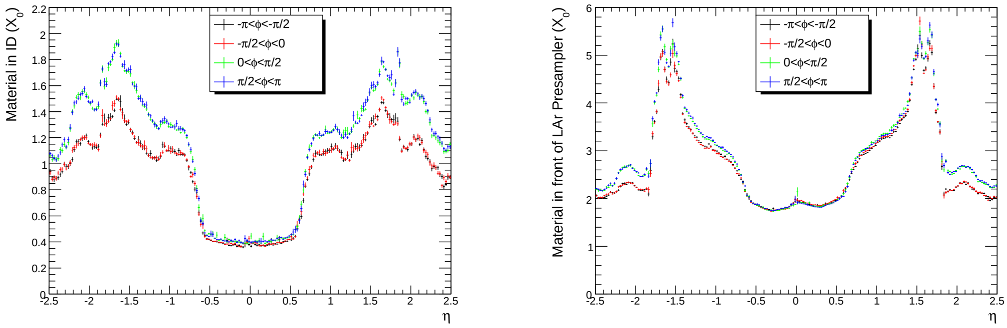

Figure 7.6: Amount of material in radiation lengths in the Inner Detector (left) and in front of the electromagnetic calorimeter (right) for all quadrants in φ as a function of η.

same exercise will be done without the prior exact knowledge of the material distribution. The relative scale factor $\bar{\mu}_e/\hat{\mu}_e$, expected to be 1, is shown in figure 7.7 for all 4 quadrants in φ as a function of η. The extracted values are compatible to 1 within errors. The obtained precision is well compatible with the precision of the nominal geometry with a comparable luminosity, i.e. figure 7.3(a). This means that the effect of the additional material is well recovered by the proper modeling of the correlation.

Finally, the relative scale factor is extracted with correlation taken from the η–φ bin corresponding to the nominal geometry at the same η position, i.e. from the region $-\pi < \varphi < -\frac{\pi}{2}$ and $\eta < 0$. The relative scale factor $\bar{\mu}_e/\hat{\mu}_e$, expected to be 1, extracted this way is shown in figure 7.8 for all 4 quadrants in φ as a function of η. Figure 7.8(b) demonstrates that the impact of additional material in the cryostat of the electromagnetic calorimeter on the precision of the extracted relative scale factor is very low because the increase of bremsstrahlung activity in the cryostat has no impact on the momentum measurement in the Inner Detector and therefore the correlation between e and q remains unaffected. On the other hand, additional material in the Inner Detector has a bigger impact (figures 7.8(c) and 7.8(d)), especially in the gap region and the endcap where more material had been added. However, these material additions in the Inner Detector are all much larger than the uncertainty of the knowledge of the corresponding material contributions.

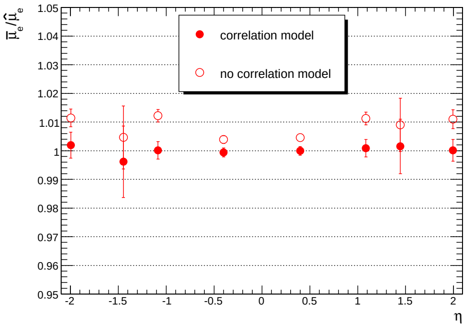

(a) $-\pi < \varphi < -\frac{\pi}{2}$

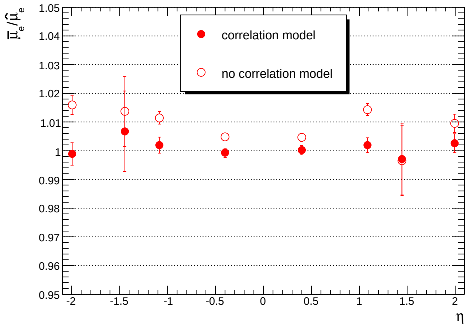

(b) $-\frac{\pi}{2} < \varphi < 0$

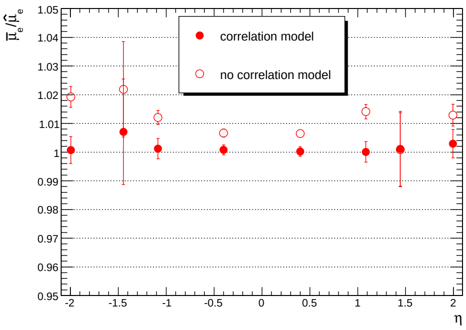

(c) $0 < \varphi < \frac{\pi}{2}$

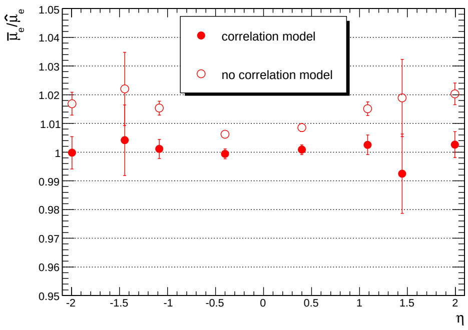

(d) $\frac{\pi}{2} < \varphi < \pi$

Figure 7.7: The relative scale factor $\bar{\mu}_e/\hat{\mu}_e$ extracted from the E/p distributions without and with correlation weighting for Monte Carlo simulation for electrons from W$\rightarrow$eν decays as a function of η. The correlation has been taken from the given bin. The four quadrants in φ are shown, $-\pi < \varphi < -\frac{\pi}{2}$ (top left), $-\frac{\pi}{2} < \varphi < 0$ (top right), $0 < \varphi < \frac{\pi}{2}$ (bottom left) and $\frac{\pi}{2} < \varphi < \pi$ (bottom right). The integrated luminosity is $3.4\,\mathrm{pb}^{-1}$ per quadrant.

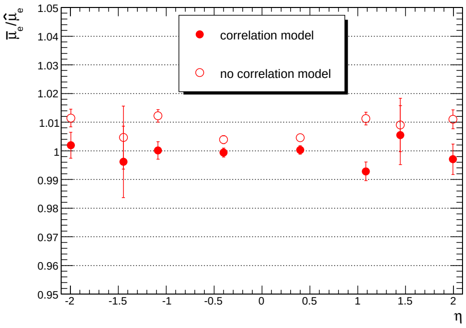

(a) $-\pi < \varphi < -\frac{\pi}{2}$

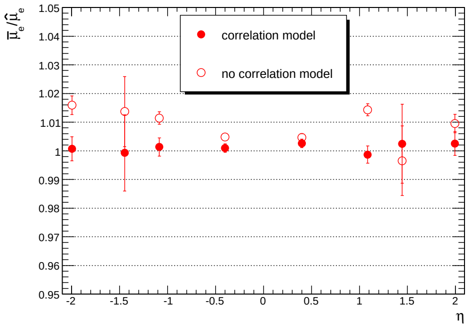

(b) $-\frac{\pi}{2} < \varphi < 0$

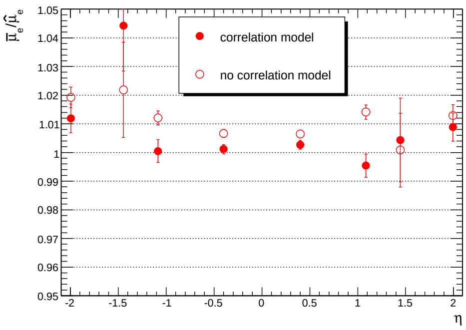

(c) $0 < \varphi < \frac{\pi}{2}$

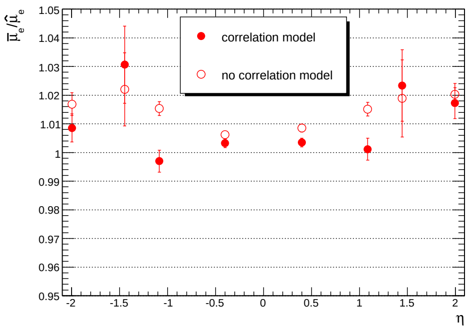

(d) $\frac{\pi}{2} < \varphi < \pi$

Figure 7.8: The relative scale factor $\bar{\mu}_e/\hat{\mu}_e$ extracted from the E/p distributions without and with correlation weighting for Monte Carlo simulation for electrons from $W \rightarrow e\nu$ decays as a function of η. The correlation has been taken from the corresponding bin in the octant $-\pi < \varphi < -\frac{\pi}{2}$, $\eta < 0$. The four quadrants in φ are shown, $-\pi < \varphi < -\frac{\pi}{2}$ (top left), $-\frac{\pi}{2} < \varphi < 0$ (top right), $0 < \varphi < \frac{\pi}{2}$ (bottom left) and $\frac{\pi}{2} < \varphi < \pi$ (bottom right). The integrated luminosity is $3.4\,\mathrm{pb}^{-1}$ per quadrant.

7.5 Summary

In this chapter the procedure to extract the relative scale between the electromagnetic calorimeter and the Inner Detector using a parameterization of the E/p distribution developed for the combined test beam 2004 (chapter 6), has been applied to Monte Carlo simulation for ATLAS.

After the description of the modeling of the E/p distribution with an emphasis on the differences with respect to the combined test beam 2004, the various physics processes that could provide electrons with a sufficient rate have been discussed and W boson decays into an electron and a neutrino, i.e. W→eν, have been idenified as the most performant process for this intercalibration method.

By employing an iterative scheme, I have shown that the relative scale factor $\bar{\mu_e}/\hat{\mu_e}$ extracted from the E/p distributions for electrons from W→eν decays is always compatible with 1 within errors using the nominal material description in the Monte Carlo simulation. Different variations of the material description have been used to evaluate the systematic errors arising from an imperfect material description in the Monte Carlo simulation. For the realistic variations the relative scale factor $\bar{\mu_e}/\hat{\mu_e}$ is still compatible with 1 within errors. A dedicated Monte Carlo simulation shows that the systematic error due to the fitting procedure is at the 1‰level.

As a consequence, I have shown that the intercalibration method allows the calibration of the absolute energy scale of the electromagnetic calorimeter with an integrated luminosity of 20 pb^{-1} at the level of a few ‰ including the systematic uncertainties arising from the description of the material upstream of the electromagnetic calorimeter and the parameter extraction procedure.

8 The ATLAS calibration strategy for electrons with early LHC collision data

This chapter outlines the current strategy for the electron calibration with early LHC collisions data. Section 8.1 presents the inputs for the calibration of electrons and discusses their status. Section 8.2 presents the goals that have to be met for the electron calibration. Different methods that can be used to improve the electron calibration are presented in section 8.3 and, finally, section 8.4 shows how these different methods will be combined to achieve the goals set for the electron calibration.

8.1 Inputs

The energy measurement of electrons will be calibrated using a dedicated variant of the Calibration Hits Method [37] that was presented for the combined test beam 2004 in section 5.7. The required inputs for this method are:

Monte Carlo simulation The Monte Carlo simulation is used to estimate the various, not directly measured energy deposits in the detector. In order to make sure that the extrapolation of the estimates for these energy deposits to the ATLAS detector is correct, the material description of the detector in the Monte Carlo simulation must be accurate on the $\leq$1% level. Presently, this level of understanding of the material distribution is clearly not reached and is rather at the $\leq$5% level.

Absolute energy scale Since the absolute scale of the energy is a free parameter, it has to be set by known physics processes such as $Z \rightarrow e^+e^-$ decays or by intercalibration with the Inner Detector using E/p. Furthermore, the energy scale can vary from module to module. The uniformity of the energy scale was investigated with cosmic muons measured during the commissioning phase of the ATLAS detector and in such a way probed at the 1% level.

Concerning the Inner Detector the required inputs are:

Magnetic field map The magnetic field in the Inner Detector has been measured during a dedicated precision measurement campaign [38, 42, 43]. The resulting field residuals were less than 0.5 mT, and the systematic error on the measurement of track sagitta due to the field uncertainty was estimated to range from $2{\cdot}10^{-4}$ to $12{\cdot}10^{-4}$, depending on the tack rapidity.

Alignment of the various Inner Detector components An initial alignment of the Inner Detector components was done with cosmic muons. Since cosmic muons predominantly come in the vertical direction many alignment constants of the Inner Detector could not be adjusted using cosmic muons and therefore have to be corrected using collision particle tracks.

8.2 Goals

Energy scale

The electromagnetic energy scale is known from test beams to a precision of 2-3% over wide range of energies (10 GeV to 280 GeV). The uncertainties are coming from the imperfect knowledge of the temperature of the liquid argon in the test beams and of the pulse shape. The electromagnetic energy scale at lower energies (0.5 GeV to 10 GeV) is also important for jets. The goal is to establish the electromagnetic energy scale with better than 1% accuracy with an integrated luminosity of $10\,\mathrm{pb}^{-1}$ using the Z mass peak together with $Z\to e^+e^-$ decays as well as the E/p distribution for electrons from W boson decays.

Linearity

Based on test beam measurements the electromagnetic calorimeter is known to be linear to 0.2% over the high energy range and 0.5% over the 1-10 GeV range. The goal is to verify the linearity with a precision better than 1% over the full eta range by studying the electrons from J/ψ, Υ and Z decays with an integrated luminosity of 10-100 pb^{-1}.

Electromagnetic calorimeter modul–to–modul cross-calibration

The energy scale spread between modules of the electromagnetic calorimeter is predicted to be around 7‰ [44]. The goal is to measure to better than 0.5% using the E/p distribution and $Z\to e^+e^-$ decays by the end of 2010. For this measurement it is important to know the material distribution in the detector quite well. The strategy will evolve from uniformity in φ using the energy flow in minimum bias events at the beginning, later switching to $J/\psi \to e^+e^-$ decays and the E/p distribution for electrons coming from heavy flavour decays and ultimately $Z \to e^+e^-$ decays as well as the E/p distribution for electrons from W boson decays for an integrated luminosity of $200\,\mathrm{pb}^{-1}$.

Resolution

The goal is to derive the full response function of the electromagnetic calorimeter. This will be done with $Z \to e^+e^-$ decays as a function of η with an integrated luminosity of $200\,\mathrm{pb}^{-1}$.

Alignment of Inner Detector and the electromagnetic calorimeter

Although some indications of the alignment of the Inner Detector and the electromagnetic calorimeter were obtained from cosmic muons measurements during the commissioning phase of the ATLAS detector, the goal is to establish the alignment to a precision of 0.2 mm with an integrated luminosity of a few pb^{-1} using electrons from heavy flavour decays.

Material mapping in front of EM calorimeter

The material distribution in the detector is known from construction drawings and the weighing of the various detector parts to a few percent of a radiation length. The goal is to map the material distribution with data to 5% of a radiation length by summer 2010 and to 1-2% of a radiation length by end 2010. This will be done using photon conversions and mix of other sensitive but less direct methods, e.g. longitudinal shower shapes and studies of the tail parameter extracted from the E/p distribution.

8.3 Methods

8.3.1 Energy scale determination using $Z \to e^+e^-$

The mass of the Z boson is very precisely known from the experiments at LEP to be $91.1876 \pm 0.0021\,\mathrm{GeV/c^2}$. Furthermore the full functional form of the Z boson line shape is also well known. Therefore $Z \to e^+e^-$ decays can be used to determine the energy scale of the electromagnetic calorimeter. The procedure for ATLAS is documented in [45]. The basic idea is to split the geometrical coverage of the detector into regions, assign a scale factor to each region and then to minimize the difference of the expected Z boson line shape and the measured Z boson line shape wrt. the scale parameters. For the expected Z boson line shape the full response function of the electromagnetic calorimeter including the tails is modeled instead of using a simple gaussian.

Z boson line shape modeling

The true line shape for the Z boson is modeled with a Breit–Wigner function

$$BW(M) = \frac{\Gamma_Z^2\, M^2/M_Z^2}{\left(M^2 - M_Z^2\right)^2 + \Gamma_Z^2\, M^4/M_Z^2}, \tag{8.1}$$

where M_Z is the mass and Γ_Z is the decay width of the Z boson.

In order to correct for small deviations from the Breit-Wigner line shape due to subtile effects in proton–proton collisions a parton luminosity term $\mathcal{L}(M)$

$$\mathcal{L}(M) = M^{-\beta} \tag{8.2}$$

is mulitplied with the Breit–Wigner function and fitted to the Z boson mass distribution, obtained with events generated with PYTHIA. The resulting value is $\beta = 1.60 \pm 0.01$.

Inspired by the modeling of E/p_{beam} for the combined test beam 2004 (section 6.1.2) the parameterization for the calorimeter response is derived as a gaussian convoluted with an exponential tail which yields

$$R(x, \sigma, \lambda) = N(\sigma, \lambda) \int_{-\infty}^{b(\sigma,\lambda)} e^{\lambda\, t}\, e^{-\frac{(t-x)^2}{2\,\sigma^2}}\, dt, \tag{8.3}$$

where $x = M/M_Z - 1$ and the parameters $N(\sigma, \lambda)$ and $b(\sigma, \lambda)$ are chosen such that $R(x, \sigma, \lambda)$ is a probability density function, i.e. its integral is equal to 1, and the most probable value is at $x = 0$.

Combining equation 8.1, equation 8.2 and equation 8.3, the expected measured Z boson mass line shape is given by

$$L(M) = \int_{-\infty}^{\infty} BW(u)\, \mathcal{L}(u)\, R(M - u)\, du. \tag{8.4}$$

Paramter fitting method

The geometrical coverage of the calorimeter is divided into 896 regions. The barrel part ($|\eta| < 1.4$) is divided into regions of $\Delta\eta \times \Delta\varphi = 0.2 \times 0.2$. The endcap part ($|\eta| > 1.4$) is divided with a granularity of 0.2 in φ and with η boundaries of 1.4, 1.5, 1.6, 1.8, 2.0, 2.1, 2.3 and 2.5. For each region, index by i, a scale factor $1+\alpha_i$ is introduced to compensate a possible miscalibration of the reconstructed electron energy, i.e.

$$E_i^{calib} = E_i^{reco}\,(1 + \alpha_i). \tag{8.5}$$

The di–electron invariant mass for an event, where one electron is measured in region i and the other one in region j, is approximated as

$$M_{ij} = M_{ij}^{reco}\left(1 + \frac{\alpha_i + \alpha_j}{2}\right). \tag{8.6}$$

The standard procedure to determine the 896 coefficients α_i is to minimize the following log-likelihood function

$$-\ln L_{tot} = \sum_{k=1}^{N} -\ln L\left(\frac{M_k}{1 + \frac{\alpha_{i(k)}+\alpha_{j(k)}}{2}}\right), \tag{8.7}$$

where L is given by equation 8.4, N is the total number of events, $i(k)$ and $j(k)$ denote the two regions where the electrons are detected for a given event k and $M_k = M_{i(k)j(k)}$ is the di–elctron invariant mass for a given event k.

Since the solving of the full minimization problem (equation 8.7) is very time consuming, a faster method, denoted *iterative method* has been developed. A region i is selected and the coefficient α_i is computed under the assumption that all other regions are perfectly calibrated, i.e. $a_j = 0\ \forall j \neq i$. Therefore the function to be minimized is

$$-\ln L_{iter} = \sum_{k=1}^{N_i} -\ln L\left(\frac{M_k}{1 + \frac{\alpha_i}{2}}\right) \tag{8.8}$$

where k runs over all events with an electron in region i, L is given by equation 8.4 and $M_k = M_{i\,j(k)}$ is the di–electron invariant mass for the given event k.

For a single iteration step the minimization of equation 8.8 is done consecutively for all regions of the calorimeter, i.e for all indices i. The iteration procedure typically converges, i.e. $|\alpha_i^{l+1} - \alpha_i^{l}| < 0.1\%\ \forall i$, after 5 iterations.

Performance

The performance of the Z$\rightarrow$e$^+$e$^-$ energy scale determination method was evaluated with a Monte Carlo simulation where miscalibration was simulated by injecting random scale biases α_i^{bias} into all regions of the calorimeter. Then the iterative procedure (equation 8.8) was used to compute α_i^{calib} in order to recover these miscalibrations. The residual distributions $\alpha_i^{calib} - \alpha_i^{bias}$, $\forall i$ were fitted with a gaussian and the σ of this gaussian is shown in figure 8.1 as a function of the integrated luminosity. For an integrated luminosity of 100 pb^{-1} the expected resolution is 0.5% for the barrel part of the calorimeter.

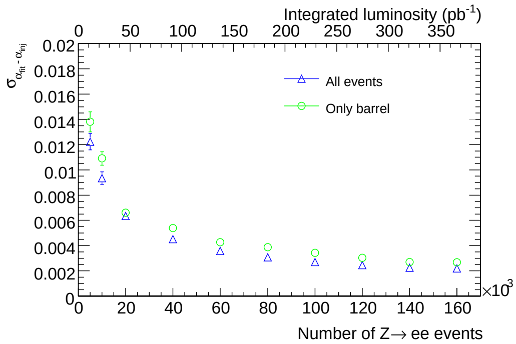

Figure 8.1: Width of a gaussian fitted to the residual distribution $\alpha_i^{calib} - \alpha_i^{bias}$ for the barrel part of the electromagnetic calorimeter ($|\eta| < 1.4$) as a function of the number of events or the integrated luminosity. These residuals are shown for all events (triangles) or for all events where both electrons are measured in the barrel (circles). [45]

The Z mass line shape before and after the corrections for the injected bias is shown in figure 8.2 for the geometry with additional material to test the impact of the material description on the energy scale. The shift due to the additional material is recovered very well, at the level of 1 permill. However, the impact of additional material on the reconstructed energy cannot be corrected for by a scale factor, but needs to be included in the computation of the weights of the Calibration Hits Method.

The systematic uncertainty is estimated to be at approximately 0.2%. at the energy corresponding to the Z boson mass. At other energy scales, the effects of the material description dominate the systematic uncertainty. Extrapolating to the full p_T spectrum for the central part of the barrel ($|\eta| < 0.6$) yields an uncertainty of 0.5%. For the non–central part of the detector these effects increase to 1-2% except for the gap region where they are even larger [45].

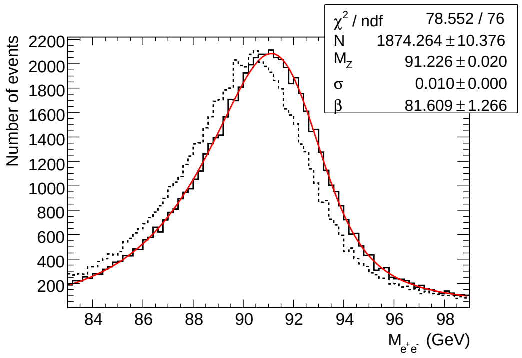

(a) without additional bias

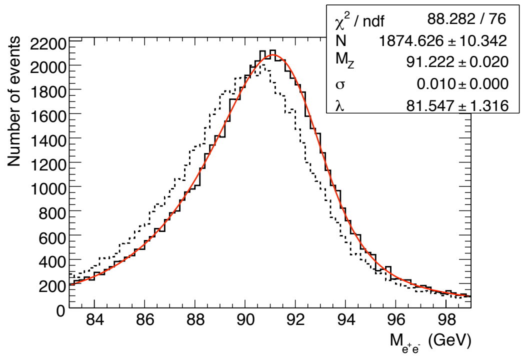

(b) with additional bias

Figure 8.2: Distribution of the di–electron invariant mass for electrons ($|\eta| < 1.4$ or $1.8 < |\eta| < 2.5$) before (dashed) and after (solid) corrections for the geometry with additional material without and with additional random scale bias to simulate miscalibration. [45]

8.3.2 Energy scale determination using E/p

A method for the energy scale determination using the momentum measurement and the E/p distribution for electrons from W boson decays has been presented in the previous chapter 7.

In additional to electrons from W boson decays, an effort to understand the impact of the underlying event for the E/p distributions for electrons coming from heavy flavour decays has been ramping up.

With a large integrated luminosity, high p_T electrons from top quark decays can be used to probe the linearity of the electromagnetic calorimeter up to several hundred GeV.

8.3.3 Material mapping using photon conversions

For photons with an energy measurable in ATLAS, i.e. above 1 GeV, the cross section for converting into an electron–positron pair is almost independent of the photon's energy and is given by

$$\sigma = \frac{7\,A}{9\,X_0\,N_A}. \tag{8.9}$$

Due to the stochastic nature of this process the probability that a photon converts while passing a layer of material with thickness d is given by

$$p(d) = 1 - e^{-\frac{7}{9}\frac{d}{X_0}}. \tag{8.10}$$

Therefore by measuring the conversion probability in a given layer of material, its thickness can be calculated.

A method to reconstruct photon conversions has been developed for the combined test beam 2004 [46]. The basic idea is that the tracks of an electron–positron pair which is produced in the conversion are measured by the Inner Detector and their intersection vertex is used to determine the position of the conversion. During dedicated runs of the combined test beam 2004 an additional copper foil with a thickness is 37μm was placed upstream of the pixel detector. Figure 8.3 shows the results obtained with the CTB 2004 Monte Carlo simulation of the difference of the reconstructed conversion vertex position and the true conversion vertex position taken from the Monte Carlo simulation. The

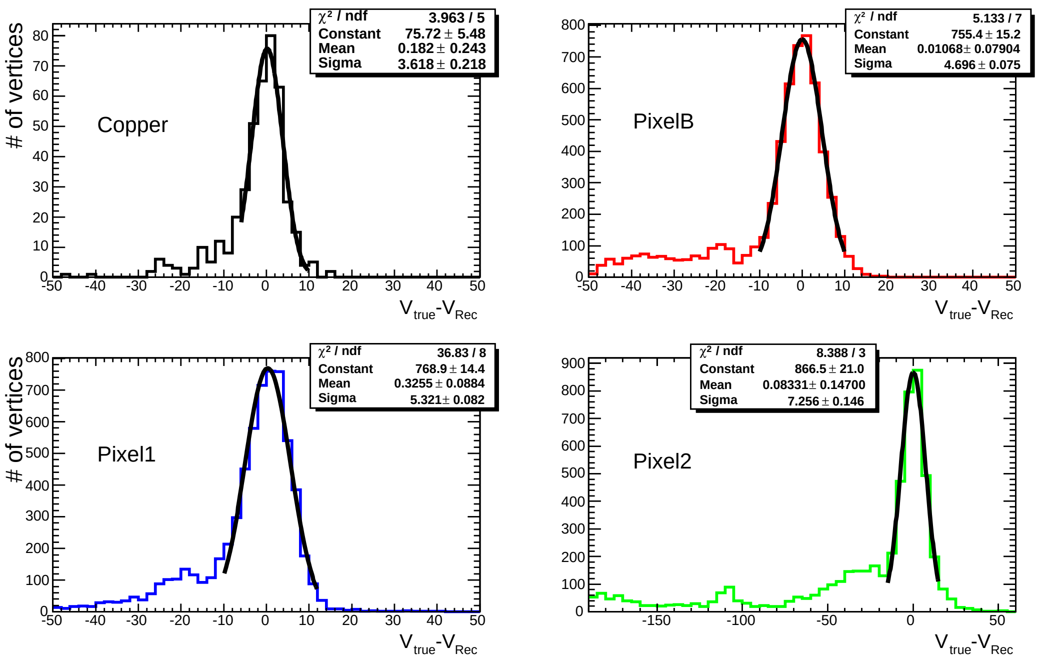

Figure 8.3: Difference (in mm) of the reconstructed conversion vertex position and the true conversion vertex position for the CTB 2004 Monte Carlo simulation.

resolution is 3.6, 4.7, 5.3 and 7.3 mm for the copper and the Pixel three layers. Since the clearances between the layers for Pixel Detector and the SCT are about 35 mm and

70 mm, the obtained resolution is good enough to observe the structure of the detector layers.

The Monte Carlo simulation to data comparison for the combined test beam 2004 is shown for the photon conversions in the copper foil in figure 8.4 and the Inner Detector in figure 8.5.

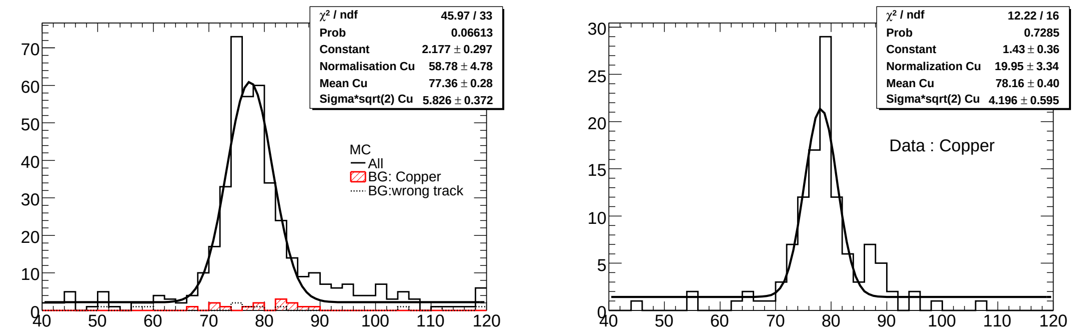

(a) Monte Carlo simulation (b) Data

Figure 8.4: Reconstructed conversion vertex distribution (in mm) for the copper foil for Monte Carlo simulation and CTB 2004 data.

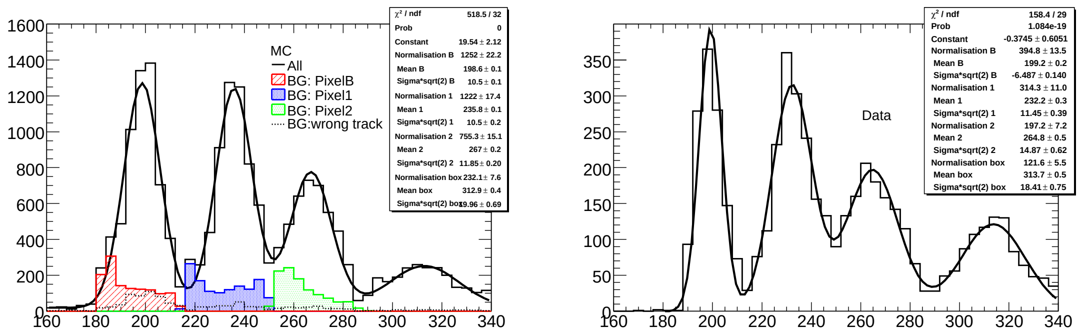

(a) Monte Carlo simulation (b) Data

Figure 8.5: Reconstructed conversion vertex distribution (in mm) for the active layers of the Inner Detector for Monte Carlo simulation and CTB 2004 data.

For ATLAS the same algorithm will be used to map the material distribution [5]. Photons coming from minimum bias events will be so abundant that right from the LHC startup there will be enough statistics available so that the performance of this method will be dominated by its systematic errors. The number of reconstructed photon conversions $N_C(R)$ for a given material layer R is given by

$$N_C(R) = N(R)p(R)\epsilon(R) \tag{8.11}$$

where $N(R)$ is total number of photons passing the layer, $p(R)$ is the conversion probability from equation 8.10 and $\epsilon(R)$ is the reconstruction efficiency of the photon conversions that occur in the given layer. Since the total number of photons, i.e. the photon flux, will be basically unknown, equation 8.11 is normalized to the number of photons $N_C(BP)$ converting in the geometrically corresponding ($N(R) = N(BP)$) part of the beam pipe. The reason for this normalization is that the material distribution in the beam pipe, i.e. $p(BP)$, is very well known.

$$\frac{N_C(R)}{N_C(BP)} = \frac{N(R)\,p(R)\,\epsilon(R)}{N(BP)\,p(BP)\,\epsilon(BP)} = \frac{p(R)\,\epsilon(R)}{p(BP)\,\epsilon(BP)} \tag{8.12}$$

Transforming this to express the desired quantity $p(R)$ yields

$$p(R) = \frac{N_C(R)\,p(BP)\,\epsilon(BP)}{N_C(BP)\,\epsilon(R)}. \tag{8.13}$$

The quantities $N_C(R)$ and $N_C(BP)$ will be measured. The reconstruction efficiency for photon conversions in the beam pipe $\epsilon(BP)$ will be extracted from Monte Carlo simulation and the probability for conversions in the beam pipe $p(BP)$ is well known from the material description. Therefore the most difficult part will be to determine the reconstruction efficiency for photon conversions in the given layer $\epsilon(R)$ which will dominate the systematic error. One method under investigation to accomplish this is to use also the Pixel support tube surrounding the Pixel detector as a second normalization layer in addition to the beam pipe. It is made out of carbon and its material distribution is also very well known.

The expected mapping of the material distribution in the Inner Detector is plotted in figure 8.6 based on 500,000 minimum bias events.

8.3.4 Material mapping using the shower shape

The impact of the material distribution in front of the electromagnetic calorimeter on the shower shape is well known from the combined test beam 2004 [14]. Several material sensitive measurement variables were studied, i.e. the energy deposited in the strips layer

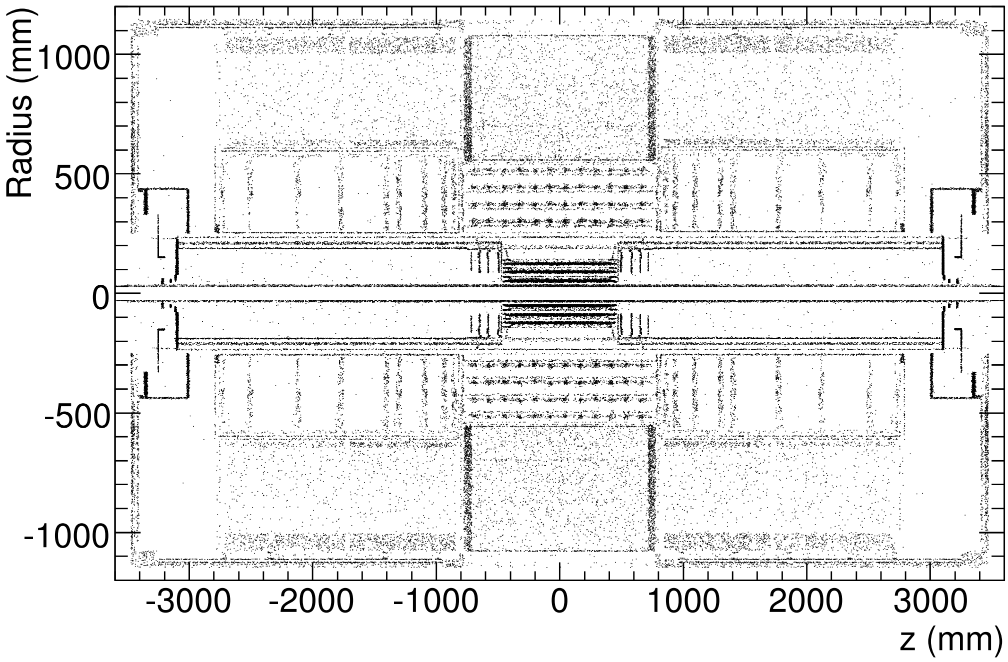

Figure 8.6: Mapping of photon conversions as a function of z and radius, integrated over φ, for the Inner Detector. The mapping has been made from 500,000 minimum bias events, using 90,000 conversion electrons of $p_T > 0.5$ GeV/c originating from photons from pi$^0/\eta$ decays. Taken from [5].

relative to the total visible energy or the lateral shower shape measured by the energy distribution in the strip layer in η direction.

In ATLAS, high p_T electrons (p_T >15 GeV/c) coming from W decays can be used to determine the amount of material in various locations [47]. In figure 8.7 the impact of additional material equivalent to 7% of a radiation length between the presampler and the strips layer on the relative energy deposit in the strip layer and on the lateral shower width measured as the η width of the shower in the strip layer is shown using 2.5 million events. In figure 8.8 the impact of additional material equivalent to 15% of a radiation length in the cryostat on the relative energy deposit in the presampler layer, on the relative energy deposit in the strip layer, on the relative energy fraction of the strip layer outside a core of 3 strips and on the lateral shower width measured as the η width of the shower in the strip layer is shown using 2.5 million events. Using these variables the material in front of the calorimeter can be identified to the level of a few percent of a radiation length. If differences in the shower shape variables between the Monte

Carlo simulation and the data are observed for a certain region, the determination of the position along the particle tracks in this region, where the material description in the Monte Carlo simulation has to be modified, will be highly nontrivial and will have to be cross–checked with the other presented methods.

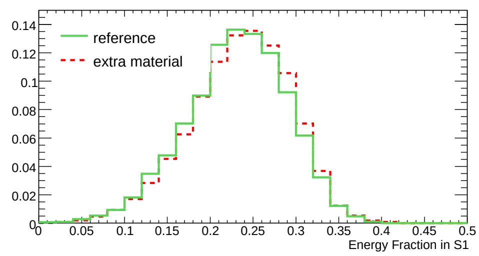

(a) Relative energy in the strip layer

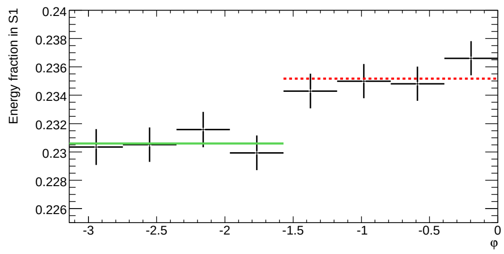

(b) Profile of the relative energy in the strip layer versus φ

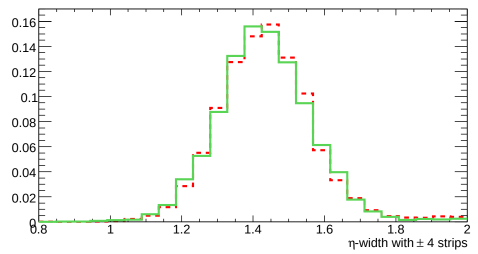

(c) η–width in the 9 ($\pm$4+1) strips around the strip energy maximum

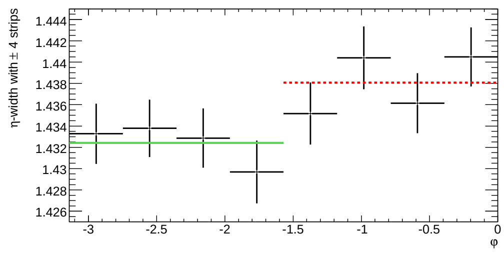

(d) Profile of the η–width in the 9 ($\pm$4+1) strips around the strip energy maximum versus φ

Figure 8.7: Distribution and profile versus φ for different material sensitive measurement variables without (solid reference) and with (dashed) additional material between the presampler and the strips layer.

8.3.5 Material mapping using E/p

Percentage of events in the tail of the E/p distribution

Detailed Monte Carlo simulation studies have revealed that the tail of the E/p distribution (E/p >2.0) is mainly populated by electrons, having emitted bremsstrahlung in the pixel detector. The idea is therefore to correlate the fraction of the number of events in the tail of the E/p distribution with the total material in the pixel detector [48].

Figure 8.9 shows the fraction of events in the tail of the E/p distribution (E/p >2.0) for electrons coming from heavy flavour (red circles) decays and the amount of material in

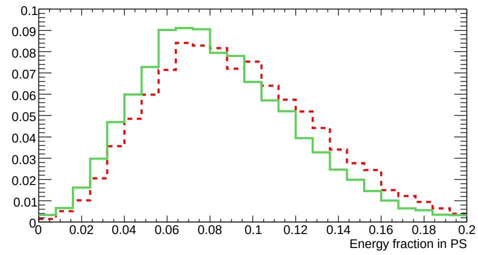

(a) Relative energy in the presampler layer

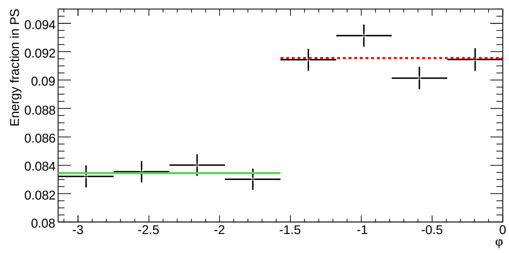

(b) Profile of the relative energy in the presampler layer versus φ

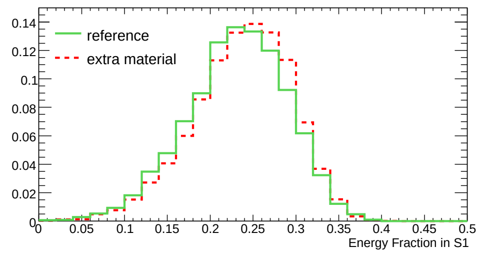

(c) Relative energy in the strip layer

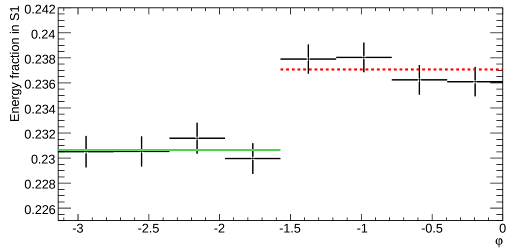

(d) Profile of the relative energy in the strip layer versus φ

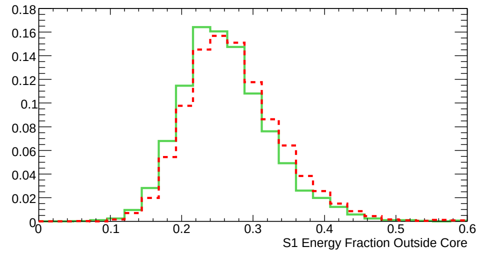

(e) Relative energy fraction of the strip layer outside a core of 3($\pm$1+1) strips around the strip energy maximum

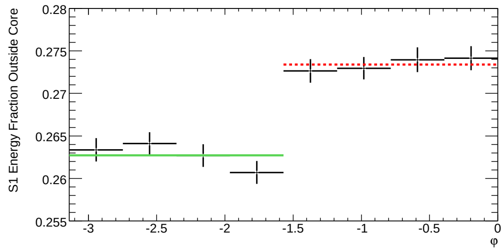

(f) Profile of the relative energy fraction of the strip layer outside a core of 3($\pm$1+1) strips around the strip energy maximum versus φ

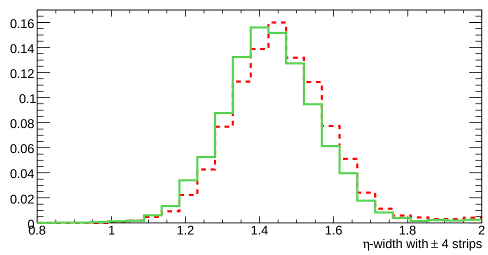

(g) η–width in the 9 ($\pm$4+1) strips around the strip energy maximum

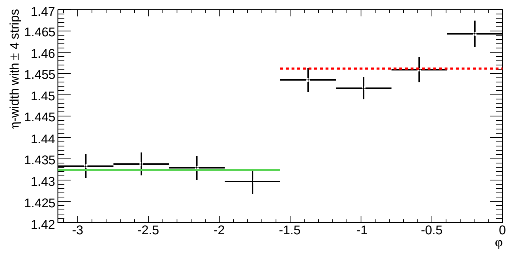

(h) Profile of the η–width in the 9 ($\pm$4+1) strips around the strip energy maximum versus φ

Figure 8.8: Distribution and profile versus φ for different material sensitive measurement variables without (solid reference) and with (dashed) additional material in the cryostat.

the Pixel detector (lines) as a function of η. The fraction of tail events tracks the amount of material in the pixel detector; however, the correlation still has to be quantified.

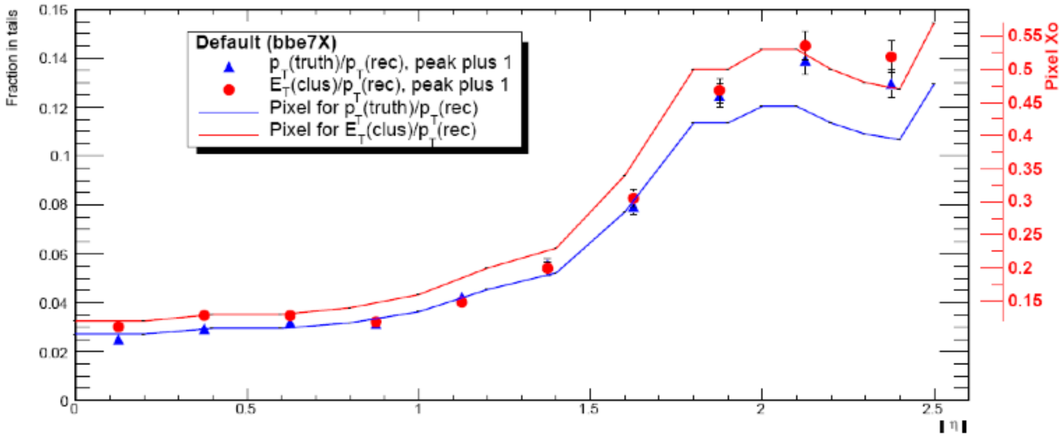

Figure 8.9: The fraction of events in the tail of the E/p distribution (E/p >2.0) for electrons coming from heavy flavour (red circles) decays and the amount of material in the Pixel detector (lines) as a function of η. On the right the axis for the amount of material in the Pixel detector is added.

Fitting the tail of the E/p distribution

Using the modeling and fitting procedure described in chapter 7 the tail parameter τ_e (equation 7.1) of the response function of the electromagnetic calorimeter can be determined from the E/p distribution [49]. The tail parameter obtained from the E/p distribution as well as the ratio of the tail parameter obtained from the E/p distribution and the tail parameter obtained from the E/p_{true} distribution are presented in figure 8.10 for an integrated luminosity of 24 pb^{-1} as a function of η. The precision is at the level of 10-20% and still dominated by statistics.

Using the nominal material description and the geometry with additional material in the Monte Carlo simulation the tail parameter τ_e obtained from the E/p distribution can be correlated with the amount of material in front of the calorimeter at a given η position. In figure 8.11 this correlation is plotted and modeled with an exponential curve. For an integrated luminosity of 24 pb^{-1} and taking the correlation between the fit parameters of the exponential model into account, the precision on the amount of material in front of the calorimeter is 8.8% of a radiation length. Extrapolating these results to an integrated luminosity of 100 pb^{-1} the amount of material in front of the

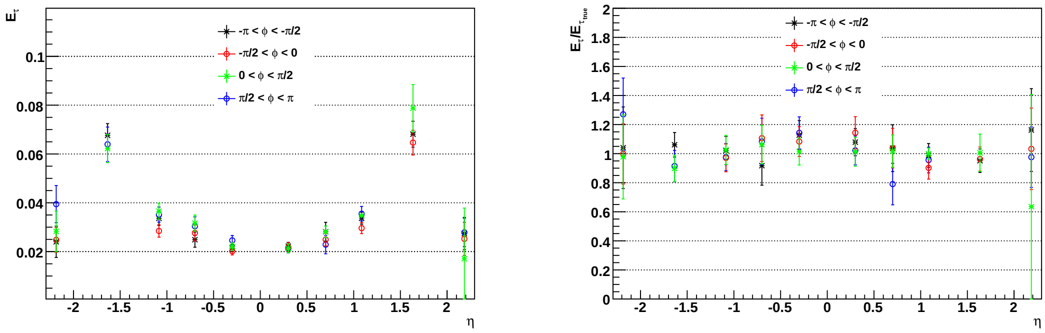

(a) E_T from the E/p distribution

(b) Ratio of E_T from E/p and E/p_{true} distributions

Figure 8.10: The tail parameter, denoted E_T, obtained from the E/p distribution and the ratio of the tail parameter obtained from the E/p distribution and the tail parameter obtained from the E/p_{true} distribution as a function of η.

calorimeter can be determined with a precision of approximately 5% of a radiation length.

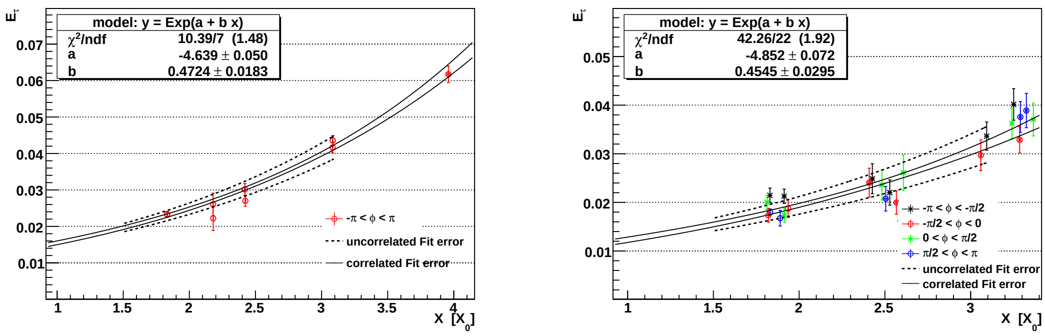

(a) Nominal material description

(b) Geometry with additional material

Figure 8.11: The tail parameter, denoted E_T, of as a function of the amount of material in front of the calorimeter.

8.4 Combined strategy

The calibration of electrons with the Calibration Hits methods for each η–φ bin relies on the accurate material description in the Monte Carlo simulation and on the energy scale. These two ingredients are not independent from each other, e.g. more material in the real detector than in the Monte Carlo simulation changes the position of the peak of the response function of the electromagnetic calorimeter. Furthermore, the scale will be set at low energy (3 GeV) by the J/ψ and at medium energy (40-50 GeV) by the Z boson mass peak and by W boson decays. The impact of the material description on the extrapolation from these energies to the whole energy spectrum also has to be taken into account. The challenge will be to disentangle material effects from the calibration of the energy scale and not to compensate material effects by applying scale factors for different detector regions.

Starting with a coarse η–φ binning and gradually refining it, the calibration will be performed in several iterations which involve the following steps for each η–φ bin:

1. Idenify discrepancies in sensitive measurement variables between the Monte Carlo simulation and the data with the methods presented in section 8.3.
2. Derive a better estimate of the material description and the electron energy scale parameter.
3. Rerun the Monte Carlo simulation with the updated material description and electron energy scale parameter, derive the new calibration constants and perform the Monte Carlo simulation to data comparison again.

The very details of the iteration process are still under discussion.

In the long term, the precision of the energy measurement of electrons for the various parts of the energy spectrum will be driven by the needs of the physics program of ATLAS. For example, the material description that is adequate for the Z mass peak calibration is likely to be the good choice for the precision measurement of the W boson mass. Since this material description is obtained with electrons in the same energy range as the electrons for the W boson mass measurement, a partial compensation for material effects by scale factors would only have a minor impact. For the search for a heavy Z' boson with a mass larger than $1\,\mathrm{TeV/c^2}$ the energy scale at a few hundred GeV is essential. Therefore a partial compensation for material effects by scale factors would have to be extrapolated to these energies and the impact would be much larger for the Z' boson search.

Conclusions

During the combined test beam in summer 2004 a slice of the ATLAS barrel detector - including all detector sub systems from the inner tracker, the calorimetry to the muon system - was exposed to particle beams (electrons, pions, photons, muons) with different momenta (1 GeV/c to 350 GeV/c). The aim was to study the combined performance of the different detector subsystems in ATLAS-like conditions. The first part of the thesis covered the analysis of data taken at the combined test beam 2004 with the ATLAS LAr calorimeter with particles traversing a magnetic field prior to their measurement similar to ATLAS data taking. The calibration of the energy measurement for electrons with the presence of a magnetic field has been investigated and the differences with respect to the calibration without magnetic field have been analyzed. The linearity obtained is 0.28% for the energy range of 20 to 100 GeV which is within the estimated systematic uncertainties. The stochastic term of the energy resolution is $(10.1 \pm 0.1)\%$ GeV$^{1/2}$ after noise subtraction. This is compatible with previous test beam results without magnetic field and fulfills the physics requirements for the ATLAS LAr calorimeter.

I developed a method to intercalibrate the energy scale of the electromagnetic calorimeter and the momentum scale of the Inner Detector by investigating the E/p distribution for electrons. This method has been evaluated with data from the combined test beam 2004. It has been demonstrated that the correlation between E and p has to be taken into account in order to intercalibrate the two scales with a precision better than a 1%. The precision obtained for the relative scale is better than 5‰ when the correlation computed with Monte Carlo is applied to the data and is limited by the available statistics.

The intercalibration method using the E/p distribution developed for the combined test beam 2004 has been adapted for the ATLAS detector using electrons from W boson decays and studied with Monte Carlo simulations. It has be demonstrated that the intercalibration method will allow the calibration of the scale of the electromagnetic calorimeter with an integrated luminosity of 20 pb^{-1}, i.e. approximately 235.000 events, at the level of a few ‰ including the systematic uncertainties arising from the description of the material upstream of the electromagnetic calorimeter and the parameter extraction procedure.

The intercalibration method which I have developed in this thesis will be used for the calibration of the energy scale of the electromagnetic calorimeter with the first LHC collisions data. It is one of the main ingredients to obtain a calibrated ATLAS detector with an integrated luminosity of $100\,\mathrm{pb}^{-1}$. Using this calibration ATLAS will be ready for discoveries beyond the present frontiers of experimental high energy physics.

Appendix A

For the Monte Carlo simulation of the ATLAS detector a dedicated geometry has been implemented to assess the impact of the material distribution in the detector on various measurement variables. The ATLAS geometry tag for this geometry with additional material is ATLAS-CSC-02-02-00.

The geometrical acceptance of the detector was divided in 8 regions (4 quadrants in φ and η positive/negative) and a different material configuration was implemented by adding additional material to the Inner Detector or the Liquid Argon electromagnetic calorimeter for each region.

Inner Detector

For the Inner Detector, material was only added in the upper half of the detector ($0 < \varphi < \pi$). The additional material was implemented as additional thin layers of material. Carbon has been used when enough free space was available, otherwise aluminium or copper has been used.

The depths of the material contributions are quoted in radiation lengths X_0. They are listed below for particles impinging normal to the surface.

- Sensitive layers (These additions are all much larger than the uncertainty but smaller increments would not be visible.)

  1. Barrel Pixel detector: Just after B-layer: +1% X_0 (Aluminium)
  2. Barrel SCT layer 2: increasing from +1% X_0 at $z = 0$ to +3% X_0 at $z = z_{max}$ (Carbon)
  3. End-cap SCT disks 1 and 6 at side $z < 0$: +2% X_0 (Copper)
  4. End-cap SCT disks 3 and 5 at side $z > 0$: +3% X_0 (Copper)
  5. End-cap pixel disks: +1% X_0 for disk 2 at side $z < 0$ and for disk 3 at side $z > 0$ (Carbon)

- Barrel services

  1. Pixel barrel services in front of the pixel disks: +1% X_0 (Carbon)
  2. Pixel-SCT boundary: increasing from +0.6% X_0 at $z = z_{min}$ to +1.2% X_0 at $z = z_{max}$ (Carbon)
  3. TRT barrel at $z = z_{max}$: +3% X_0 (Carbon)

- End-cap services

  1. SCT end-cap services at $R = 55$ cm at side $z < 0$: +5% X_0 (Copper)
  2. SCT end-cap services at $R = 55$ cm at side $z > 0$: +5% X_0 (Copper)

- Services along cryostat

  1. PPB1 and PPF1 at side $z < 0$: +7.5% X_0 (Copper)
  2. PPB1 and PPF1 at side $z > 0$: +15% X_0 (Copper)
  3. Inner Detector end-plate and pixel services at side $z < 0$: +5.4% X_0 (Aluminium + Copper)
  4. Inner Detector end-plate and pixel services at side $z > 0$: +13.5% X_0 (Aluminium + Copper)
  5. All services along cryostat bore at side $z < 0$: +7.5% X_0 (Copper)
  6. All services along cryostat bore at side $z > 0$: +4.5% X_0 (Copper)

Liquid Argon Electromagnetic Calorimeter

- Barrel cryostat upstream of the calorimeter: +8-11% X_0 (radial, i.e to be multiplied by $\cosh(\eta)$ to get the amount seen by particles at η) for $\eta > 0$
- Between barrel presampler and strips: +5% X_0 (radial) for $\pi/2 < \varphi < -\pi/2$ and $\eta > 0$
- Between barrel presampler and strips: +5% X_0 (radial) for $-\pi/2 < \varphi < \pi/2$ and $\eta < 0$
- Barrel cryostat downstream of the calorimeter: +7-11% X_0 (radial) for $\eta > 0$
- Gap barrel-endcap cryostats: Density of material increased by a factor of 1.7 (much more than the expected uncertainty)

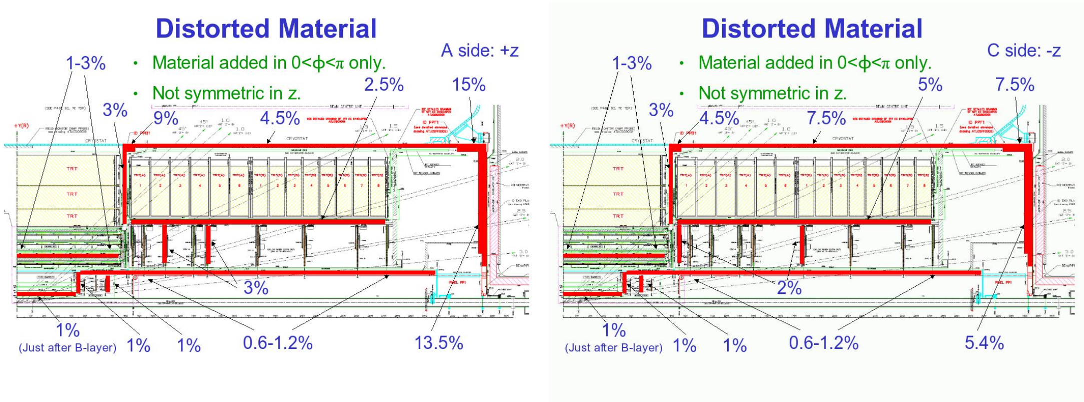

Description of the material added to the Inner Detector in the Monte Carlo simulation for the geometry ATLAS-CSC-02-02-00 for $0 < \varphi < \pi$ for side A (left), i.e. $\eta > 0$, and for side C (right), i.e. $\eta < 0$.

List of Acronyms

ALICE A Large Ion Collider Experiment. Heavy ion experiment at the LHC.

ATHENA ATLAS offline software framework.

ATLAS A Toroidal LHC ApparatuS. General purpose experiment at the LHC.

CERN European Center of Particle Physics located in Geneva, Switzerland.

CMS Compact Muon Solenoid. General purpose experiment at the LHC.

CSC Cathode Strip Chambers. Part of the ATLAS Muon Spectrometer.

CTB Combined Test Beam

FCal Forward Calorimeter. Part of the calorimeter system of ATLAS.

FEB Front End Board

LAr Liquid Argon

LAr EMB Liquid Argon Electromagnetic Barrel calorimeter. Part of the calorimeter system of ATLAS.

LEP Large Electron–Positron collider previously located at CERN.

LHC Large Hadron Collider located at CERN.

LHCb Heavy flavour physics experiment at the LHC.

MC Monte Carlo (simulation)

MDT Monitored Drift Tubes. Part of the ATLAS Muon Spectrometer.

OFC Optimal Filter Coefficients. Computed with the Optimal Filtering Method.

QCD Quantumchromodynamics

RPC Resistive Plate Chambers. Part of the ATLAS Muon Spectrometer.

SCT SemiConductor Tracker. Part of the ATLAS Inner Detector.

SPS CERN Super Proton Synchrotron

TGC Thin Gap Chambers. Part of the ATLAS Muon Spectrometer.

TRT Transition Radiation Tracker. Part of the ATLAS Inner Detector.

Bibliography

[1] Lyndon Evans and Philip Bryant (editors). LHC Machine. *Journal of Instrumentation*, 3(08):S08001, 2008.

[2] The ALICE Collaboration and K Aamodt et al. The ALICE experiment at the CERN LHC. *Journal of Instrumentation*, 3(08):S08002, 2008.

[3] The CMS Collaboration and S Chatrchyan et al. The CMS experiment at the CERN LHC. *Journal of Instrumentation*, 3(08):S08004, 2008.

[4] The LHCb Collaboration and A Augusto Alves Jr et al. The LHCb Detector at the LHC. *Journal of Instrumentation*, 3(08):S08005, 2008.

[5] The ATLAS Collaboration and G Aad et al. The ATLAS Experiment at the CERN Large Hadron Collider. *Journal of Instrumentation*, 3(08):S08003, 2008.

[6] C. Amsler et al. (Particle Data Group). Review of Particle Physics. *Physics Letters*, B667, 1, (2008) and 2009 partial update for the 2010 edition.

[7] Christian W. Fabjan and Fabiola Gianotti. Calorimetry for particle physics. *Rev. Mod. Phys.*, 75(4):1243–1286, Oct 2003.

[8] R. Wigmans. *Calorimetry*. Oxford University Press, 2000.

[9] Egidio Longo and Ignazio Sestili. Monte carlo calculation of photon-initiated electromagnetic showers in lead glass. *Nucl. Instrum. Methods Phys. Res., Sect. A*, 128(2):283–307, October 1975.

[10] The ATLAS Collaboration. *Expected Performance of the ATLAS Experiment: Detector, Trigger and Physics*. CERN, Geneva, 2008.

[11] The ATLAS collaboration. Detector and Physics Performance Technical Design Report. Technical Report CERN/LHCC/99-14/15, CERN, 1999.

[12] B. Aubert et al. Construction, assembly and tests of the ATLAS electromagnetic barrel calorimeter. *Nucl. Instrum. Methods Phys. Res., A*, A 558 (2006) 388-418, 2006.

[13] N.J. Buchanan et al. Design and implementation of the Front End Board for the readout of the ATLAS liquid argon calorimeters. *J.Instrum.*, 3 P09003, 2008.

[14] M. Aharrouche et al.(ATLAS Liquid Argon Group). Measurement of the Response of the ATLAS Liquid Argon Barrel Calorimeter to Electrons in the Energy Range from 1 to 250 GeV at the 2004 Combined Test-Beam. *submitted to Nucl. Instrum. Meth.*, NIMA-D-09-00590, 2009.

[15] B. Di Girolamo et al. ATLAS Barrel Combined Run in 2004 Test Beam Set-up and its Evolutions. *ATLAS EDMS Note*, ATC-TT-ID-0001, EDMS Id: 406980, 2005.

[16] M. Gilchriese (editor). Construction and Performance of the ATLAS Pixel Detector. *J.Instrum., [NOT YET PUBLISHED].*

[17] A. Abdesselam et al. The Barrel Modules of the ATLAS SemiConductor Tracker. *Nucl. Instrum. Methods Phys. Res., A*, A568 (2006) 642671, 2006.

[18] E. Abat et al. The ATLAS TRT Barrel Detector. *J.Instrum.*, 3 P02014, 2008.

[19] The ATLAS collaboration. Liquid Argon Calorimeter Technical Design Report. Technical Report CERN/LHCC/96-041, CERN, 1996.

[20] J. Abdallah et al. Design, Construction and Installation of the ATLAS Hadronic Barrel Scintillator-Tile Calorimeter. *J.Instrum., [NOT YET PUBLISHED]*, ATL-TILECAL-PUB-2008-001, 2008.

[21] B. Di Girolamo et al. Beamline instrumentation in the 2004 combined ATLAS testbeam. *ATLAS Internal Note*, ATLAS-TECH-PUB-2005-001, 2005.

[22] M. Boonekamp. Private communication.

[23] M. Aleksa, M. Delmastro, M. Fanti, R. Lafaye, W. Lampl, S. Laplace, D. Prieur, F. Tarrade, I. Wingerter-Seez. ATLAS Combined Testbeam: computation and validation of the electronic calibration constants for the electromagnetic calorimeter. *ATLAS Internal Note*, (ATL-LARG-PUB-2006-003), 2006.

[24] W.E. Cleland and E.G. Stern. Signal processing considerations for liquid ionization calorimeter in a high rate environment. *Nucl. Instrum. Methods Phys. Res., A*, 338, 1984.

[25] D. Banfi, M. Delmastro and M. Fanti. Cell response equalization of the ATLAS electromagnetic calorimeter without the direct knowledge of the ionization signals. *J.Instrum.*, 1:P08001, 2006. DOI: 10.1088/1748-0221/1/08/P08001.

[26] L. Neukermans, P.Perrodo and R. Zitoun. Understanding the electromagnetic barrel pulse shapes and the absolute electronic calibration. *ATLAS Internal Note*, ATL-LARG-2001-008, 2001.

[27] M. Citterio, M. Delmastro and M. Fanti. *A study of the electrical properties and of the signal shapes in the ATLAS Liquid ARgon Accordion Calorimeter using a hardware model*. *ATLAS Internal Note*, ATL-LARG-2001-018, 2001.

[28] D. Prieur. Using Time Convolution Method to compute Optimal Filtering Coefficients for LARG electromagnetic calorimeter. *ATLAS Internal Note*, ATL-LARG-2005-001, 2005.

[29] M. Aharrouche et al.(ATLAS Liquid Argon Group). Energy Linearity and Resolution of the ATLAS Electromagnetic Barrel Calorimeter in an Electron Test-Beam. *Nucl. Instrum. Meth.*, A568:601–623, 2006.

[30] W Lampl, S Laplace, D Lelas, P Loch, H Ma, S Menke, S Rajagopalan, D Rousseau, S Snyder, and G Unal. Calorimeter clustering algorithms: Description and performance. Technical Report ATL-LARG-PUB-2008-002. ATL-COM-LARG-2008-003, CERN, Geneva, Apr 2008.

[31] S. Agostinelli et al. (GEANT4 Collaboration). Geant4: A simulation toolkit. *Nucl. Instrum. Meth.*, A506:250, 2003.

[32] B. Di Girolamo, M. Gallas and T. Koffas. 2004 ATLAS Barrel Combined Test Beam Layout. *ATLAS EDMS Note*, ATC-TT-IN-0001, 2005.

[33] F. Hubaut, B. Laforge, D. Lacour, F. Orsini. Test beam Measurement of the Crosstalk in the EM Barrel Module 0. *ATLAS Internal Note*, ATL-LARG-2000-007, 2000.

[34] F. Hubaut. Crosstalk Measurements in the EM Barrel Module 0 from 99', May 00' and July 00' Beam Tests. *ATLAS Internal Note*, ATL-LARG-2000-009, 2000.

[35] M. Delmastro, M. Aleksa, T. Carli, R. Froeschl, I. Wingerter-Seez. Response of the ATLAS Liquid Argon Electromagnetic Barrel Calorimeter to Very Low Energy Electrons at the 2004 ATLAS Combined Test-Beam. *ATLAS Internal Note*, (ATL-COM-LARG-2009-014), 2009.

[36] T. Koffas, T. Vu Anh. Private communication.

[37] D. Banfi, L. Carminati and L. Mandelli. Calibration of the ATLAS electromagnetic calorimeter using calibration hits. *ATLAS Note*, (ATL-LARG-PUB-2007-012), 2007.

[38] M Aleksa, F Bergsma, P-A Giudici, A Kehrli, M Losasso, X Pons, H Sandaker, P S Miyagawa, S W Snow, J C Hart, and L Chevalier. Measurement of the atlas solenoid magnetic field. *J. Instrum.*, 3(SN-ATLAS-2008-068):P04003. 20 p, Dec 2007. Accepted as Scientific Note SN-ATLAS-2008-068.

[39] J. E. Gaiser. *Charmonium Spectroscopy from Radiative Decays of the J/ψ and ψ'*. PhD thesis, SLAC-R-255, 1982. The Crystal Ball function is defined in Appendix F, p.178.

[40] V. M. Abazov et al. (D0 Collaboration). Simultaneous measurement of the ratio R = B(t $\rightarrow$ Wb)/B(t $\rightarrow$ Wq) and the top-quark pair production cross section with the d0 detector at sqrt(s) = 1.96 tev. *Physical Review Letters*, 100(19):192003, 2008.

[41] V. Gallo, S. Haug. Private communication.

[42] M Aleksa, F Bergsma, L Chevalier, P A Giudici, J C Hart, A Kehrli, M Losasso, P S Miyagawa, X Pons, H Sandaker, and S W Snow. Results of the ATLAS solenoid magnetic field map. *J. Phys.: Conf. Ser.*, 110:092018, 2008.

[43] M Aleksa, F Bergsma, P-A Giudici, A Kehrli, M Losasso, X Pons, H Sandaker, PS Miyagawa, SW Snow, JC Hart, and L Chevalier. Measurement of the solenoid magnetic field. Technical Report ATL-MAGNET-PUB-2007-001. ATL-COM-MAGNET-2007-002, CERN, Geneva, Sep 2007.

[44] M. Aharrouche et al. Response uniformity of the ATLAS liquid argon electromagnetic calorimeter. *Nucl. Instrum. Methods Phys. Res., A*, 582:429–455, Sep 2007.

[45] N Makovec. In-situ calibration of the electromagnetic calorimeter using Z $\rightarrow$ ee events (Monte-Carlo studies). Technical Report ATL-COM-LARG-2008-008, CERN, Geneva, Nov 2008.

[46] Reconstruction of photon conversions. Technical Report ATL-PHYS-PUB-2009-006. ATL-COM-PHYS-2009-172, CERN, Geneva, Apr 2009. CSC PUB Note.

[47] M Kuna, C Gabaldon Ruiz, F Hubaut, and P Pralavorio. Study of material in front of the EM calorimeter with high pt electron shower shapes and tracks. Technical Report ATL-PHYS-INT-2008-026. ATL-COM-PHYS-2008-081, CERN, Geneva, Jun 2008.

[48] M. Vincter. Private communication.

[49] S. Rossegger, R. Froeschl, M. Aleksa. Private communication.

Curriculum vitae

Robert Fröschl
geboren am 1. August 1976 in Wien
verheiratet, eine Tochter

6/94	Matura mit Auszeichnung
ab 10/94	Technische Universität Wien, Studium der Technischen Mathematik
03/97-06/97	Tutor am Institut für numerische und angewandte Mathematik, Technische Universität Wien
ab 10/97	Universität Wien, Studium der Physik
12/97-08/98	Siemens Austria Space Business Unit
ab 10/98	Universität Wien, Studium der Astronomie
03/99	Sponsion zum Diplom-Ingenieur (Technische Mathematik) mit Auszeichnung
12/99	Würdigungspreis des Bundesministers für hervorragende Studienleistungen (unter den besten 58 von ca. 15000 Absolventen in ganz Österreich im Jahr 1999)
09/99-04/00	Präsenzdienst an der Landesverteidigungsakademie in Wien, Abteilung für internationale Kontakte
07/00	ESA Summer School Alpbach "Extragalactic Astronomy & Cosmology from Space"
06/02	Summer School "Post-Accident Radiation Monitoring Techniques", Kyiv, Ukraine
04/03	Sponsion zum Magister der Naturwissenschaften (Physik) mit Auszeichnung
07/04-02/07	Austrian Research Centers - Material Research
ab 03/07	Technische Universität Wien & CERN, Doktoratsstudium Physik